Generation and detection of optical vortex beam

Mardan Dezfouli, Ali

University of Zagreb

Faculty of Science

Ali Mardan Dezfouli

GENERATION AND DETECTION OF OPTICAL VORTEX BEAM

DOCTORAL THESIS

Supervisor:
Dr.sc. Hrvoje Skenderović

Zagreb, 2024

Prirodoslovno-matematikčki fakultet

Ali Mardan Dezfouli

GENERIRANJE I DETEKCIJA OPTIČKIH VRTLOŽNIH SNOPOVA

DOKTORSKI RAD

Voditelj:
Dr.sc. Hrvoje Skenderović

Zagreb, 2024

Supervisor Biography

Hrvoje Skenderović received his PhD in 2000 working on the spectroscopy of electric discharges at the Institute of Physics, Zagreb. As a Humboldt postdoctoral fellow, he spent two years (2001 – 2003) at the Institute for Quantum Optics in Garching, Germany working on ultrafast dynamics of molecules. After returning to the Institute of Physics he continued to work in the field of femtosecond spectroscopy. He co-authored about 50 papers indexed in WoSCC base and participated at numerous international conferences. His longer stays abroad include TU Wien in 2010. and University of Heidelberg, 2011 – 2012. More recently, his work includes research in digital holography, laser machining and quantum light. He mentored three finished PhD thesis.

Acknowledgments

I am immensely grateful to Dr. Hrvoje Skenderović, my supervisor, for providing me with the opportunity to work within the Coherent Optics and Digital Holography Laboratory. His unwavering support, guidance, and encouragement have been invaluable throughout my entire journey during my PhD studies.

I'd like to extend my sincere gratitude to those individuals with whom I've had direct conversations, for their invaluable guidance and assistance: Prof. Hrvoje Buljan, Dr. Nazif Demoli, Dr. Nikša Krstulović, Dr. Silvije Vdović, Dr. Goran Zgrablić. Dr. Neven Šantić, Dr. Damir Dominko.

Furthermore, my thanks go to: Dr. Mario Rakić, Dr. Denis Abramović, Dr. Juraj Krsnik, and Vedran Brusar, at institute of physics for the collaboration and interesting talks which we had during my study.

I extend my sincere appreciation to Marko Hum and Marija Sobol for their invaluable assistance and professionalism in addressing administrative matters throughout this journey.

Finally, I extend my heartfelt gratitude to my family for their support and encouragement throughout this journey. Their encouragement has been an invaluable source of motivation for me.

Abstract

Light can have a special property called orbital angular momentum (OAM), which gives beams a twisted shape of the wavefront. Twisted beams carry a specific amount of angular momentum in the direction of propagation. This property opens possibilities for increasing amount of information we can send in both optical and quantum communication. It could also help us improve and expand the capabilities of some types of quantum technology. By changing a regular beam of light in a particular way, we can create beams with some unique features. In this work, emphasis is given on Laguerre-Gaussian (LG) modes, and their generation and detection. LG modes carry non-zero OAM and are characterized by two numbers: the radial mode index p and the azimuthal mode index l, known as topological charge (TC).

This thesis delves into exploring the use of spatial light modulators (SLM) for the modal detection of Laguerre-Gaussian (LG) beams. A critical challenge in utilizing LG beams is to accurately determine indices of the unknown LG beam, which constitutes the main topic of this thesis.

As a major contribution, a new type of diffraction grating was designed, which offers effective modal detection of LG beams. Our approach showcases a robust method capable of simultaneously determining both mode indices of an LG mode. Theoretical and experimental results show a clear correlation of the radial and azimuthal mode indices with the intensity distribution in the far-field diffraction pattern.

Key words

orbital angular momentum of light, spatial light modulator, diffraction

Sažetak

Svjetlost može biti nositelj i kutne količine gibanja (OAM), što se ispoljava u valnoj fronti uvrnutog oblika, odnosno svjetlosnom vrtlogu. Vrtložne zrake nose određenu kutnu količinu gibanja u smjeru širenja. Ovo svojstvo otvara mogućnosti za povećanje količine informacija koje možemo poslati u redovnoj i kvantnoj komunikaciji. Također bi nam moglo pomoći da poboljšamo i proširimo mogućnosti nekih vrsta kvantne tehnologije. Promjenom regularne zrake svjetlosti na određeni način, možemo stvoriti zrake s jedinstvenim značajkama. U ovoj studiji ćemo staviti naglasak na Laguerre-Gaussovi (LG) modove, njihovo generiranje i detekciju. LG modovi nose OAM različit od nule i karakteriziraju ih dva broja: indeks radijalnog moda p i indeks azimutalnog moda l, poznat kao topološki naboj (TC).

Ovaj se doktorski rad bavi istraživanjem upotrebe prostornih modulatora svjetla (SLM) za modalnu detekciju Laguerre-Gaussovih (LG) zraka. Kritični izazov u korištenju LG snopa je točno određivanje indeksa nepoznatog LG snopa, što je i glavna tema ove disertacije.

Kao originalni doprinos, u doktoratu je dizajnirana nova vrsta difrakcijske rešetke kojom se postiže učinkova detekcija moda LG zrake. Naš pristup predstavlja robusnu metodu koja može istovremeno odrediti oba indeksa LG zrake. Teorijski i eksperimentalni rezultati pokazuju jasnu korelaciju između indeksa radijalnog i azimutalnog moda i distribucije intenziteta u difrakcijskom uzorku dalekog polja.

Ključne Riječi

Kutna količina gibanja svjetlosti, prostorni modulator svjetlosti, difrakcija

Extended Abstract

The intrinsic property of light known as orbital angular momentum (OAM) manifests in optical vortex (OV) beams. These beams exhibit a spiral-shaped wavefront, carrying discrete units of quantized orbital angular momentum ($l\hbar$) per photon, where 'l' denotes an integer, referred to as topological charge (TC). This Hilbert space associated to OAM is theoretically infinite and holds promise for amplifying information capacities in both classical and quantum communication systems. Moreover, it offers potential for enhancing and broadening the capabilities of qubit and qudit-based quantum algorithms. Furthermore, leveraging OAM modes enables innovative imaging methodologies to directly observe and measure diverse topological attributes in objects spanning from semiconductors defects to the observation of astronomical objects. In optics, OAM of light already, utilized as optical tweezers to manipulate small objects. From the physical sciences point of view, our understanding of OAM in optical fields may provide insights into vortex behavior in other physical systems.

Optical vortices are created by optical diffractive elements, which can be produced via techniques like photolithography. Dynamic phase variations essential for this purpose are facilitated by devices such as electro-optical and acousto-optical modulators, along with liquid crystal spatial light modulators (LC-SLM). LC-SLM comprise, a microscopic array of individually controllable pixels, consisting of liquid crystal cells. Each pixel has the capability to introduce a specific phase shift to the incident light. LC-SLM offer distinct advantages including high resolution, small pixel size, and a high fill factor. They play a significant role in quickly and dynamically implementing digital holographic techniques within experimental setups.

This thesis covers two main topics: (1) generation of beam carrying an OAM and (2) detection of OAM state of light using diffractive method, with both parts relying significantly on the utilization of SLMs.

The chapters in this thesis are organized as follows. In Chapter 1, a historical exploration traces the evolution of understanding angular momentum within the realm of light. This chapter not only delves into the history related to the angular momentum of light but also introduces the Laguerre-Gaussian (LG) mode, as solution to the paraxial wave equation. Furthermore, Chapter 1 extensively surveys the literature, elucidating the diverse and extensive applications harnessing the unique properties of OAM. It illuminates how these applications span various fields, including optical communications, tweezers, microscopy, and quantum information processing, showing the widespread relevance and potential impact of OAM in modern science and technology.

Chapter 2 provides a survey of the literature focusing on two main aspects: the generation of optical vortex beams and the techniques used for their detection. Different methods utilized in creating and detecting optical vortex beams are described in the chapter. This thorough exploration covers a wide array of techniques, shedding light on the challenges, and potential applications associated with detecting OAM.

Within Chapter 3, we investigate the experimental generation of optical vortices using, SLM. This investigation involves employing various phase modulation techniques enabled by SLMs to generate and control vortex beams. Furthermore, this chapter gives a short discussion about technical challenges inherently linked to the application and implementation of SLMs. The discussion involves an exploration of these potential challenges, seeking to provide insights and possible solutions for proficiently utilizing SLMs in the generation and manipulation of shaped light.

In Chapter 4, the foundation is set by introducing the theory that focuses on detecting the LG mode based on its azimuthal index, keeping the radial index at zero. This theoretical framework paves the way for subsequent practical demonstrations and experimental pursuits aimed at detecting the OAM state of light. These experiments are specifically designed to employ our original sinusoidally-shaped phase gratings (SSPG) designed as a computer generated hologram (CGH) loaded on SLM for detection of TC. Furthermore, this chapter delves into an exploration of the adaptive nature intrinsic in SSPGs, shedding light on their dynamic capacity and their role in enhancing detection efficiency.

Chapter 5 redirects its focus toward assessing the efficiency of detection within the framework of laser beam misalignment tolerances. This chapter is dedicated to understanding how the detection mechanisms perform when subjected to variations or misalignments in laser beam positioning. It aims to explore the impact of these misalignments on the accuracy and reliability of detection methods, providing crucial insights into the robustness and adaptability of detection systems in scenarios where misalignments are prevalent.

Chapter 6 thoroughly examines the detection techniques used for measuring both LG radial and azimuthal modal indices. This exploration aims to generate and detect LG mode, for different radial and azimuthal mode indices. This analysis provides a clearer insight into the intricate properties and behaviors exhibited by LG beams across their diverse modal indices.

Chapter 7 encapsulates the conclusions drawn from the conducted research and outlines potential pathways for furthering this study. It offers a summary of the research findings and paves the way for future directions and ongoing exploration in this field.

Prošireni Sažetak

Intrinzično svojstvo svjetlosti poznato kao kutna količina gibanja (OAM) očituje se u optičkim vrtložnim (OV) zrakama. Ove zrake pokazuju valnu frontu spiralnog oblika, noseći diskretne jedinice kvantizirane kutne količine gibanja ($l\hbar$) po fotonu, gdje 'l' označava cijeli broj, koji se naziva topološki naboj (TC). Ovaj Hilbertov prostor povezan s OAM-om teoretski je beskonačan i veoma perspektivan za povećanje informacijskih kapaciteta u klasičnim i kvantnim komunikacijskim sustavima. Štoviše, nudi potencijal za poboljšanje i proširenje kvantnih algoritama temeljenih na qubitima ili quditima. Nadalje, korištenje OAM načina rada omogućuje inovativnim slikovnim metodologijama izravno promatranje i mjerenje različitih topoloških atributa u objektima, od defekata poluvodiča do promatranja astronomskih objekata. U optici, OAM svjetlosti već se koristi kao optička pinceta za manipuliranje malim objektima. Sa stajališta fizičkih znanosti, naše razumijevanje OAM-a u optičkim poljima može pružiti uvid u ponašanje vrtloga u drugim fizičkim sustavima.

Optički vrtlozi nastaju upotrebom optičkih difrakcijskih elemenata, koji se mogu proizvesti tehnikama poput fotolitografije. Dinamičke varijacije faza bitne za ovu svrhu omogućavaju uređaji kao što su elektro-optički i akusto-optički modulatori, kao i prostorni svjetlosni modulatori s tekućim kristalima (LC-SLM). LC-SLM sastoje se od mikroskopskog niza piksela kojima se može pojedinačno upravljati, a koji se sastoje od ćelija tekućeg kristala. Svaki piksel ima sposobnost unijeti određeni fazni pomak upadnog svjetla. LC-SLM nude različite prednosti uključujući visoku rezoluciju, malu veličinu piksela i visok faktor popunjavanja. Oni igraju značajnu ulogu u brzoj i dinamičnoj implementaciji digitalnih holografskih tehnika unutar eksperimentalnih postava.

Ovaj doktorski rad pokriva dvije glavne teme: (1) generiranje OAM-a koji nosi zraku i (2) Detekcija OAM stanja svjetlosti pomoću difrakcijske metode, pri čemu se oba dijela značajno oslanjaju na korištenje SLM-ova.

Poglavlja u ovoj tezi organizirana su na sljedeći način. U 1. poglavlju, dan je povijesni pregled evoluciju razumijevanja svjetlosti koja posjeduje kutnu količinu gibanja. Ovo poglavlje također predstavlja Laguerre-Gaussovu (LG) funkciju, kao jedno od rješenja paraaksijalne valne jednadžbe. Nadalje, Poglavlje 1 opsežno daje pregled literature, i opis raznolike i opsežne primjene jedinstvenih svojstava OAM-a. Osvjetljavaju se i aplikacije vezane uz optičke komunikacije, optičku pincetu, mikroskopiju i kvantnu obradu informacija. Pokazuje se široka važnost i potencijalni utjecaj OAM-a u modernoj znanosti i tehnologiji.

Poglavlje 2 daje pregled literature usredotočujući se na dva glavna aspekta: stvaranje optičkih vrtložnih zraka i tehnike korištene za njihovu detekciju. Pokazuju se različite metode korištene u stvaranju i detekciji optičkih vrtložnih zraka. Prikazane je široka lepeza tehnika, s osvrtom na izazove i potencijalne primjene povezane s otkrivanjem OAM-a.

Unutar poglavlja 3 istražujemo eksperimentalno generiranje optičkih vrtloga pomoću SLM-a. Ovo istraživanje uključuje korištenje različitih tehnika fazne modulacije koje omogućuju SLM za generiranje i upravljanje vrtložnim zrakama. Nadalje, ovo poglavlje donosi kratku raspravu o tehničkim izazovima koji su inherentno povezani s primjenom i implementacijom SLM-a. Rasprava uključuje istraživanje potencijalnih izazova i rješenja za efikasnu upotrebu SLM-a u stvaranju i manipuliranju strukturiranog svjetla.

U 4. poglavlju temelj je postavljen uvođenjem teorije koja se usredotočuje na otkrivanje LG moda na temelju njegovog azimutalnog indeksa, zadržavajući radijalni indeks na nuli. Ovaj teorijski okvir utire put kasnijim praktičnim demonstracijama i eksperimentalnim potragama s ciljem otkrivanja OAM stanja svjetlosti. Ovi eksperimenti se odvijaju pomoću originalno dizajnirane fazne rešetke sinusoidnog oblika (SSPG), realizirane kao računalno generirani hologram (CGH) učitan na SLM.. Nadalje, u ovome se poglavlju demonstrira adaptivna priroda SSPG-a, dinamički kapacitet i poboljšanje učinkovitosti detekcije.

Poglavlje 5 prikazuje istraživanja učinkovitosti detekcije unutar okvira tolerancija neusklađenosti laserske zrake. Ovo je poglavlje posvećeno razumijevanju učinkovitosti detekcije kada i prisustvu varijacija ili neusklađenosti u pozicioniranju laserske zrake. Cilj je istražiti utjecaj tih neusklađenosti na točnost i pouzdanost metoda detekcije, pružajući ključne uvide u robusnost i prilagodljivost sustava detekcije.

Poglavlje 6 temeljito ispituje tehnike detekcije LG zrake koja posjeduje i radijalni i azimutalni modalni indeks različit od nule. Ovo istraživanje ima za cilj generirati i detektirati LG mod za različite radijalne i azimutalne indekse. Ova analiza pruža jasniji uvid u svojstva i ponašanja LG p i l modova

U 7. poglavlju sažimaju se zaključci izvedeni iz provedenog istraživanja i ocrtavaju potencijalni putovi za daljnji nastavak ove studije. Prikazan je sažetak istraživanja i putevi za buduće smjerove istraživanja i primjene u ovom području.

List of abbreviations

OAM orbital angular momentum of light

SLM spatial light modulator

LCD liquid crystal display

SPP spiral phase plate

SAM spin angular momentum of light

OV optical vortex

TC topological charge

CGH computer generated hologram

LG Laguerre-Gaussian mode

SSPG sinusoidally-shaped phase gratings

Table of Contents

1 The orbital angular momentum of light

1.1 The history of the momentum of light

From the mid-19th century onward, it has been established that light beams possess both energy and momentum, a foundational characteristic elucidated by Maxwell's equations [1]. This momentum gives rise to radiation pressure, symbolized as P, which is equivalent to I/c, where I signifies the irradiance of the incoming laser light.

Poynting, while examining Maxwell's equations, derived an expression for the angular momentum of light. His investigation centered on the rotation within the electromagnetic field present in circularly polarized light beams. Drawing an analogy between this rotation and the mechanical movement of a revolving shaft, he suggested that circularly polarized light also carries angular momentum. His findings indicated that the ratio of angular momentum to energy equates to 1/ω, where ω represents the light's angular frequency [2]. Recognizing the minute scale of this effect, Poynting himself considered it highly unlikely to observe it through a mechanical experiment.

The experimental demonstration of this angular momentum occurred in the 1930s through a study conducted by Beth in a laboratory setting. [3]. In Beth's experiment, circularly polarized light passed through a half-wave plate, leading to the plate's rotation. The key aspect of the experiment was suspending the waveplate using a quartz fiber to minimize frictional effects. The rotation occurred because the waveplate reversed the handedness of the circularly polarized light, consequently reversing its angular momentum. This change in momentum caused a torque on the waveplate, resulting in its rotation.

The initial investigations were grounded in a classical interpretation of light, not requiring the quantized electromagnetic field. However, in modern physics, the interaction between light and matter is often explained in photon terms rather than in the context of electromagnetic waves. The quantification of momentum within a light beam involves evaluating the momentum per photon, expressed as $\hbar k$ for linear momentum and $\hbar$ for angular momentum. These quantized expressions align with the classical interpretations known to Maxwell and Poynting when considering the earlier mentioned ratios of momentum and energy. In the context of a quantum interpretation of light beams, circular polarization

is understood as the result of individual photons spinning either in a left-handed or right-handed direction. This spinning motion is termed spin angular momentum., of value $\sigma\hbar$, where $\sigma = \pm 1$ depending on sense of circular polarization.

Yet, as early as the 1930s, there were hints suggesting that light could carry more intricate momentum states. When discussing photons, they are generated during atomic transitions, and in the case of dipole transitions, the alteration in angular momentum amounts to $\hbar$. Consequently, emitted circularly polarized light aligns with the principle of momentum conservation. In 1932, Darwin explored higher-order transitions, revealing momentum transfers surpassing the value of $\hbar$ [4]. He proposed that light emitted in proximity to an atom's center of mass would impart not only linear momentum to the emitted photon but also an extra torque on the center of mass. This supplementary angular momentum, now identified as orbital angular momentum, originated from these higher-order transitions.

1.2 Laguerre-Gaussian Modes: Characteristics and Applications

Fast forward to 1992 when Allen and his team, while conducting research in Leiden, explored the realm of orbital angular momentum present in Laguerre-Gaussian (LG) laser beams [5]. LG beams are distinguished by their helical phase fronts, which inherently encompass a phase singularity at their core. The term optical vortex (OV) refers to a zero-point within an optical field, signifying a location of zero intensity, where phase is undefined. Since the 1970s, there has been ongoing examination and scrutiny of these phase singularities with extensive research in the optical fields [6, 7] .

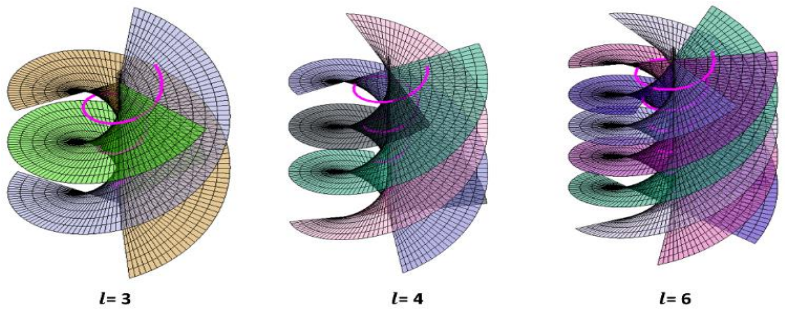

Figure 1-1: Numerically simulated the spiral phasefronts of vortex beam for different azimuthal value. Light can carry OAM if its phasefronts are twisted around the direction that the light is moving. The linear momentum of the light (perpendicular to the phasefronts; depicted by a pink-colored spiral line) has a small component around the propagation direction, resulting in the generation of orbital angular momentum aligned with the direction of the beam's propagation.

Yet, none of these preceding studies had pinpointed the angular momentum linked to helically phased beams. LG modes are solutions of the paraxial wave equation. These modes exhibit circular symmetry and can be expressed using Laguerre polynomials L_p^l, with 'p' denoting the radial index and 'l' representing the azimuthal index. Expressed in cylindrical coordinates, the complex amplitude of an LG beam is formulated as:

$$u_p^{\ell}(r,\varphi) = C_{\ell,p}\left(\frac{\sqrt{2}r}{w_0}\right)^{|\ell|} L_p^{|\ell|}\left(\frac{2r^2}{w_0^2}\right)\exp\left[\frac{-r^2}{w_0^2}\right]\exp\left(i\,\ell\varphi\right) \tag{1-1}$$

where w_0 is the beam waist size, $L_p^{|l|}$ representing the Laguerre polynomial of the variables l and p, and C_{lp} is the term for amplitude normalization [8]. The variables possess broad ranges: 'l' extends across unbounded values, and 'p' can either be zero or assume any positive integer. The crucial term in this complex amplitude is $\exp(il\varphi)$, which governs the azimuthal phase profile of these beams. Figure 1-2 showcases the numerically simulated transverse intensity profiles of various LG beam.

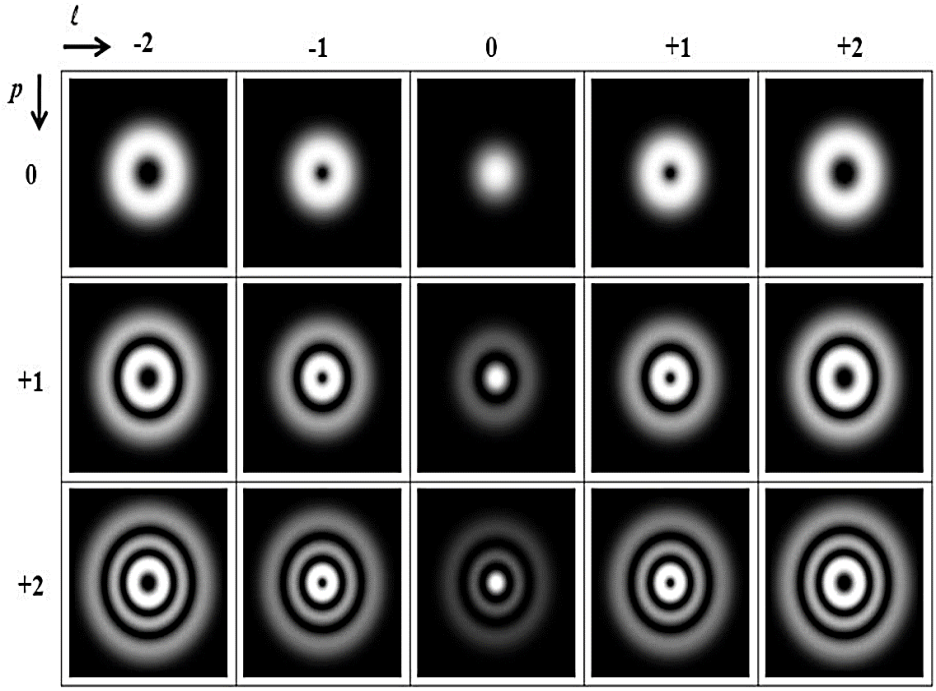

Figure 1-2: intensity profiles of numerically simulated LG beams with different combinations of radial and azimuthal mode indices. The rows and columns in the figure correspond to the azimuthal and radial mode indices, respectively.

Utilizing Equation (1-1), It is possible to derive expressions that describe the energy and momentum contained within such a beam. They are characterized by the spatially dependent form of the Poynting vector, as illustrated in Figure 1-1. Within a ray optics framework, the Poynting vector dictates the direction of a local ray originating from a particular position on the wavefront [9]. Helically phased beams cause a deviation in these local rays, and each ray carries a linear momentum. When averaged across the entire beam, this linear momentum generates an azimuthal component contributing to the beam's momentum, ultimately resulting in angular momentum aligned with the direction of propagation.

Looking at the helical phase front at a fixed distance from the beam's center, it resembles a slope with a constant incline in azimuthal coordinates. At a specific distance from the center, this slope covers a length of $2\pi r$ with the height of $l\lambda$ where λ is the wavelength of the light, therefore, the angle of skewness for the local rays is:

$$\gamma = \frac{\ell\lambda}{2\pi r} = \frac{\ell}{kr} \tag{1-2}$$

Given the wavenumber k related to the beam, upon analyzing the linear momentum 'P' carried by a singular skewed local ray interacting with a surface at an angle γ, we can determine the resulting orbital angular momentum carried by the beam:

$$|L| = |r \times P| = |r \times \hbar k \, sin\gamma| = l\hbar \tag{1-3}$$

Allen and colleagues hypothesized that these beams possess a ratio of OAM to energy expressed as l/w, resulting an OAM of $l\hbar$ per photon.

In contrast to the spin angular momentum (SAM) with solely two orthogonal states (binary state) with values $\sigma = \pm 1$, The states associated with the OAM are boundless described by l. Every integer value of l stands as orthogonal to all others. Nevertheless, this advantage introduces a formidable challenge in the measurement techniques. Embracing N modes means delving into an N-dimensional state space. To overcome the complex task of detecting OAM, we must achieve flawless detection of all of N potential OAM states. This achievement is the key to unlocking the solution to the challenge of OAM detection.

Allen et al. suggested an experiment similar to Beth's approach for measuring spin angular momentum (SAM). They used two cylindrical lenses to flip the phase profile's direction, changing the beam's orbital

angular momentum. This shift in momentum was expected to cause a rotational motion in the lenses, as shown in Figure 1-3.

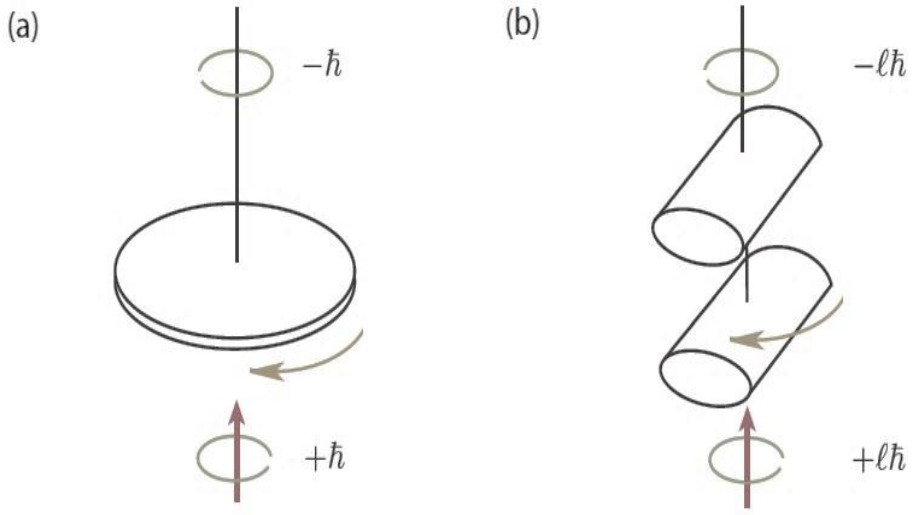

Figure 1-3: (a) Demonstrates the rotational torque exerted on a $\pi/2$ waveplate as circularly polarized light passes through, altering the polarization state from left-handed to right-handed. (b) Illustrates suspended cylindrical lenses undergoing rotation when a helical beam traverses the lenses, converting the OAM value from $l\hbar$ to $-l\hbar$. (Schematic reproduced from Reference [5]).

Showing this effect in larger objects has been tricky. The torque from orbital angular momentum isn't strong enough to rotate big things, but in the tiny world, it's a different story. After Allen et al.'s initial work, He looked into passing orbital angular momentum to tiny absorbing particles held in optical tweezers. (Figure 1-4) [10].

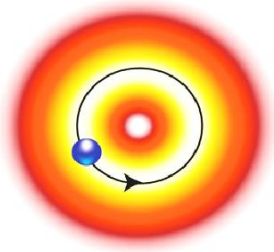

Figure 1-4: A micro-particle is trapped by a helically-phased beam. The partially absorbing nature of this microparticle leads to the absorption of OAM, consequently generating torque.

Optical tweezers capture particles by harnessing the intensity gradient within focused light beams. This force attracts dielectric particles toward the center of the high field strength area, enabling the

manipulation and confinement of micro-scale particles. When employing a helically phased beam to trap particles, aligning the beam's waist size with that of the particle positions the center of attraction at the phase singularity within the beam's center. Initial investigations exploring torque exerted by OAM-carrying beams utilized black micron-sized CuO particles. These particles demonstrated rotation when trapped using a plane-polarized LG beam. Subsequent studies combined the torque generated by OAM with that arising from the spin angular momentum of circularly polarized light. By altering the relative orientation of these two components, the particle's rotation could be accelerated, decelerated, or even halted [11, 12]. Besides the evident mechanical applications of OAM-carrying beams, a pivotal study focused on the conservation of OAM during second harmonic generation (SHG). In SHG, a nonlinear crystal effectively merges photons of a specific energy to generate a new photon with twice that energy. Observations revealed that OAM remains preserved, with the second harmonic output possessing double the OAM of the input light [13]. Second-order processes like SHG are reversible. In the reverse process, known as parametric down-conversion, the energy of a single pump photon splits into two new photons. In 2001, Mair et al. investigated the conservation of OAM during down-conversion, commonly utilized for entangled photon preparation [14]. Their work demonstrated that a down-converted photon could possess various l values. When the OAM of this photon combined with its entangled partner, it highlighted OAM conservation (Figure 1-5). These findings hinted at quantum entanglement, enabling exploration of this entanglement within higher-dimensional Hilbert spaces.

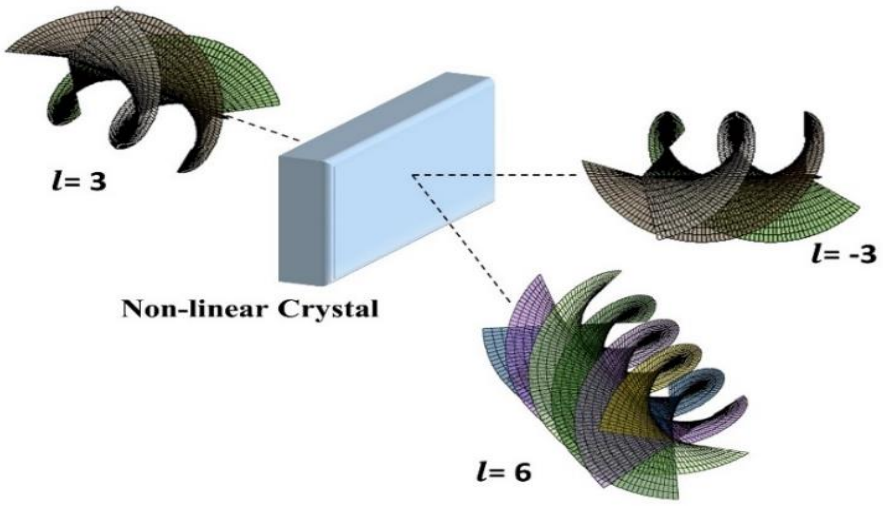

Figure 1-5: When a photon with a certain OAM passes through a nonlinear crystal, it splits into two photons, each having half the energy of the original. Their combined OAM equals the OAM of the input photon, and they can take various values. Here, we show the case of l = 6 and l = -3.

Any fully polarized state can be expressed as a combination of two perpendicular circular polarization states. Visualizing these combinations is often achieved through a Poincaré sphere, where the poles signify left and right circularly polarized light. Linear polarization, an equal amalgamation of left and right states, occupies the equatorial region of the Poincaré sphere. The orientation of linear polarization depends on the relative phase between these superimposed components. Similarly, an analogous sphere can be devised for LG modes, representing a subset of the unbounded LG state-space with two states. In this representation, the north and south poles correspond to different 'l' values, delineating the two-state subset [15]. An equal superposition of 'l' values creates petal-shaped laser modes. Changing the relative phase of these modes causes the mode to rotate. This comparison between spin angular momentum and OAM extends various quantum mechanics tests, originally focused on polarization, to subsets of the OAM state-spaces.

The discrete and limitless potential of OAM, where 'l' can theoretically assume any integer value, has sparked significant interest among researchers. This optical property has become a focal point for those striving to enhance data transmission across optical communications networks [16]. The current focus in OAM applications revolves around free-space links, where several developed schemes are attracting considerable interest [16-18], Wang et al. recently introduced a scheme that incorporates OAM multiplexing alongside other conventional multiplexing methods, resulting in data rates reaching 2.56 Tbit/s for their link [19]. Researchers are exploring OAM not solely as a means to augment communication link bandwidth but also as a pathway to bolster their security. The expanded alphabet offered by OAM holds promise in enhancing the security of cryptographic keys transmitted through a quantum key distribution (QKD) system [20]. In the realm of quantum information processing [21], OAM holds substantial promise for pioneering advancements in both quantum computing and communication. OAM-based communication systems, with their potential to revolutionize secure data transmission, hold the key to enhancing data capacity and network efficiency significantly [22]. Furthermore, OAM contributes to the advancement of cutting-edge imaging techniques, ultimately leading to higher resolution and superior imaging performance [23]. Beyond this, the applications of OAM extend their influence to a myriad of fields, including trapping particles [24], astrophysical studies [25]. In particular, OAM is instrumental in the creation of chiral structures with exceptional and unique properties [26]. Additionally, OAM plays a vital role in fundamental research [27], offering invaluable insights into the core principles of physics and expanding our comprehension of the intricate world of twisted light.

A critical challenge in utilizing LG beams across diverse applications is achieving precise determination of the indices for an unknown LG beam.

In this thesis, I uncover my substantial contributions to the realm of optics, where my primary focus revolves around the intriguing domain of light beams carrying OAM. Across my research journey, I have consistently exhibited a dedication to comprehending the complexities inherent in dealing with OAM state. I have been devoted to devising innovative solutions aimed at overcoming challenges in detection of LG beams.

2 Generation and detection of orbital angular momentum of light

In this chapter, we'll explore methods for generating and detecting OAM of light. While various techniques exist for creating vortex beams, our focus lies on intriguing methods such as the spiral-phase-plate (SPP), q-plate and computer-generated holograms (CGH), and spatial light modulators (SLM). Given the thesis's core focus on SLM, we'll delve deeper into its ability to shape light. Additionally, we'll discuss diverse OAM detection techniques, such as torque measurement on microscopic particles, counting spiral interference fringes, and studying propagations through specific apertures, among others.

2.1 Spiral phase plate (SPP)

A spiral phase plate (SPP) serves as a transparent optical diffractive element, depicted in Figure 2-1, Its structure resembles that of a spiral steps [28]. As light passes through the SPP, changes in its thickness induce distinct alterations in the optical path of the outgoing beam. This variation introduces a spiral phase factor $\exp(il\theta)$, where l is the topological charge of the SPP and θ is the rotation azimuth. This leads to the formation of an optical vortex in the light field, causing a phase singularity to emerge at the center of the outgoing beam, featuring a spiral wavefront structure.

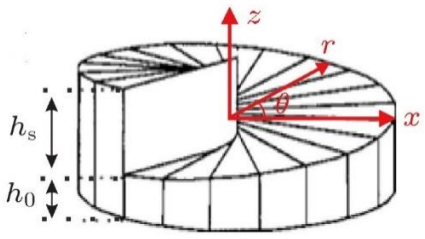

Figure 2-1: Ideal spiral phase plate.

The thickness 'h' correlates directly with the azimuth angle 'θ' and can be represented as follows:

$$h_{SPP} = h_0 + h_s \frac{\theta}{2\pi} \tag{2-1}$$

where h_0 represents the thickness of the phase-plate and h_s denotes the thickness of the step. Assuming minimal variation in the step height h of the SPP the light intensity of the outgoing beam becomes negligible. After the laser beam goes through the SPP, it mainly adjusts the phase of the outgoing beam. The resulting phase-delay expression after the beam passes through the SPP is:

$$\delta = \frac{2\pi}{\lambda}\left[\frac{(n-n_0)h_s\theta}{2\pi} + nh_0\right] \tag{2-2}$$

where λ is the wavelength of the incoming laser beam, and n and n_0 are the refractive index of material and refractive index of surrounding medium , respectively. The topological charge of SPP is expressed as $l = h_s(n-n_0)/\lambda$

The phase alteration, $\Delta\phi$, is contingent upon the rotation azimuth, θ. As θ increases from zero to 2π, the value of phase increments from 0 to $2\pi l$. In an ideal model, the SPP's thickness increases uniformly with the rotation azimuth, but practical manufacturing involves employing a multilevel-step spiral phase plate (ML-SPP). In contrast to the ideal SPP, the ML-SPP's thickness no longer ascends uniformly but rather in discrete phase increments. If the ML-SPP comprises N phase steps, then the phase disparity between two successive orders is $2\pi l/N$.

The spiral-phase-plate technique is widely employed for producing vortex, offering high efficiency and the ability to process high-power laser beams. However, it is limited by generating solely one-order vortex beams in theory. Additionally, it lacks flexibility in controlling the parameters and varieties of OAM beams. Furthermore, the manufacturing and processing methods for SPP demand rigorous standards and entail higher costs.

2.2 **Q-plate method**

The q-plate, detailed in [29, 30], It comprises a liquid crystal panel with consistent birefringence phase retardation δ, along with a transverse optical axis configuration distinguished by a non-zero topological charge. The angle $\alpha(r,\phi)$, which represents the orientation of the optical axis concerning the x-axis in the $x-y$ plane, can be expressed as $\alpha(r,\phi) = q\phi + \alpha_0$. Here, α_0 denotes the initial optical axis orientation. Figure 2-2, displays various q-plate patterns with different q and $\alpha_0$values. When precisely adjusted ($\delta = \pi$), the q-plate can alter an incoming light beam, causing a topological

charge shift $\Delta = \pm 2q$. For instance, when a circularly polarized beam undergoes a tuned q-plate with $q = 1$, it produces a helical phase front displaying topological charges = ±2, contingent upon the input polarized light, as illustrated in the Figure 2-2 (e).

Q-plates are recognized for their capacity to generate OAM by converting optical spin into orbital angular momentum, in accordance with the conservation law of angular momentum. When $q = 1$, the highest attainable topological charge remains limited to 2. Essentially, the q-plate operates as a Berry phase optical component [31], controlling the wavefront shape by manipulating the polarization state. it's important to note that the q-plate, made of liquid crystal, has an energy threshold and may not be suitable for use with high-power laser beams. Besides its high price the q-plate, serving as a device for converting SAM into OAM, is not recommended for OAM communications application due to its limitations in achieving higher maximum topological charges. Instead, it finds more suitable applications in tasks related to particle manipulation.

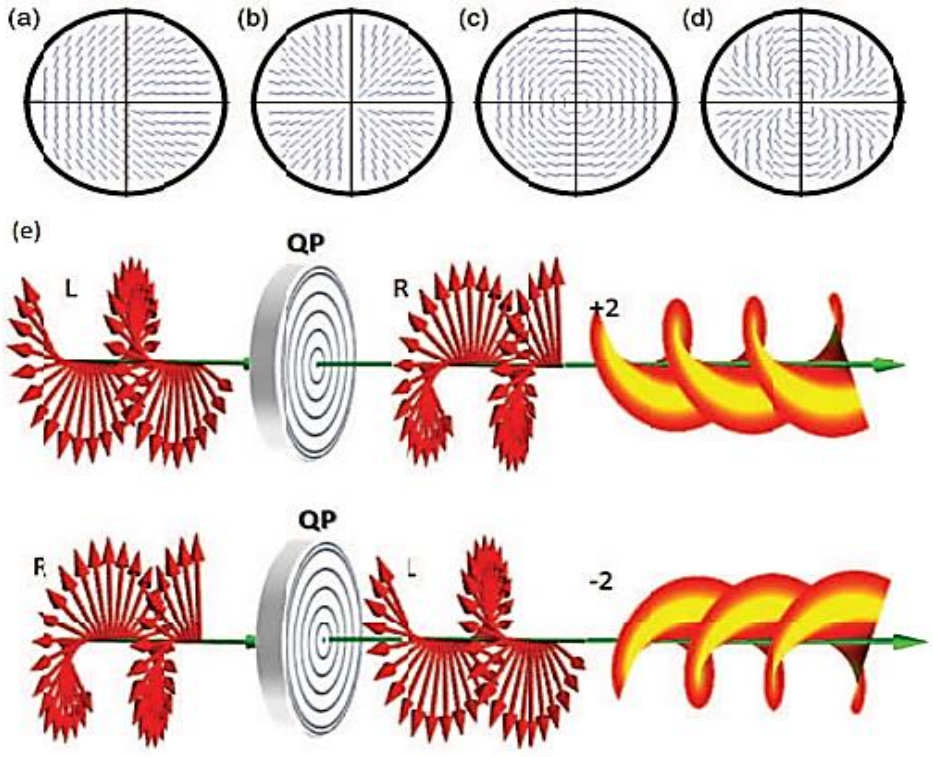

Figure 2-2: Four examples of q-plate patterns with: (a) (q, α0) = (1/2, 0), (b) (q, α0) = (1, 0), (c) (q, α0) = (1, π/2) and (d) (q, α0) = (2, 0). The segments indicate the optical axis orientation in the transverse plane. (e) Pictorial illustration of the optical action of a tuned q-plate with q = 1 on an input circularly polarized plane beam. A left-circular (or right circular) polarized Gaussian beam passing through a tuned q-plate with q = 1 turns into a helically phased beam with l = +2 (or l = −2) and right-circular (or left-circular) polarization (Figure adapted from [30]).

2.3 **Computer generated holography (CGH)**

A hologram essentially serves as a synthetic representation of an object, captured using specific plates that store the optical field information for reproducing desired objects. These plates record the interference pattern resulting from the superimposition of the object's optical field and a coherent reference beam. Consequently, when illuminated by a beam mirroring the reference beam's characteristics, an image of the object emerges. Holographic plates find applications in both transmission and reflection, although I'll focus solely on the former here. holography was invented in 1948 by Gabor [32]. Back then, the production of holographic plates faced limitations due to the lack of coherent sources necessary for stable interferograms. Substantial progress in holographic techniques occurred following the emergence of laser sources in the Sixties. Presently, two distinct types of transmission holographic plates have been developed, including the on-axis Gabor holograms. [33] and the off-axis Leith-Upatnieks holograms [34]. A Gabor hologram generates both virtual and real images of an object along a single axis, resulting in an observer perceiving a combined view of the two images. In contrast, Leith-Upatnieks holograms enable the separation of these images by introducing an offset angle between the reference wave and the light scattered by the object within the holographic plate.

In the mid-Sixties, the synthesis of holographic plates experienced significant advancements, thanks to the integration of computer technology [35]. Computers played a crucial role in simplifying the calculation of the complex amplitude of the optical field propagated from the object to the hologram plane. This calculated complex amplitude is then encoded as a real non-negative function, represented as a matrix of points with real values.

The utilization of computer technology in holographic plate synthesis comes with several advantages. Notably, it circumvents issues related to the coherence of the source of the reference beam and environmental conditions such as vibrations and turbulence. This increased robustness enhances the reliability and applicability of holographic patterns.

One important feature of computer-generated holograms is their capability to reproduce optical fields of diverse nature, including intricate light beams. This characteristic has positioned computer-generated holograms as invaluable tools for producing and studying light beams carrying orbital angular momentum [36-39]. This versatility not only expands the possibilities in holography but also opens up avenues for exploring and understanding the complex nature of light interactions in various applications.

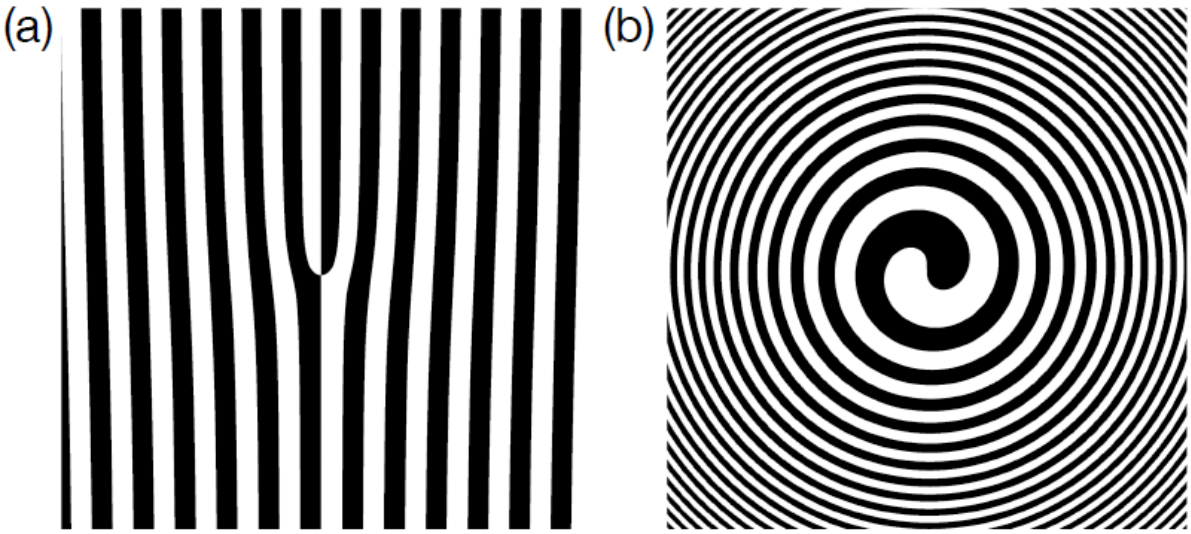

Figure 2-3: Examples of computer-generated hologram (numerically simulated) designed to produce optical vortex with $\ell = 1$. (a) a fork hologram, (b) Spiral hologram.

The holographic pattern obtained by computing the interference of the reference wave with a vortex beam is different if the former is a plane wave or a spherical wave. In the first case, the pattern of the interferogram is similar to that of a grating with a central fork-shaped dislocation [40]. This is the reason why they are usually called fork holograms. Figure 2-3 (a) shows an example of a fork hologram with just one central dislocation. When a plane wave with a wavelength λ intersects perpendicularly a fork hologram, the grating structure ideally produces an infinite number of diffraction orders, the share of optical power between different diffraction order depends on amplitude and phase modulation. The angle θ_m subtended by the direction mth diffraction order with respect the propagation axis of the input beam is given by the usual grating equation [41]

$$\Lambda \sin \theta_m = m \lambda \tag{2-3}$$

where Λ is the pitch of the grating far away from the center. Instead, if the reference beam is a spherical wave, then the interferogram pattern will assume a spiral-like shape similar to that of a Fresnel zone plate [42] (see Figure 2-3 (b)). Such a spiral hologram diffracts an incident beam too, but the diffraction orders are found at different positions along the propagation axis. For the purposes of the experiments that will be discussed later, fork hologram is more useful than spiral holograms because it is always possible to simultaneously inspect different diffraction orders without changing the position of the observation plane. Therefore, in the following I will present only the properties of fork grating.

The object that we desire to reproduce is a l-charged vortex beam having an optical field:

$$U_O = u_O \exp(i\ell\varphi) \tag{2-4}$$

where u_O is a real amplitude factor and $\varphi = arctan(y/x)$ is the azimuthal angle in the (x, y) plane perpendicular to the z axis. The reference beam is represented by a plane wave with a constant amplitude u_0 and a wave vector k lying in the (x, z) plane that subtends an angle ψ with the z axis. The corresponding field distribution is

$$U_R = u_R \exp(-ikx \sin\psi) = u_R \exp(-i \frac{2\pi x}{\Lambda}) \tag{2-5}$$

where $\Lambda = \lambda / sin\psi$. Assuming for simplicity $u_O = u_R$= u, the interferogram produced by the two fields is:

$$I(x,\varphi) = |U_O + U_R|^2 = 2u^2 \left[1 + \cos\left(\frac{2\pi x}{\Lambda} + \ell\varphi\right)\right] \tag{2-6}$$

This represents the interference pattern that has to be imprinted in the holographic plate to obtain a fork hologram. Equation (2-6) may be used also to describe the transmission function of a Hologram. In this case, Λ has to be identified with the pitch of the grating away from the center. Another computationally convenient expression can be derived by employing Fourier transform techniques [43]:

$$T(r,\varphi) = \sum_{n=-\infty}^{\infty} T_n \exp\left[-in\left(\ell\varphi - \frac{2\pi}{\Lambda} r\cos\varphi\right)\right] \tag{2-7}$$

Where $rcos\varphi = x$. When such hologram is illuminated with a plane wave, the beam containing the optical vortex having the desired topological charge l is generated at the first diffraction order ($m = +1$). More generally, a beam formed at the mth diffraction order possess a vortex beam with topological charge equal to ml.

The holographic plate in which a fork hologram is recorded can modify either the amplitude and the phase of an incident light beam. The latter are preferable for experimental reasons because they have a lower energy absorption and a higher diffraction efficiency. To obtain a phase hologram, the transmission function has to be translated into a variation of the thickness of the hologram material. Furthermore, the spatial resolution must be sufficiently high to resolve the interference fringes.

To fabricate CGHs, an enlarged sample of the computed hologram is plotted. Then a photographic reduction forms the hologram with the desired final size. In recent years, CGHs have been fabricated by direct writing with a laser beam system or electron beam lithography system to benefit of a resolution impossible to reach with photographic techniques. The most important factor that affects the efficiency of printed CGHs are line numbers which are related to the resolution. The challenge with printing CGHs lies in their time-consuming nature, static characteristics, and occasional limitations in resolution. However, in recent years, advancement in electro-optical modulator technology, such as spatial light modulators (SLM), has provided a solution for rapid, dynamic, high resolution and digital manipulation of the amplitude or the phase of light beam. SLM, a computer-controlled device with small pixel size, serves to modulate or manipulate various properties of light, including amplitude, polarization, and phase. The typical dimension of individual pixels on the SLM can range between 3.5 μm to 35 μm. Each pixel's optical phase retardation covers a range from [0, 2π) with 256 steps, correlating to a Gray Level color scale. This scale is attained through voltage modulation from a computer graphics card. Upon displaying a hologram with precise dimension and phase depth modulation on the PC screen, a corresponding voltage, in line with the pixel's color in the gray scale level, is applied to the relevant pixel on the SLM. This action modifies the liquid crystal alignment within the cell, thereby altering its optical retardation. The displayed hologram pattern can be altered by changing the pattern on the screen. Nonetheless, the speed of the SLM is limited by both the graphic card and the response time of the liquid crystal molecules. Additionally, its effectiveness is notably contingent upon the polarization state of the beam. The SLM finds widespread use across various applications, particularly in scenarios that demand dynamic control over beam shapes, as in the realm of optical tweezers [44] and optical trapping [45].

An electrically addressed nematic SLM comprises a layer of birefringent liquid crystals. On one side, there is a transparent electrode, while on the other side, there are silicon-pixilated electrodes. The magnitude of the applied voltage to the nearest pixelated electrode can influence the orientation of the LCs at a specific location. Consequently, in the absence of an electric field, the LCs align in a preferred orientation.

As the applied electric field increases, the orientation of the LCs begins to align with the considered electric field. This alignment is crucial, as it allows the refractive index of each pixelated electrode to be controlled by modulating the voltage applied to the individual silicon pixelated electrodes in the LC displays. This dynamic control over the refractive index enables precise manipulation of the optical properties, providing a versatile platform for various applications in display technology (Figure 2-4).

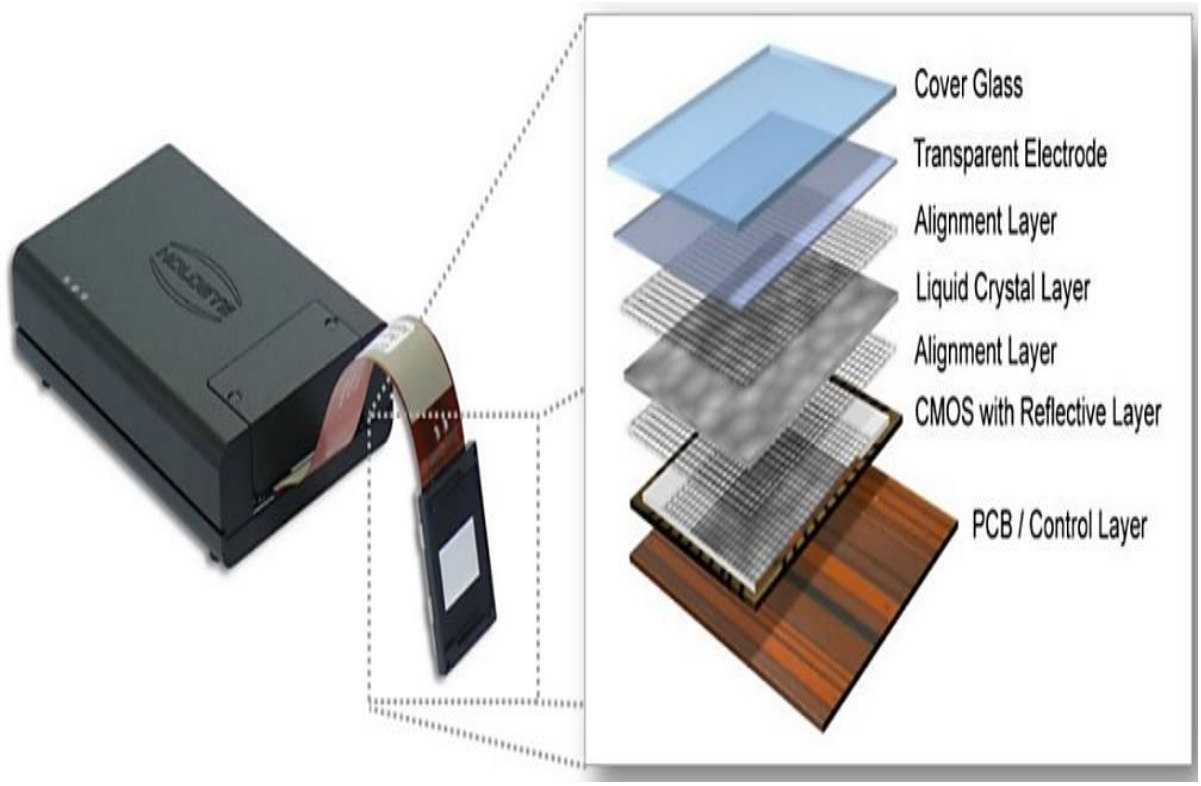

Figure 2-4: Left: photo of the device: Holoeye, PLUTO - phase only SLM. Right: Sketch of SLM display assembly. Both images are taken from the Holoeye web page. (www.holoeye.com).

2.4 Detection of orbital angular momentum of light

The content in this section is sourced from Chapter 13 of the book [46] on the measuring OAM of light. In this section, I'll review few established methods employed to detect the OAM state. For additional methods of detecting OAM, reader can refer to the mentioned book.

In the preceding chapter, I introduced the concept of light's orbital angular momentum and delved into numerous applications. The OAM inherent in light stands as a highly valuable optical trait with widespread applications across various optical domains. However, this advantage poses a significant challenge in devising adequate detection methods, given the utilization of N modes, leading to an N-dimensional state space. Achieving comprehensive detection of all potential N states (see Figure 2-5) becomes essential to effectively resolve the issue with OAM. In this regard, a method's efficacy is gauged by its capability to successfully identify as many OAM modes as possible.

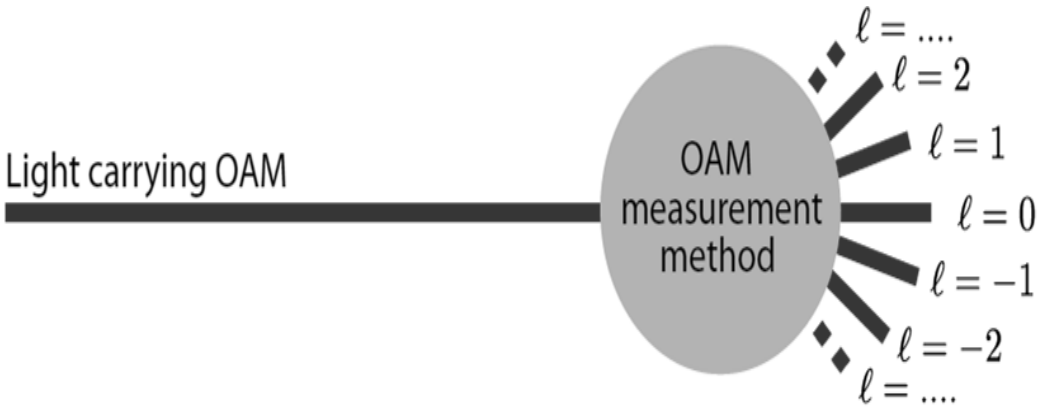

Figure 2-5: An optical vortex beam carries an OAM with a value of $\ell\hbar$ per photon. ℓ, theoretically, can span any integer, providing a broad spectrum of potential outcomes.

This unresolved issue necessitates the creation of a direct and highly effective method for measuring OAM. These experimental techniques encompass measurements involving torque on micro particles [47], spiral interference fringe counting [48] and diffraction through apertures [49], among many others. The existing methods exhibit diverse strengths and limitations, considering factors like complexity, resilience to misalignment, and their ability to detect higher-order OAM. Nonetheless, finding a straightforward and efficient solution akin to the effectiveness of the polarizing beam splitter in measuring spin angular momentum remains a challenge.

As previously emphasized, spin angular momentum is fundamentally binary, directly linked to the polarization state of light. In the case of left and right circularly polarized beams, the spin angular momentum per photon is represented as $\sigma\hbar = \pm 1$, respectively. The detection of SAM can be achieved using a polarizing beam splitter, where circularly polarized light undergoes transformation by a λ/4 wave-plate into either a p- or s-polarized state.

This modified state is then either transmitted or reflected, resulting in one of two distinct outputs, as illustrated in Figure 2-6. This process provides a practical means for discerning and manipulating spin angular momentum in optical systems, with applications ranging from communication to quantum information processing.

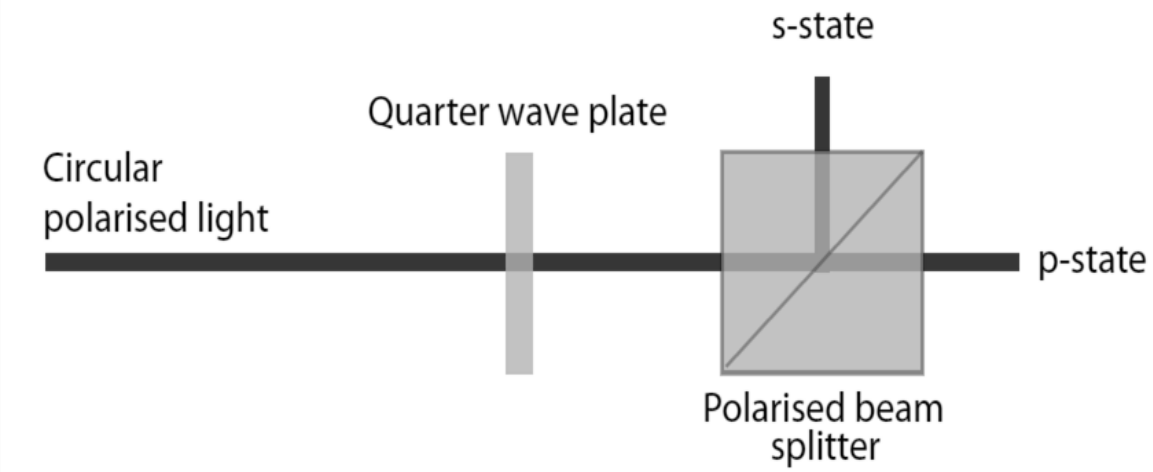

Figure 2-6: transformation of a circularly polarized light using a quarter-waveplate into linear states. Subsequently, a polarizing beam splitter transmits p-polarized light and reflects s-polarized light, yielding two outputs for determining the polarization state.

2.4.1 Spinning trapped particles

As previously mentioned, He et al. investigated the transfer of OAM to trapped microscopic absorbing particles within optical tweezers. Optical tweezers operate by utilizing a force linked to the intensity gradient in the waist of focused light beam: dielectric particles are drawn towards regions of heightened strength, enabling the trapping and manipulation of microparticles [10, 47]. When employing helically-phased beams for trapping, particularly with a beam waist comparable to the particle size, the focal point of attraction aligns with the vortex position within the beam. Initial investigations on torque exerted by OAM-carrying beams involved employing black micron-sized CuO particles, observed to rotate upon trapping using a plane-polarized LG beam. Subsequent studies combined the torque attributed to OAM with that resulting from the spin angular momentum of circularly polarized light [10]. A dielectric particle absorbs incoming light, acquiring angular momentum in the forms of SAM or OAM, consequently exerting torque on the particle. Helically structured beams add to the torque induced by circular polarization. In the paraxial limit, the particle's interaction is influenced by both the beam's polarization and helicity, leading to torque.

$$\Gamma = \frac{P_{abs}}{\lambda}(\ell + \sigma_z) \qquad (2\text{-}8)$$

P_{abs} is the absorbed power by the dielectric bead, λ represents the light's wavelength and σ_z is the is the light's handedness for polarization. Torque applies to a particle even with individual photons; each

photon in the beam carries an OAM of $\ell\hbar$. In simpler terms, the total torque on a particle can be calculated by multiplying the photon flux by the helical beam's angular momentum. or LG beams, the total angular momentum per photon is $(l + \sigma_z)\hbar$. Simpson et al. discovered that the torque from $l = 1$ OAM and that of polarization $\sigma = -1$ can cancel each other [12].

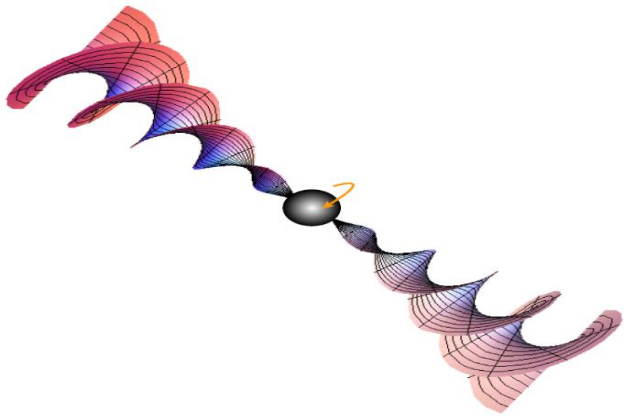

Figure 2-7: Focused helically-phased beam trapping a dielectric bead. A partially absorbing bead absorbs the OAM resulting in torque (Figure adapted from [46]).

Particles trapped in optical tweezers are usually in a viscous material, normally water, which will cause a rotational drag resulting in slower spinning. In the simplest case, this drag is proportional to the angular velocity of the particle. A measurement of the optical torque can be made when an equilibrium of the rational drag and applied torque is reached. This measurement can be captured using a high speed digital camera or a photo diode at the edge of the trapped particle measuring a flashing as the particle spins. From this rotation and knowledge of the viscous medium, the torque is calculated and can then be used in Equation (2-8) to calculate a measurement of the number l. After the initial experiment by He et al., beams carrying OAM have become useful as optical spanners and many other tasks. This method can be used to determine the OAM of an unknown input beam through the measurement of the rotation speed, when the viscous drag of the liquid and polarization state of the light are known [12]. However, this method is not optically efficient for determining OAM. It necessitates a high-power laser source to induce measurable rotation in the absorbing material, alongside a high-speed camera to capture the particle movement.

2.4.2 Counting spiral fringes using interferometry

As previously noted, beams with OAM exhibit a helical phase structure, which can be unveiled through interference, manifesting as spiral fringes [48]. This technique extracts phase information from an incoming beam and holds relevance in numerous experimental setups, including those dealing with speckle fields [50] and beams featuring displaced vortex positions [51]. The fundamental principle underlying this technique is simple: within a Mach-Zehnder or a comparable interferometer (shown in Figure 2-8), a plane-wave as a reference beam intersects with a helically phased source beam.

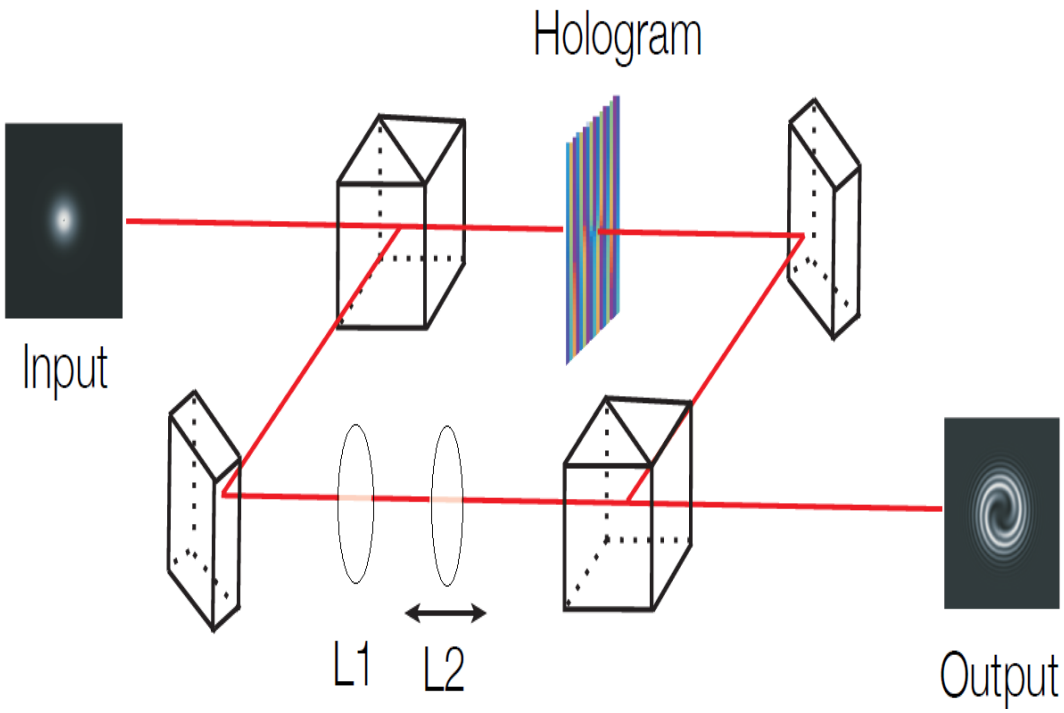

Figure 2-8. A Mach-Zehnder interferometer where a beam containing OAM is generated in one arm of the interferometer through the use of a hologram. The fringe pattern is changed from a petal pattern to a spiral fringe pattern by changing the distance between lens L1 and L2, as this alteration changes the curvature of the phase front in the reference arm (Figure adapted from [46]).

This configuration ensures that the observed fringes solely originate from the relative phase structure of the source beam. When using a vortex beam, with a phase structure of $exp(il\varphi)$, each fringe denotes a progression of 2π enabling the determination of the value l, as seen in Figure 2-9. The observed pattern relies on the phase front's curvature: matched curvatures exhibit petal patterns at the beam waist, while differing curvatures yield spiral fringes. For Laguerre-Gaussian laser modes, encompassing both helical phase term l and radial term p, the radial components manifest as radial nodes in the interferogram.

The count of these nodes equals $p + 1$, depicted in column three of Figure 2-9. Superpositions of LG laser modes result in interleaved spiral fringes, seen in column four of Figure 2-9.

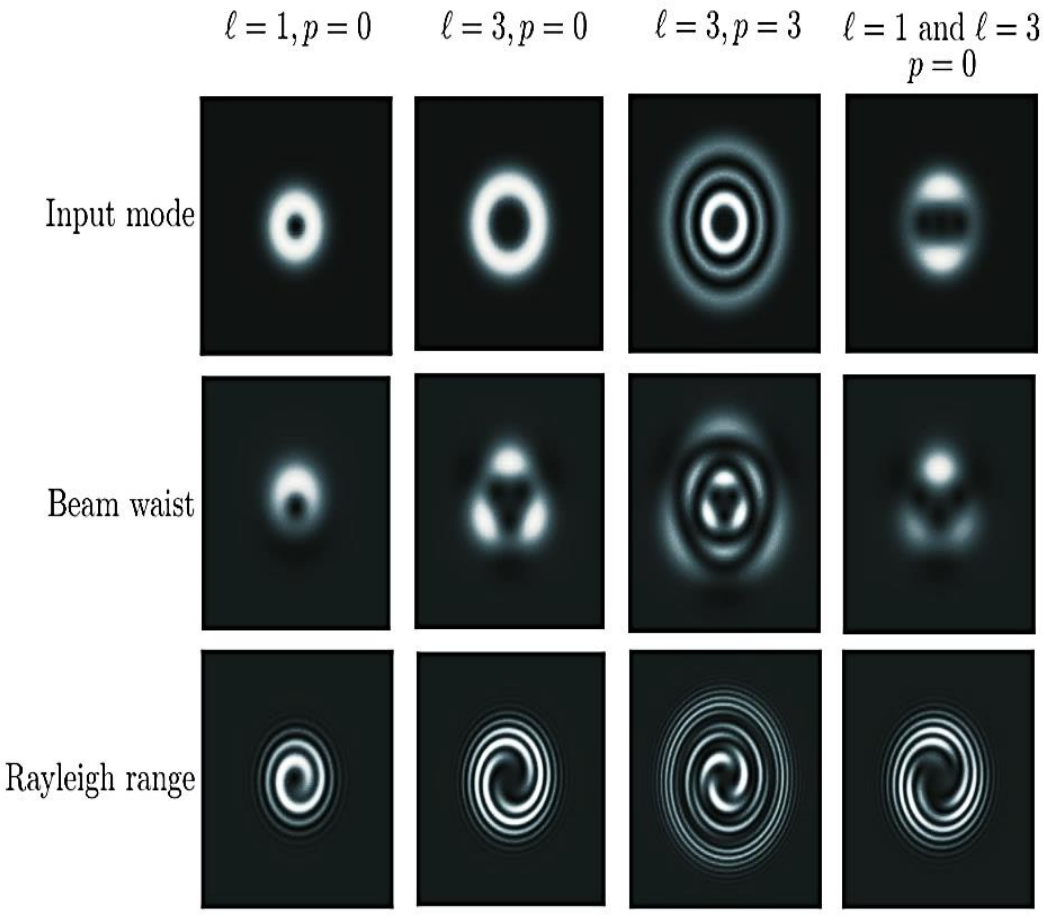

Figure 2-9: Interference occurs between an LG beam (representing OAM with ℓ as azimuthal and p as radial components) and a uniform plane-wave at the beam waist and Rayleigh range. The shown interferograms display different input modes: rows one and two feature helically phased modes without a radial component p, row three showcases a mode with radial lobes, and column four exhibits a combination of two distinct helically phased beams (Figure adapted from [46]).

Interference techniques applied to intricate structures involve creating a detailed phase map of the source. Dark regions in the interference pattern might pose uncertainty about the phase value, as they could stem from reduced intensity or destructive interference. Adjusting the phase of the plane-wave reference provides additional insights into these areas. Each pixel serves as an independent intensity measurement, measured across multiple phase steps, typically 16 or 32. Over a 2π range, these steps induce sinusoidal intensity changes; the starting point of this sinusoid indicates the phase of that specific pixel. From a computational perspective, this method allows fast execution, enabling tasks like tracking

vortex positions within speckle fields. This capability further facilitates studies exploring the topology of vortex lines within such fields.

Interferometric methods allow the OAM content of unknown LG mode to be easily determined. These are very useful techniques and have many applications, However, this method involves complex setups and it is highly sensitive to issues such as dust or scratches on optical elements. Additionally, it has limited tolerance for beam misalignment. The necessity for an appropriate reference beam imposes stringent constraints on the applicability of two-beam interference techniques. In numerous scenarios where OAM measurements are desired, this becomes challenging and, in certain instances, unfeasible. For instance, this limitation poses challenges in detecting sources from astronomical objects.

2.4.3 Diffraction effects from apertures

A method not requiring a reference beam involves diffracting light through apertures. Hickmann et al. (see Figure 2-10) [49] showed that when a helically phased beam hits a triangular aperture, it forms a triangular pattern of constructive interference spots. The number and arrangement of these spots relate to the input's l value.

This approach can be understood by modeling the diffraction pattern generated from the aperture. The resulting interference effects emerge from the light diffracted at each side of the aperture. Specifically, in the context of helically-phased beams, phase shifts that occur along the edges of the triangle are directly correlated with the input beam's l value. The intricate phase structure at the edge creates an interference pattern based on l, wherein an increase in the mode index adds an extra layer of spots to the interference pattern, as illustrated in Figure 2-10.

The triangular pattern undergoes rotation concerning the aperture due to the helical characteristics of the input mode. When the sign of l is altered, this rotation direction reverses. Utilizing a singular aperture offers a sophisticated means of measuring the OAM value associated with an input mode. This technique expands its scope beyond triangular apertures and has recently been applied using a hexagonal aperture. In this setup, lines are created that maintain a consistent intensity, and the quantity of these lines corresponds to the l mode index of the input mode [52]. Berkhout et al. independently devised an alternative method utilizing a circular arrangement of pinholes to generate diffraction patterns. The pattern structure of these diffractions depends on the mode structure of the input beam. [53] (see Figure 2-11). The arrangement of these pinholes drew inspiration from the configuration of

telescope arrays, aiming to facilitate the assessment of the OAM characteristics within light emitted from celestial sources. These assemblies of pinholes are referred to as a multipoint interferometer (MPI).

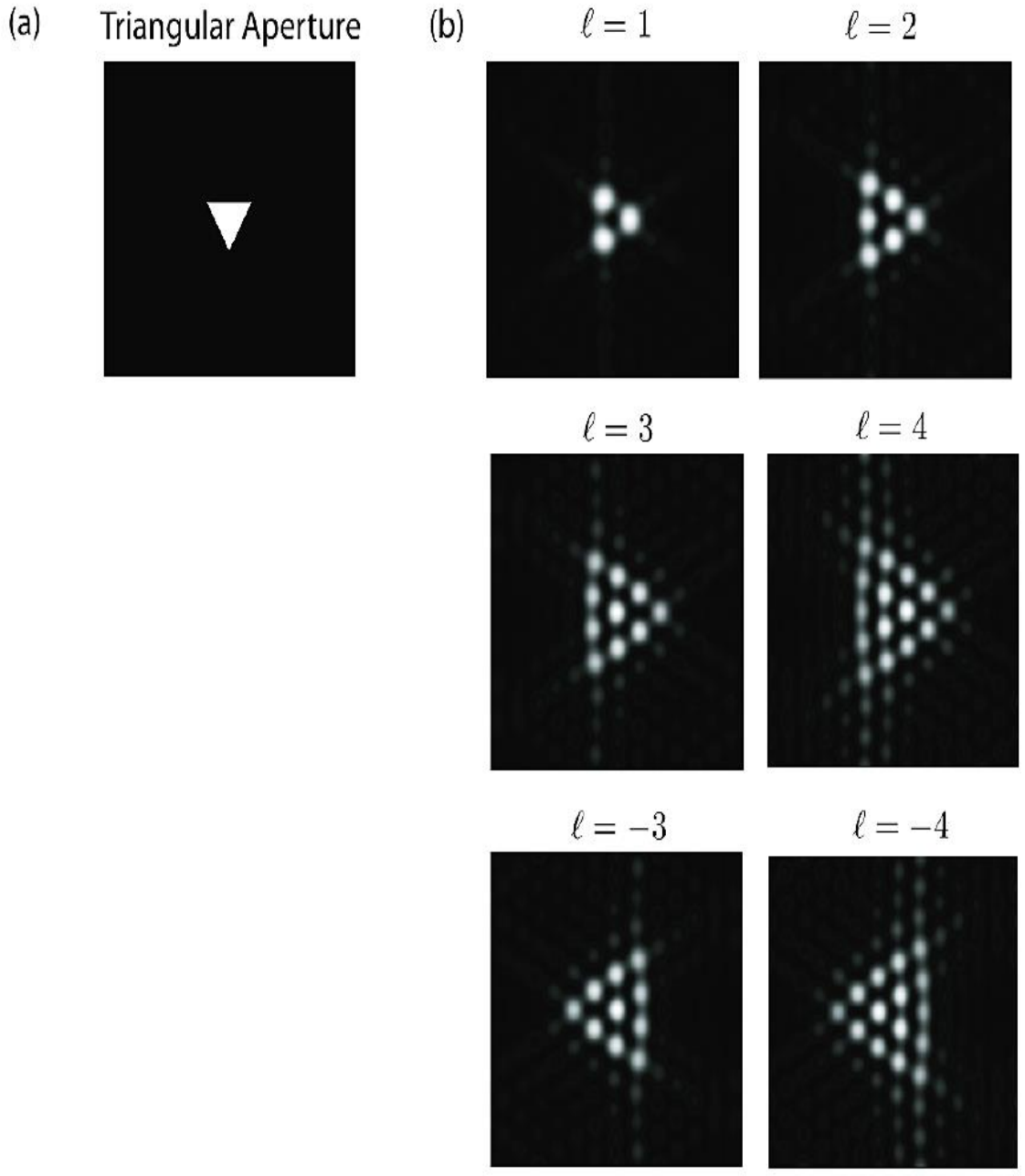

Figure 2-10: (a) An equilateral Triangular aperture. (b) The diffraction pattern at far-field resulting from the LG beams passing through the aperture for different l values. Simulated images shows the initial outcomes presented by Hickmann et al.

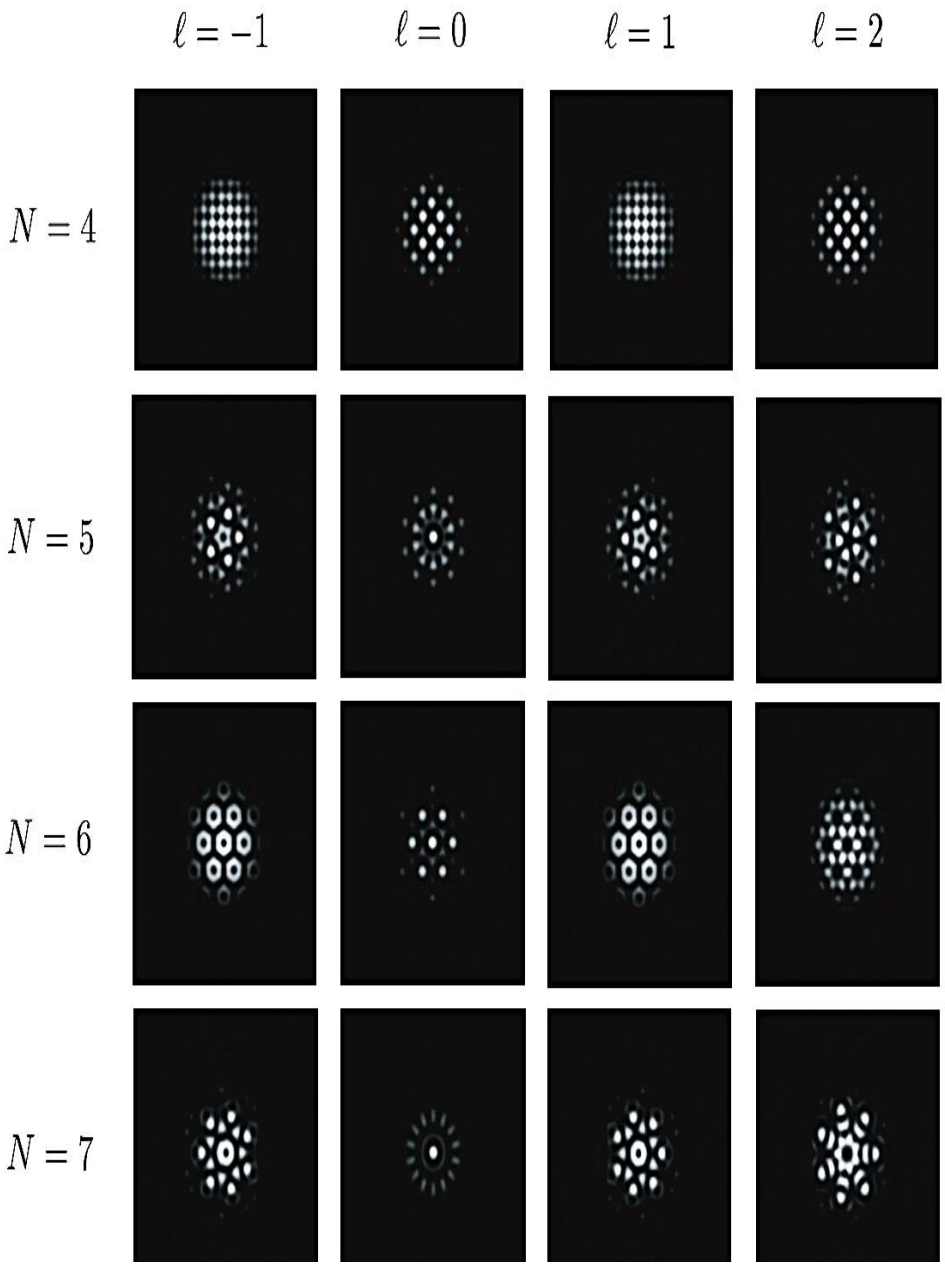

Figure 2-11: Diffraction patterns emerge when a helically phased beam carrying a topological charge traverses N-pinhole multipoint interferometer (MPI). These images are attributed to G.C.G Berkhout.

Experimental demonstrations confirmed the ability to measure the OAM state of partially coherent light. By using a set of pinholes illuminated with a central vortex beam, sampling of the phase value at fixed locations around the beam axis is achieved. Each pinhole acts as a point light source, and this setup's analysis generates the resulting far-field diffraction intensity pattern,

$$I_{\ell}^{N} \propto \left| \sum_{n=0}^{N-1} \exp(-i\,\ell\,\alpha_n) \times \exp\left(i\,\frac{ka}{z}(x\,\cos\alpha_n + y\,\sin\alpha_n) \right) \right|^2 \tag{2-9}$$

where I_{ℓ}^{N} is the far-field intensity of the MPI, N is the number of pinholes, k is the wave number, a is the radius of the circle of pinholes and $\alpha_n = 2\pi \mathrm{n}/\mathrm{N}$ is the azimuthal co-ordinate of the nth point.

The effectiveness of this technique in measuring OAM strongly correlates with the quantity of pinholes employed, as illustrated in Figure 2-11. The reliance on the number of pinholes can be comprehended concerning the phase sampling undertaken at each pinhole. In cases involving two or three pinholes, any phase difference among the pinhole positions in a helically phased beam might similarly arise from a suitably inclined plane wave.

Thus, this method is truly effective with four or more pinholes positioned along the input mode's central axis. Specifically, using four pinholes allows the multipoint interferometer (MPI) to distinguish odd and even OAM states. Changing the mode index results in an alteration of the diffraction pattern's orientation. Hickmann et al. and Berkhout et al.'s aperture-based methods present attractive options for measuring the OAM content of a specific source when simplicity is key. However, these techniques are sensitive to input beam misalignment, posing practical challenges in scenarios which demand high optical tolerance. Furthermore, these methods require a substantial number of photons in a similar state to achieve precise OAM measurements, inherently leading to inefficiencies in the measurement process.

2.4.4 Diffractive holographic filters

Optical systems inherently operate in a reversible manner, enabling the utilization of an OAM generation method as a means to measure OAM. The initial successful generation of OAM-carrying beams occurred in 1992 by Allen *et al*, employing a pair of cylindrical lenses [5]. Subsequently, Beijersbergen et al. [28] devised helical phase plates to accomplish a similar objective. Before Allen's identification of OAM in twisted beam, Heckenberg et al. demonstrated the use of computer-generated holograms for producing beams incorporating phase singularities [54].

Holograms have evolved into a customary tool for generating OAM-carrying beams. In 1990, Bazhenov et al. pursued a methodology based on a diffraction grating to generate multiple orders carrying the desired phase pattern [55]. These holograms can be perceived as the product of the vortex

term $exp(il\varphi)$ and a phase-ramp term $exp(ik\ sin(\psi)x)$, with filtering based on phase values. The formation of the l-forked pattern was inspired by the interference pattern between a beam having a phase singularity and a tilted plane wave, giving rise to distinct pattern.

In 1992, Heckenberg et al. centered their exploration on the spiral zone plate as the fundamental principle underlying the holograms they studied. These spiral zone plates comprised binary concentric circles featuring a singularity at the center, functioning similar to a Fresnel zone plate but with a dislocation at the central region [54]. The number of intertwined circles establishes the strength of singularity's charge. These zone plates can be understood as the phase emerging from the multiplication of the vortex term $exp(il\phi)$ and a lens term exp(*ikr*2/(2*f*)). These gratings have demonstrated efficacy in producing singularities, yet they encounter an issue with insufficient separation among the distinct diffraction orders

Mair *et al*. demonstrated the reversible nature of this generation technique (see Figure 2-12), by directing a specific diffraction order into a single-mode fiber [14]. In this approach, the hologram, together with the fiber's entrance aperture, acts as an OAM filter. Mair et al. employed this method to exhibit the entanglement of OAM in pairs of photons derived from a non-linear crystal. Presently, this strategy is widely employed for detecting OAM in quantum optics experiments at the single-photon levels.

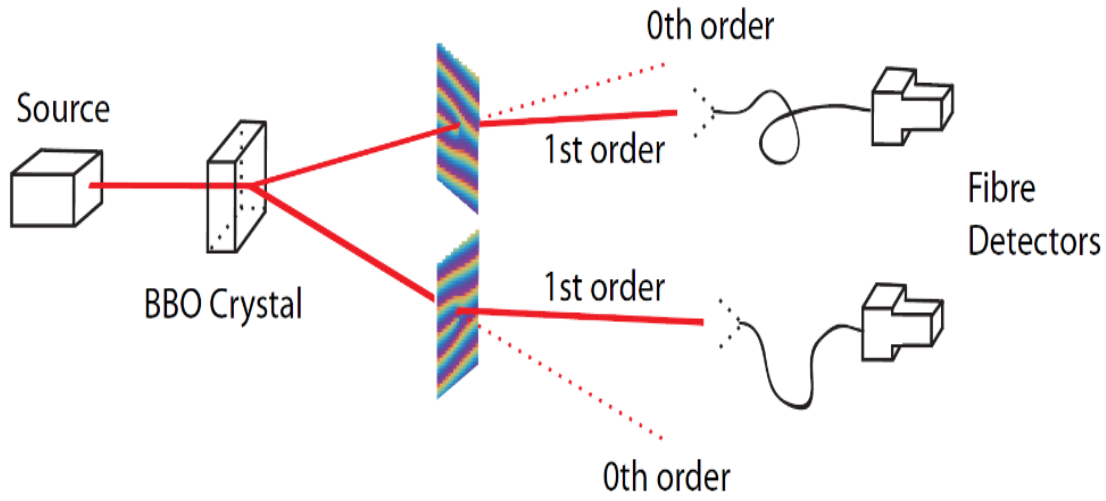

Figure 2-12: A schematic depiction of the arrangement utilized to couple entangled photons from a BBO down-conversion crystal, carrying a particular OAM content. A photon exhibiting the precise ℓ value transforms into a Gaussian mode within the primary order, subsequently registering at the fiber detector (Figure adapted from [46]).

2.4.5 More complex holograms

OAM's potential for high-bandwidth free-space communication has drawn considerable interest. Researchers are exploring its stability in turbulent atmospheres and its applicability for communication with space-based receivers. Gibson et al. introduced a communication system using two interleaved l-forked holograms, generating a 3×3 grid of diffraction orders to assess different l values within incoming beams [16]. The system effectively quantified the OAM content across eight l modes within a fifteen-meter range. Khonina et al. used this technique in 2000, involving the combination of two diffractive elements, each representing a different l value [56]. Gibson's research mirrors that of Mair et al. [14], wherein an l-forked hologram transforms an $exp(il\phi)$ beam into a planar phase-front beam.

By optimizing a hologram, specific diffraction orders can be generated. Gibson et al. harnessed this capability by optimizing the hologram to generate the -1, 0, and +1 orders, see Figure 2-13.

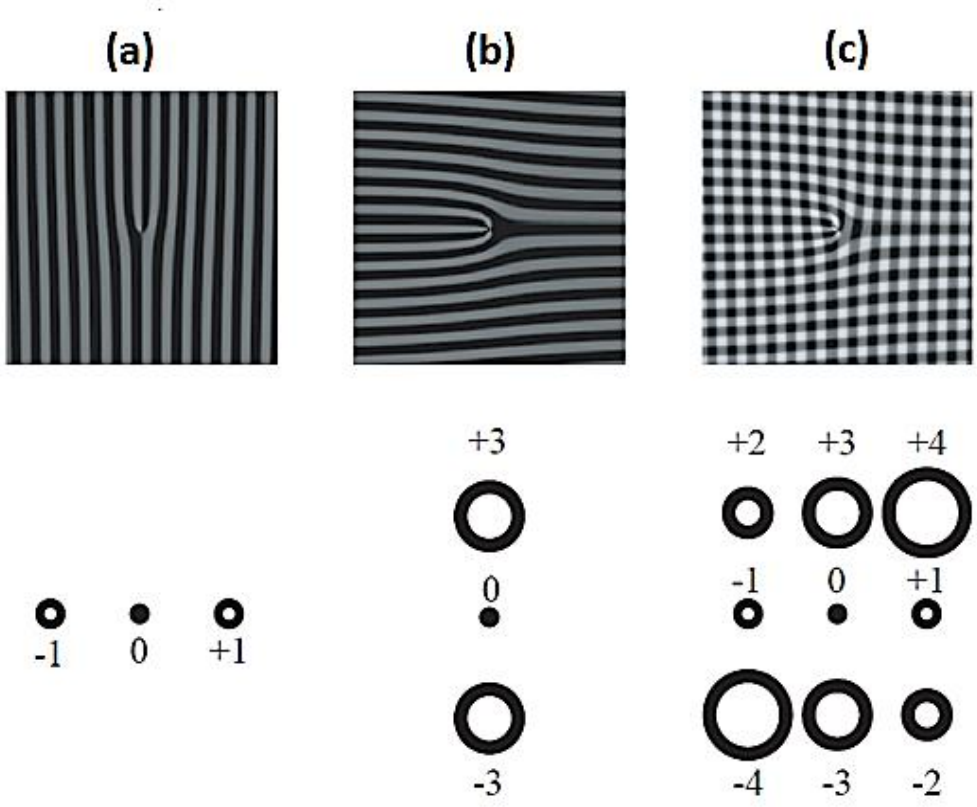

Figure 2-13: (a) The hologram's phase can be refined to equally weigh the power of the first and negative first orders. (b) A π/2 radians rotation corresponds to a similar shift in the diffraction orders' positions, as displayed above. This adjustment enables an increase in the charge to higher l values. (d) Combining the patterns showcased in (a) and (b) through addition yields the intended nine-order pattern, creating a spectrum of l-valued beams.

When an OAM-carrying beam hits hologram, the l mode will be detected. A similar modulation can be vertically done by rotating the linear phase by 90 degrees. Combining these two patterns creates multiple vertical diffraction orders for each horizontal order, each with an added l value. For instance, if the initial positive order in each hologram is $l = 1$, the first vertical order associated with that horizontal order becomes $l = 2$, while the negative first vertical order corresponds to $l = 0$. Combining horizontal and vertical patterns forms a grid for potential l readings. When an helical beam interacts with this pattern, a spot appears at the center where the beam's l value and the diffraction order add up to zero (Figure 2-14). The method evenly spreads the input power across all nine diffracted orders. Its efficiency is linked to the number of modes being detected—more modes decrease the method's effectiveness. When combining multiple l modes, this results in two or more bright central spots. The brightness of each spot tells us how much each mode contributes to the combination.

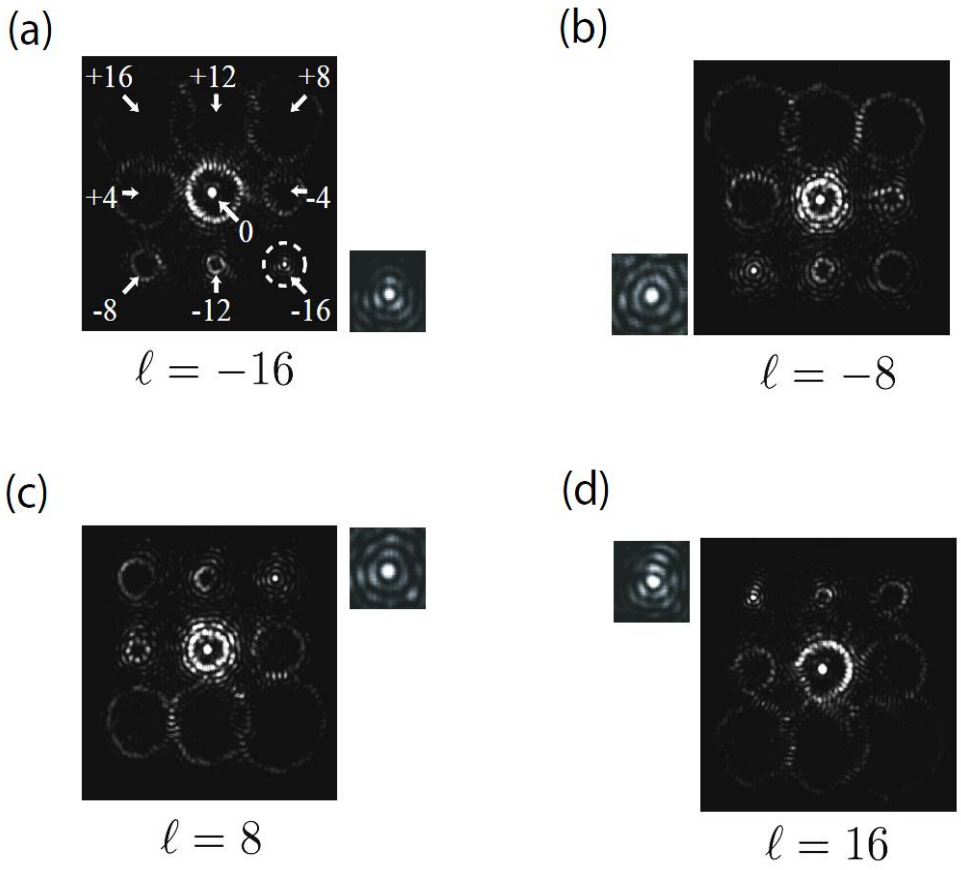

Figure 2-14: The far field observed when OAM modes with an ℓ = -16;-8; +8; +16 are passed through a hologram similar to that shown in figure 2.10 (d). Images courtesy of G Gibson [16].

Gibson et al. detected eight modes over fifteen meters. Their method, though simpler for measuring OAM, loses much input light to other beams, making it inefficient for single-photon measurements and radial modes associated to LG beam.

Although the challenges in OAM detection persist, the methods discussed here have been shown to be practical. This chapter doesn't comprehensively cover all techniques for OAM measurement. Methods like q-plates, Principal Component Analysis, and the use of Bessel beams as basis sets have had diverse success in addressing OAM detection issues [57, 58]. The quest for an OAM detection method that guarantees a 100% efficiency across all OAM modes is complex. Among the extensively researched techniques, spiral fringe interference patterns and hologram selectors stand out as notable approaches within the realm of optical detection for OAM. These methods have gained widespread adoption, but it's crucial to acknowledge their limitations. Interferometry, while being a commonly employed method with the potential to detect the two indices of LG beams simultaneously, poses challenges. It has a complex setup and low tolerance to beam misalignment, along with susceptibility to interference from dust or scratches of optical elements which can impede successful OAM detection. These vulnerabilities underscore the need for more versatile and robust detection methodologies in OAM detection, leaving room for innovative techniques to overcome these challenges.

3 Experimental generation of optical vortex beam

In this thesis, we utilize two types of Holoeye reflective spatial light modulators (SLMs): the HoloEye LETO and the HoloEye Pluto. The LETO version is a more recent version, while the Pluto version has been in use for over a decade. In a typical operation, computer sends computed phase information - created and encoded in Matlab—via a DVI or HDMI output. The SLM then displays this phase information as part of the operational process. We employed the Pluto SLM to generate optical vortex beams, while the LETO SLM was utilized for detecting OAM modes using a specially designed diffraction grating.

It's noteworthy to highlight that, as per the manufacturer's specifications, the Pluto SLM is a specialized color field sequential phase board kit utilizing the commercial Pluto 1 board. Despite the similarity in name, its liquid crystal on silicon is primarily tailored for color holographic reconstruction in the visible spectrum. Our investigation aimed to ascertain the Pluto SLM's response to diverse encoded hologram modulations and evaluate its diffraction efficiencies.

3.1 Holoeye LETO

The LETO SLM used in this study has full HD resolution (1920 x 1080 pixels) and uses liquid crystal on silicon microdisplay technology, with full HD resolution at 1920 x 1080 pixels. It features a 6.4 μm pixel pitch and a minimal interpixel gap of 0.2 μm, enabling a high fill factor of 93% and ensuring relatively efficient light transmission. Optimized for the visible spectrum, this SLM offers reflectivity ranging from 62% to 75% (dependent on wavelength) and operates effectively between 420nm and 700nm. With an AR coating limiting front reflection to less than 0.5% within this range, the SLM interfaces seamlessly as an external monitor using the standard HDMI interface of a graphics card. Notably, its small pixel size and high fill factor allow for the modulation of intricate phase patterns onto beams, crucial for the detection of LG modes. Our LETO SLM is shown in Fig. 3-1

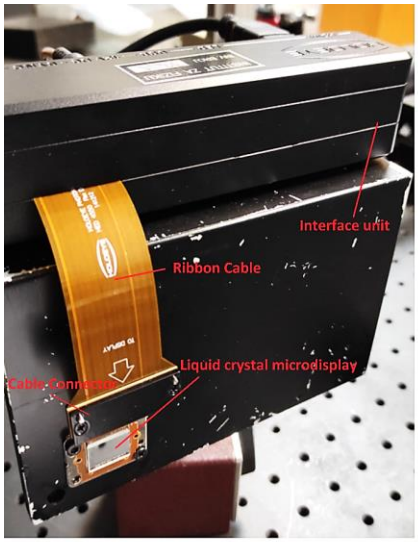

	SLM-LETO
Number of pixels:	1920×1080
Pixel pitch:	6.4μm
Display Area:	12.5×7.1 mm
Repetition rate:	60 Hz
Wavelength:	420 nm-1064 nm
Phase levels	256 (8 bit) gray level
Fill factor:	93%

Figure 3-1: Holoeye LETO SLM and its specifications

3.2 **Holoeye Pluto**

The Pluto SLM utilizes reflective micro displays, offering a resolution of 1920 x 1080 pixels with an 8 μm pixel pitch. Its active area spans 0.7" diagonally, featuring an aspect ratio of 16:9. The Pluto driver includes a DVI interface for CGH addressing and a trigger sync output to synchronize with external devices, like color-switchable lasers.

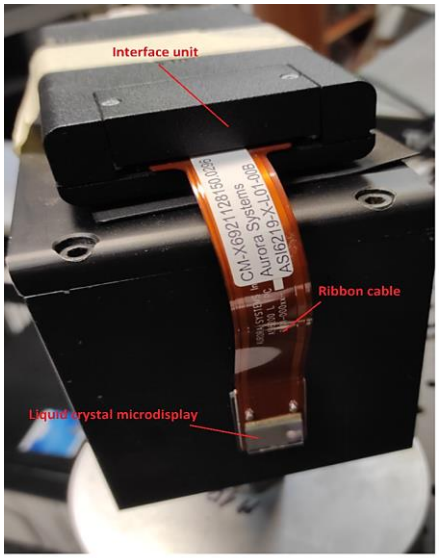

	SLM- Pluto
Number of pixels:	1920×1080
Pixel pitch:	8μm
Display Area:	15.36× 8.64 mm
Repetition rate:	60 Hz
Wavelength:	450-800 nm
Phase levels	256(8 bit) gray level
Fill factor:	87%

Figure 3-2: Holoeye Pluto SLM and its specifications

To facilitate the generation of complex structured light, we have developed a MATLAB code that serves as a versatile tool. This code facilitates the manipulation of crucial parameters for creating CGH, including the diffraction grating type, amplitude modulation and phase modulation, phase variation, amplitude visibility, grating period, and orientation (vertical or horizontal and diagonal or anti-diagonal).

As an example, the performance of the SLM Pluto is illustrated in Figure 3.8, depicting an optical holographic reconstruction of a complex amplitude hologram.

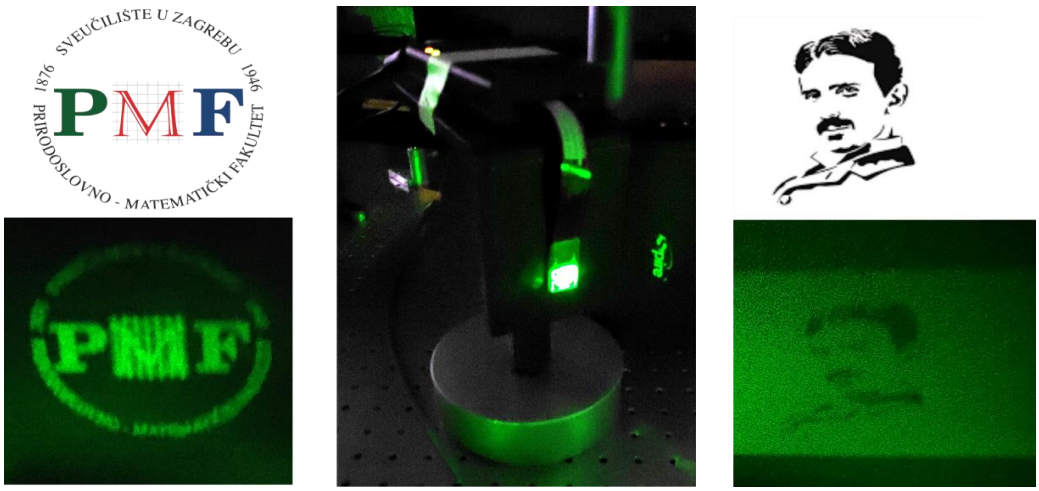

Figure 3-3: (a) Employing SLM for the optical holographic reconstruction of (b) PMF's logo and (c) a photograph featuring the renowned scientist, Nikola Tesla. (The original images are shown on top)

3.3 **Beam profilers**

For precise observation of intensity at the image plane, we used beam profilers, the Thorlabs BC106-VIS - for observing diffracted beams at this location,

The image captured in Figure 3-4 shows the Thorlabs BC106-VIS, which comprises essential components: an optical sensor covering a range of 360-1000nm; a Mini B USB connector and a TTL Trigger input, four absorptive neutral density (ND) filters (10dB, 20dB, 30dB, and 40dB). The accompanying software offers comprehensive laser beam analysis features (see Figure 3-5). It enables the simultaneous display of 2D and 3D beam profiles with a good resolution. Crucial beam profile parameters like intensity profile, beam diameter,-and peak density can be precisely tracked. The detector area spans 8.8mm×6.6mm, with pixels spaced at 6.45µm×6.45µm.

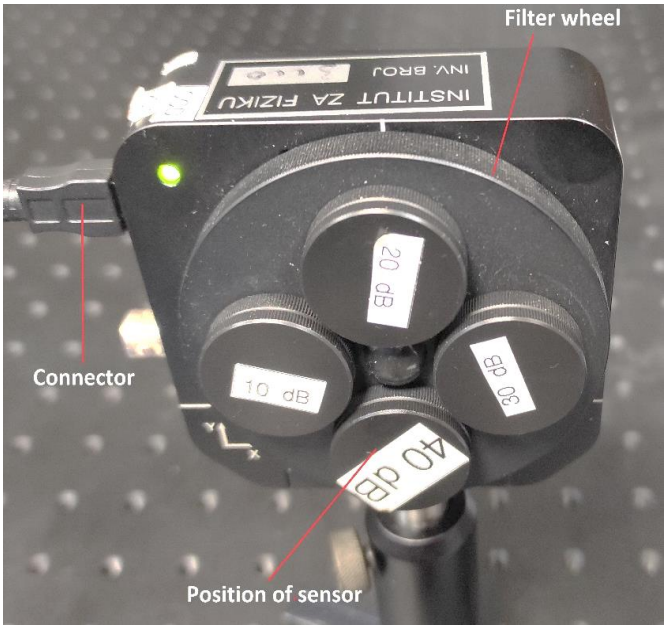

Figure 3-4: captured image of a Thorlabs BC106-VIS beam profiler used in this thesis.

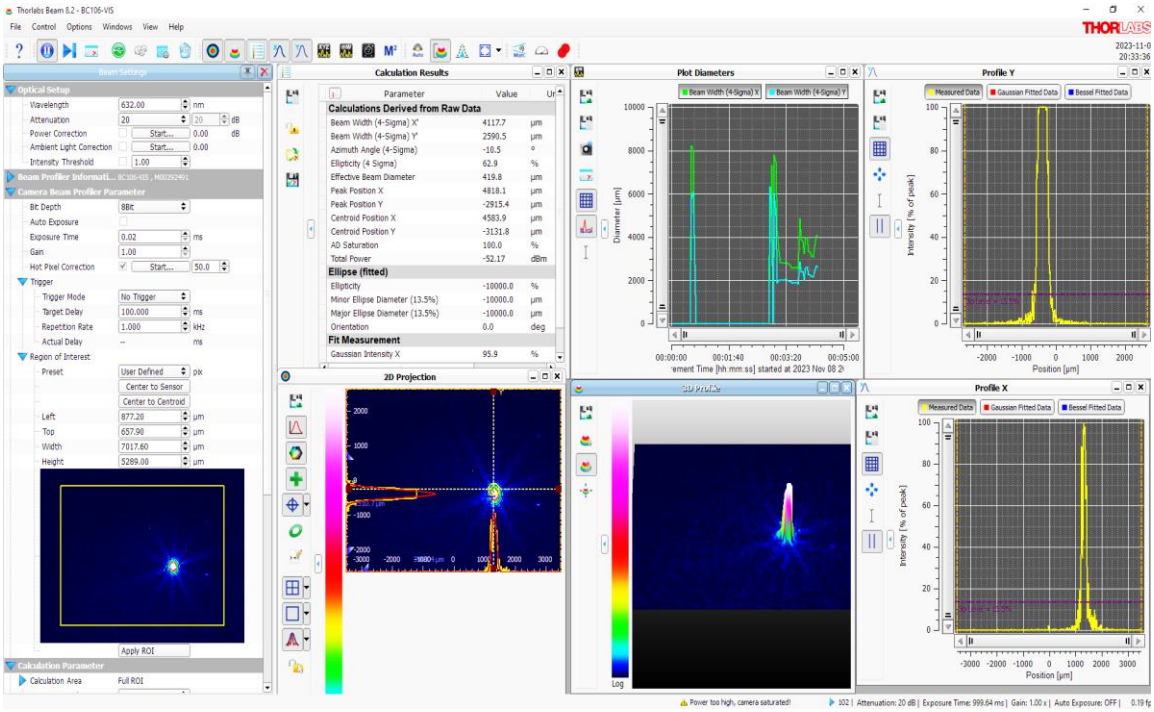

Figure 3-5: The Thorlabs BC106-VIS user interface.

3.4 4f system for beam shaping

To create customized beams, it's crucial to mitigate diffraction effects, maintaining sharp edges and preserving intricate details in the beam's phase, amplitude, and polarization. In our experimental setup, the 4f system is used to relay the optical fields between the object and image planes, thus minimizing diffraction effect and eliminating the quadratic wavefronts. The four focal lengths long setup is made by two lenses and a transparency plate. A conventional coherent 4-f imaging system is shown in Figure 3-6.

Assuming lens L1 and lens L2 have the same focal length f, we have an input of the form of a transparency $U_i(x',y')$ located in the object plane which is illuminated by a plane wave. Employing the Fresnel diffraction formula to calculate the field immediately in front of the lens L1 we have:

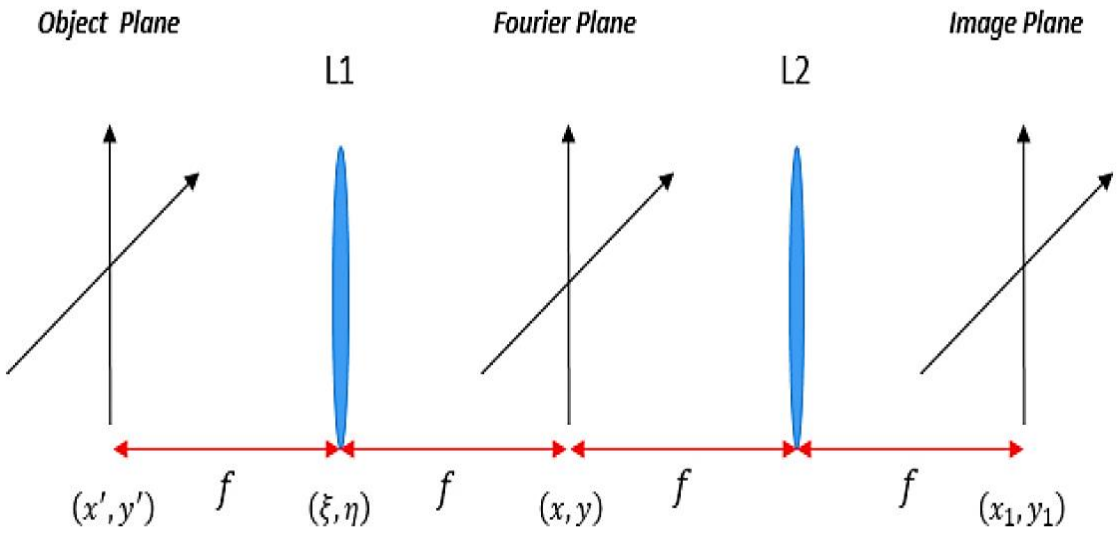

Figure 3-6: Schematic diagram of 4f imaging system.

$$
\begin{aligned}
U_1 &= U_i(x',y') * h(\xi,\eta;f) \\
&\propto \int_{-\infty}^{\infty}\int U_i(x',y') \exp\left(ik \frac{(\xi-x')^2+(\eta-y')^2}{2f} \right) dx'dy' \\
&= \exp\left(ik \frac{\xi^2+\eta^2}{2f} \right) \int_{-\infty}^{\infty}\int U_i(x',y') \exp\left(ik \frac{x'^2+y'^2}{2f} \right) \exp\left(-ik \frac{\xi x'+\eta y'}{2f} \right) dx'dy'
\end{aligned}
\tag{3-1}
$$

Where,

$$h(x,y;z)=\exp(ikz)\frac{-ik}{2\pi z}\exp\left[\frac{ik}{2z}\left(x^2+y^2\right)\right] \tag{3-2}$$

$h(x,y;z)$ is called the point spread function (PSF) in Fourier optics. The field distribution U_2 immediately after Lens1 can be calculated by multiplying the phase function as follows:

$$U_2(\xi,\eta)=U_1(\xi,\eta)\exp\left(-ik\frac{\xi^2+\eta^2}{2f}\right) \tag{3-3}$$

where $exp\ (-ik\frac{\xi^2+\eta^2}{2f})$ is the phase function of an ideal thin lens, which means the lens will only affect the phase of the incident fields. The field distribution U_3 in the back focal plane of the lens L1 (the Fourier plane) can be found as:

$$\begin{aligned}U_3(x,y)&\propto\int_{-\infty}^{\infty}U_2(\xi,\eta)\exp\left(jk\frac{(x-\xi)^2+(y-\eta)^2}{2f}\right)d\xi d\eta\\&=\exp\left(jk\frac{x^2+y^2}{2f}\right)\int_{-\infty}^{\infty}U_1(\xi,\eta)\exp\left(-jk\frac{\xi\eta+\eta y}{f}\right)d\xi d\eta\\&=\exp\left(jk\frac{x^2+y^2}{2f}\right)F\{U_1(\xi,\eta)\}\Big|_{k_\eta=ky/f}^{k_\xi=kx/f}\end{aligned} \tag{3-4}$$

And F is Fourier transform. Where,

$$\begin{aligned}&F\{U_1(\xi,\eta)\}=F\{U_i(x',y')*h(\xi,\eta;f)\}\\&=F\{U_i(x',y')\}H(x',y')=F\{U_i(x',y')\}\exp\left(-i\frac{f(k_{x'}^2+k_{y'}^2)}{2k}\right)\end{aligned} \tag{3-5}$$

If we let those spatial frequencies $k_{x'}$ and k_ξ , $k_{y'}$ and k_η equal, $U_3(x,y)$ can be simplified as:

$$\begin{aligned}&U_3(x,y)\propto\exp\left(ik\frac{x^2+y^2}{2f}\right)F\{U_i(x',y')\}\exp\left(-i\frac{f(k_{x'}^2+k_{y'}^2)}{2k}\right)\Bigg|_{k_{y'}=ky/f}^{k_{x'}=kx/f}\\&=F\{U_i(x',y')\}\Big|_{k_{y'}=ky/f}^{k_{x'}=kx/f}\end{aligned} \tag{3-6}$$

We can see the lens phase function cancels out the quadratic phase term introduced by the Fresnel diffraction and proportional to the Fourier transform of the incident transparency $U_i(x',y')$. According

to the Equation (3-6) the field in the image plane will be the Fourier transform of $U_3(x, y)$. Thus U_{out} at Image plane can be written as:

$$\begin{aligned} U_{out}(x_1, y_1) &\propto F\{U_3(x, y)\}\Big|_{k_y = k_{y1}/f}^{k_x = kx_1/f} \\ &= F\left\{F\{U_i(x', y')\}\Big|_{k_{y'} = k_{y1}/f}^{k_{x'} = kx_1/f}\right\}\Big|_{k_x = kx_1/f}^{k_x = kx_1/f} \\ &= \frac{f}{k} U_i(-x_1 - y_1) \end{aligned} \tag{3-7}$$

So far, we derived a plane wave from a laser to illuminate $U_i(x', y')$ in the 4-f optical processing system. This demonstrates the direct re-imaging of the initial input from the object plane onto the image plane without introducing any quadratic phase alterations through Fresnel diffraction. Essentially, the object can be perfectly represented at the image plane in terms of both amplitude and phase.

3.4.1 Experimental implementation for OAM beam generation

The experimental setup to demonstrate the vortex beam generation is shown in Figure 3-7. A frequency stabilized He-Ne laser at λ=632.8 nm (≈15mW) is used as our light source to provide the fundamental Gaussian beam. The laser beam is passed through a neutral density filter (NDF) to decrease the intensity of the beam so that it does not saturate the CCD camera. The spatial filter system (SF) before the SLM cleans the beam transverse intensity and creates a uniform Gaussian beam. By loading the respective CGH on SLM the corresponding beams were generated in the first diffraction order. A half-waveplate (*HWP*) was used before SLM in order to rotate the polarization of the incident light beam to the optimum angle for the SLM so as to maximize the power diffracted into the first-order.

Subsequently, a simple 4-f system is used to rescale the beam size and select the desired diffraction order, a pinhole in the Fourier plane of the SLM was used to select the first diffraction order and block all other remaining parts. Finally, the generated vortex beam was captured using a CCD camera and a beam profiler.

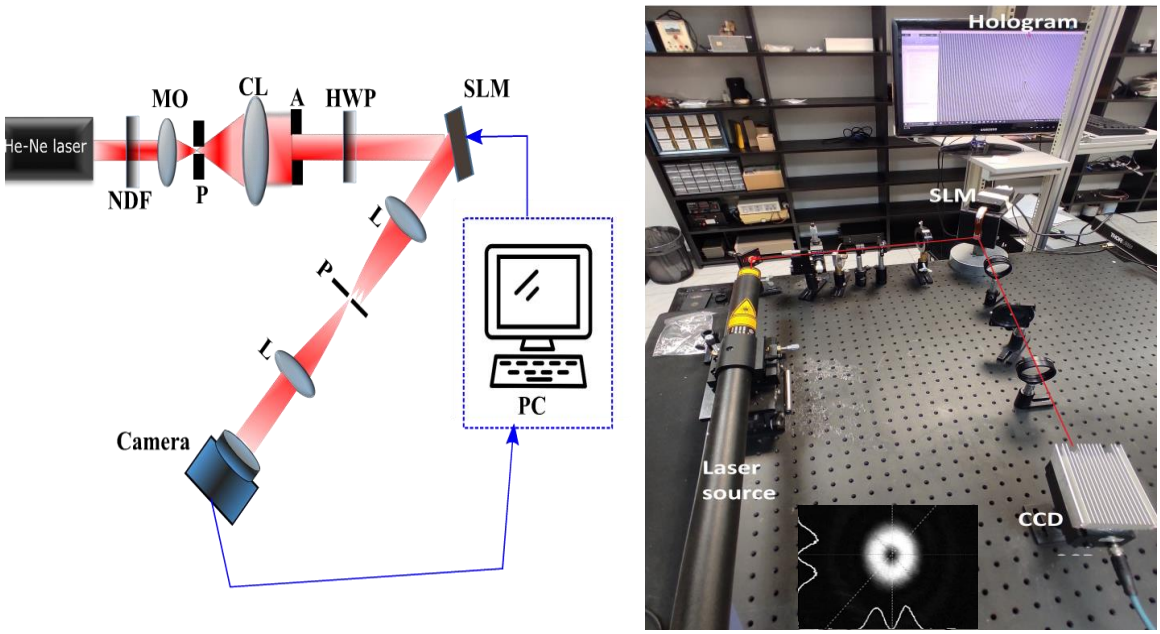

Figure 3-7: (Left)Schematic of experimental setup. NDF: neutral density filter, MO: Microscope objective, P: Pinhole, CL: Collimated lens, A: Aperture, L: Lens, SLM: Spatial light modulator, HWP: half wave plate. (Right) The experimental setup and the beam profile of the resulting LG beam with l = 2.

Understanding the response of the SLM to varied phase modulations precedes its utilization. Our study gives considerable focus to assessing diffraction efficiency when employing different CGHs. We specifically investigate three distinct CGH types: pure amplitude binary fork grating, pure phase sinusoidal fork-shaped structure, and pure phase blazed fork grating.

Assessing the efficiency of these CGHs after being loaded onto the SLM is pivotal. Diffraction efficiency serves as a critical metric, quantifying the proportion of incident light diffracted into specific orders or modes. A hologram's efficiency is often quantified by its absolute diffraction efficiency, which represents the ratio of the power within a specific order, denoted as P_i, to the incident light power, P_0, expressed as $Ef = Pi/P0$. This investigation into the characteristics and performance of each modulation method is essential for our research. It allows for optimal detection of light's OAM with high efficiency, an imperative aspect for optimizing the performance of optical systems.

3.4.2 Binary amplitude fork diffraction grating

The Transmission function of a pure amplitude binary fork-shaped grating in polar coordinate can be expressed as follows:

$$T(r,\varphi)=\frac{1}{2}\left[1+\mathrm{sgn}\left(\cos\left(\frac{2\pi}{\Lambda}r\cos\varphi-\ell\varphi\right)\right)\right] \quad (3\text{-}8)$$

The parameters of the binary fork-shaped grating are defined by the spatial period, denoted as 'Λ,' which characterizes the grating period in horizontal direction, and the topological charge, 'l,' an integer value representing the grating's singularity strength. "sgn" indicates sign function which returns 1 if the number is positive, zero (0) if the number is 0, and -1 if the number is negative. As depicted in Figure 3-8, CGHs were created, in Matlab with a fixed spatial period, Λ = 0.22 mm, while varying the values of 'l.'

The experimental results indicate that when a Gaussian beam with beam radius of $w_0 = 3mm$ is incident on SLM loaded with a pure amplitude binary fork-shaped grating, three distinct diffraction orders, namely (−1, 0, and +1), are generated. These diffraction orders correspond to the far-field diffraction pattern produced by the grating. In our experimental setup, we employed a laser power meter (COHERENT LaserMate/Q), to precisely measure the power density. This measurement was a crucial component of our investigation into the generated diffracted orders. The laser power meter allowed us to quantify and analyze the distribution of optical power, particularly within the context of the various diffracted orders produced by the binary fork-shaped grating. Prior to reaching the SLM, the incident laser power was 40 mW/cm². Upon interacting with the SLM, the power measurements for the diffracted orders exhibited reduced power. For the +1 diffraction order, the power density was 8 mW/cm², while the -1 diffraction order displayed a slightly higher power density of 9 mW/cm². The ratio between the intensities of the desired diffraction order and the incident illuminating beam has been approximately 22.5% for this particular type of grating.

3.4.3 Sinusoidal fork diffraction grating

Transmission function of a pure amplitude sinusoidal fork-shaped grating in polar coordinate can be expressed as follows:

$$T(r,\varphi)=\frac{1}{2}\left[1+\cos\left(\frac{2\pi}{\Lambda}r\cos\varphi-\ell\varphi\right)\right] \quad (3\text{-}9)$$

Where Λ is grating period in horizontal direction and l is an integer. As depicted in Figure 3-9, fork holograms were generated, using simulation with a fixed spatial period, Λ = 0.22 mm, while varying the values of 'l.'

The results show that when a Gaussian beam ($w_0 = 3mm$) is incident upon SLM loaded with a pure amplitude sinusoidal fork-shaped grating, compared to binary modulation there are also higher diffraction orders, namely (-2,−1, 0, and +1,+2), which are produced. These diffraction orders correspond to the far-field diffraction pattern produced by the grating. For the +1 diffraction order, the power density was recorded at 5 mW/cm² and for -1 diffraction order it was measured around 6 mW/cm². The efficiency dropped by about 8%, reaching 14.5%, because of this specific phase modulation.

3.4.4 Blazed fork diffraction grating

Transmission function of a pure phase blazed fork grating can be expressed in polar coordinate as follows:

$$T\left(r,\varphi\right)=\exp\left[i\,\frac{\delta}{2\pi}\,\mathrm{mod}(\ell\varphi-\frac{2\pi}{\Lambda}r\cos\varphi,2\pi)\right] \qquad (3\text{-}10)$$

Where δ is the amplitude of the phase depth modulation and Λ is the period of grating and l is an integer. And $mod(a,b)$, is the reminder of a/b. As depicted in Figure 3-10, holograms were produced, using simulation with a fixed spatial period, Λ = 0.22 mm, while varying the values of l. The experimental results, as indicated by measurements using a beam profiler, reveal a notable predominance of diffracted light towards the +1 diffraction order. Conversely, a significantly smaller portion of the incident beam is directed toward the -1 diffraction order. The power density for the +1 diffraction order was measured to be 25 mW/cm², indicating a significant intensity associated with this particular order. In contrast, the -1 diffraction order displayed a relatively lower power density, measuring approximately 2 mW/cm². The calculated efficiency for this specific grating type was approximately 62.5% for the first diffraction order.

Our research, conducted with various hologram loaded on SLM, reveals that using a pure phase blazed grating is the most advantageous option for the energy efficient shaping of light beams. In contrast, alternative choices, such as pure amplitude binary fork-shaped grating and sinusoidal gratings, are discerned as suboptimal selections. The increase in diffraction efficiency isn't just a technical improvement, it promises to significantly elevate the overall efficiency of optical system. This, in turn, holds the potential to transform our ability to detect the OAM of vortex beams for higher topological charge.

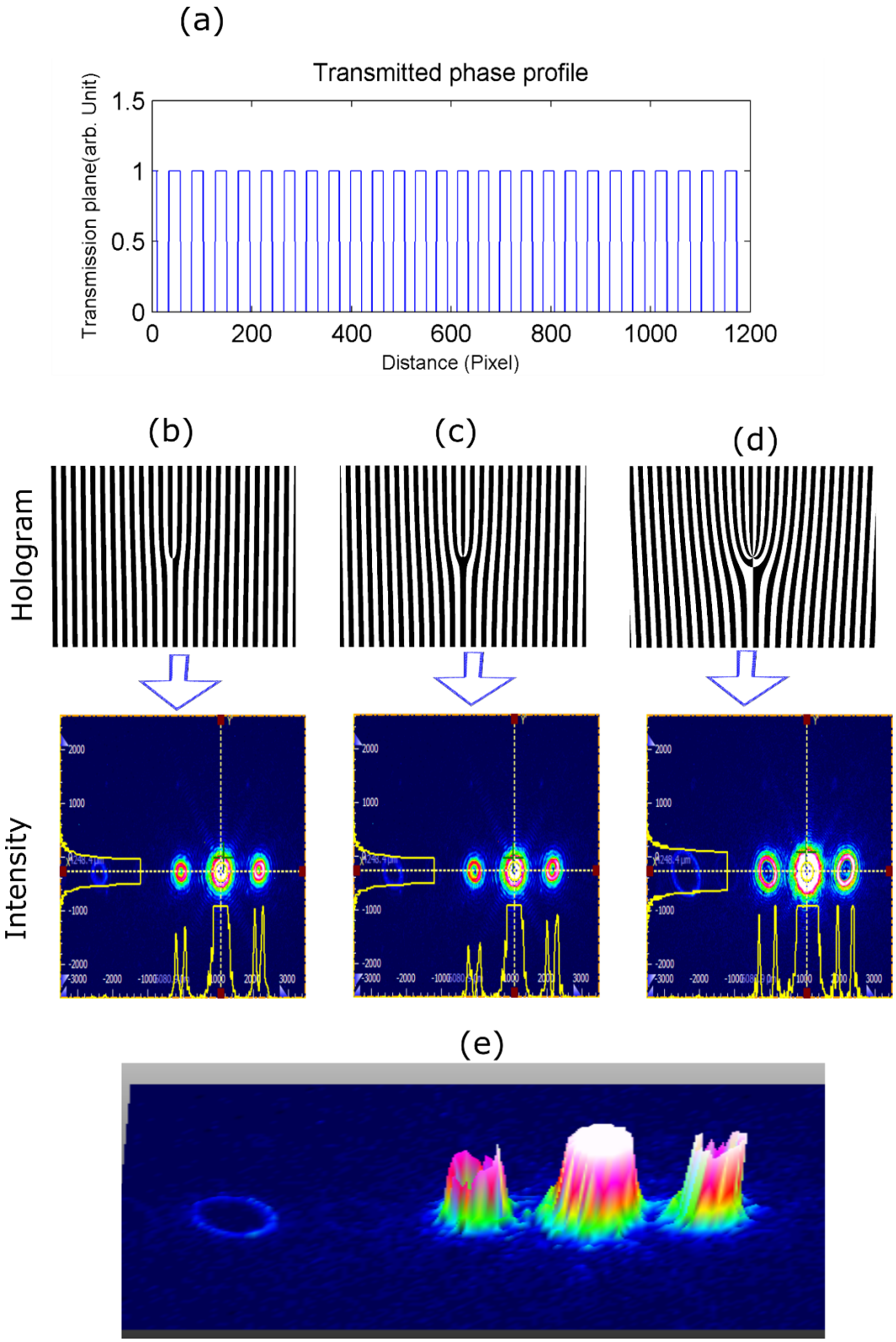

Figure 3-8: Transmitted phase profile of pure amplitude binary fork grating(**a**). Binary fork gratings and their corresponding far-field diffraction patterns when Gaussian beams are incident on (b) with l = 1; (c) with l = 2; and (c) with l = 5; and (e) 3D Beam profile for l=5

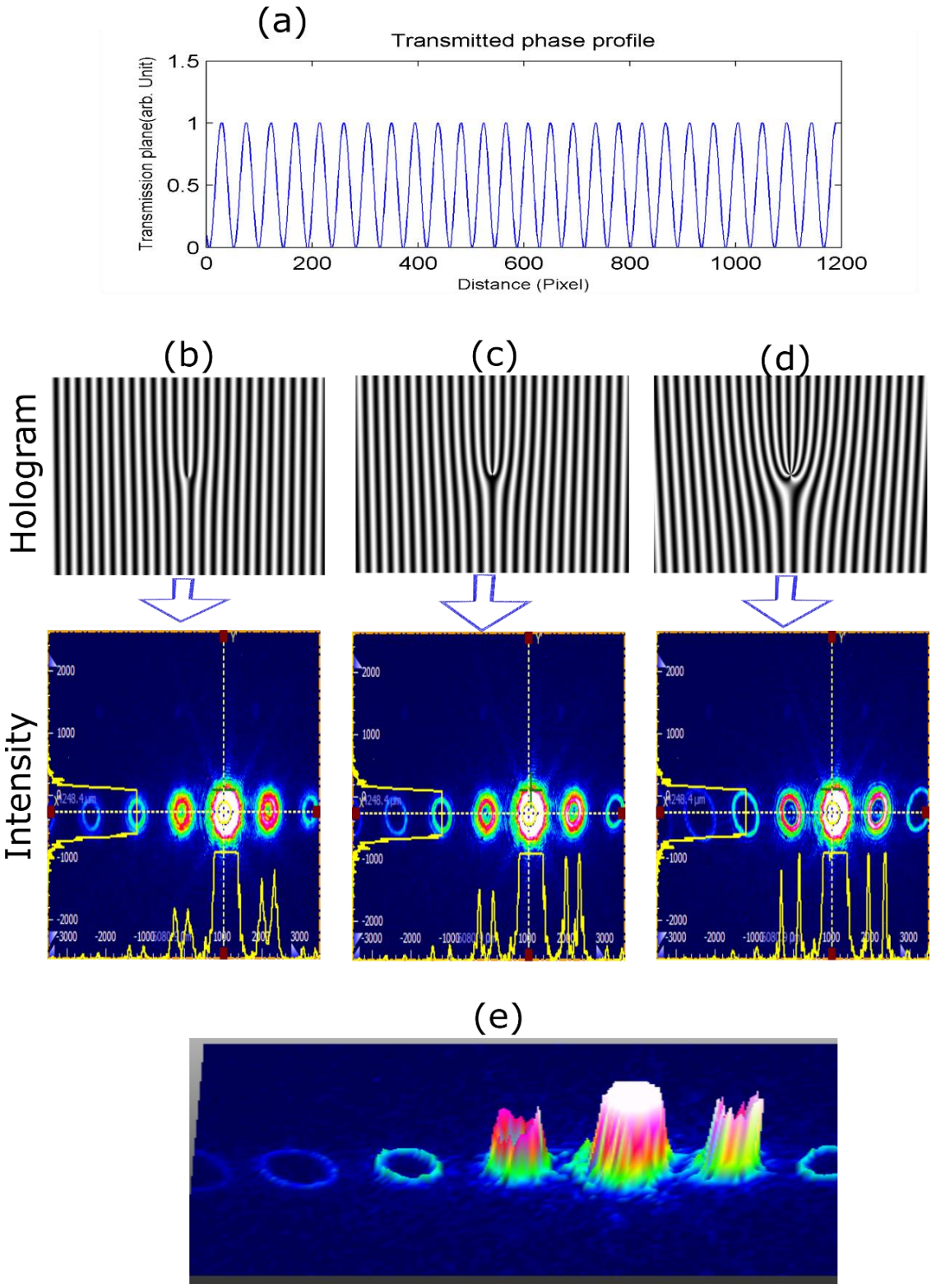

Figure 3-9: Transmitted phase profile of sinusoidal phase fork grating(**a**). sinusoidal fork gratings and their corresponding far-field diffraction patterns when Gaussian beams are incident on (b) with l = 1; (c) with l = 2; and (c) with l = 5; and (e) 3D Beam profile for l=5

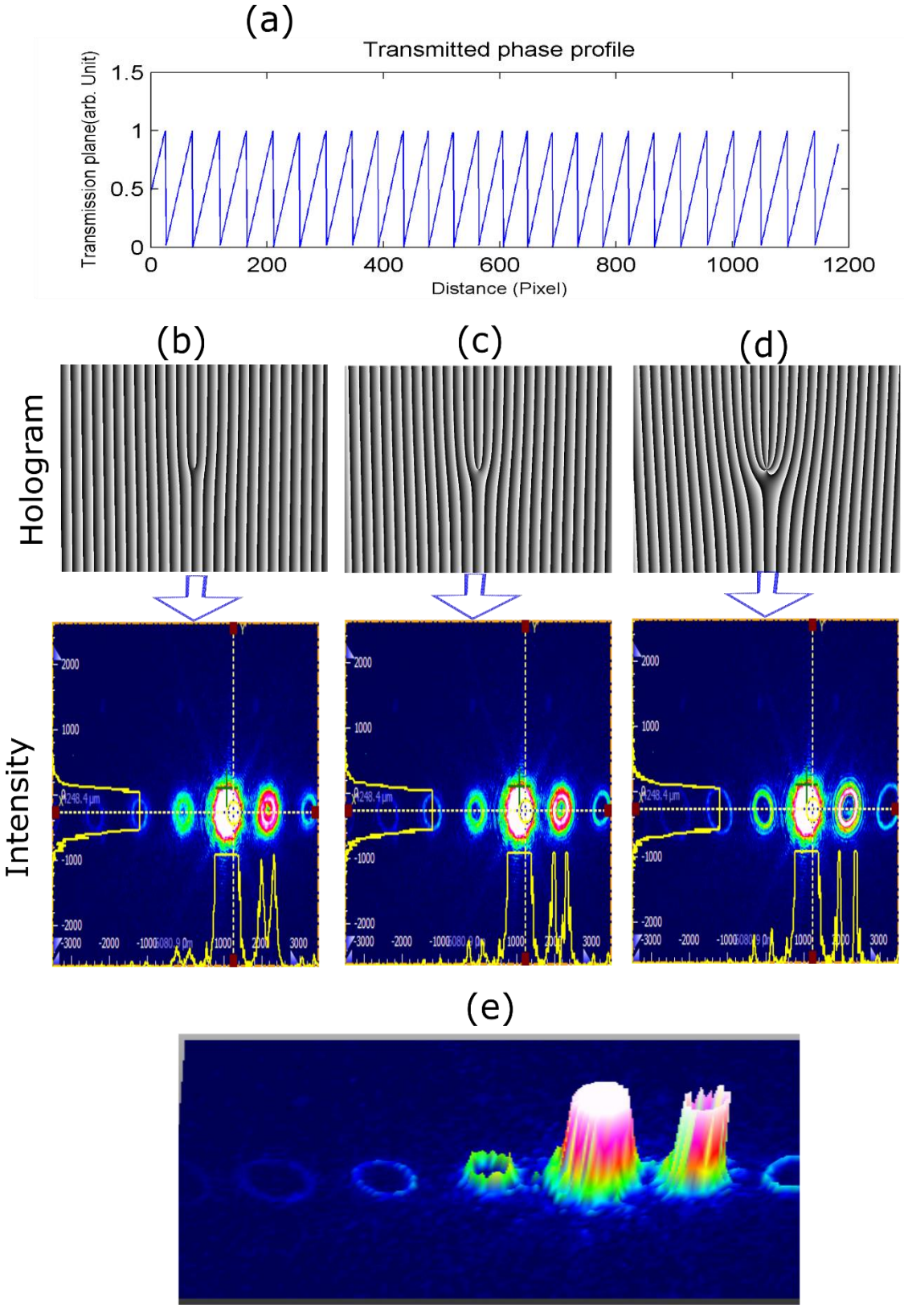

Figure 3-10: Transmitted phase profile of blazed phase fork grating(**a**). blazed fork gratings and their corresponding far-field diffraction patterns when Gaussian beams are incident on (b) with l = 1; (c) with l = 2; and (c) with l = 5; and (e) 3D Beam profile for l=5

3.5 Addressing technical issues in SLM implementation

In the practical implementation of SLMs, we encountered several technical challenges that show deviation from the ideal conditions necessary for a perfect modulation of the light field. It is imperative to briefly address these issues to provide an understanding of the limitations and considerations encountered in our experimental setup. The primary concerns were diffraction efficiency, beam misalignment, and the degradation of shaped light due to the absence of proper spatial filtering of the laser beam. Understanding these technical challenges is important for proper light shaping and maximizing its effectiveness in various applications.

3.5.1 Low diffraction efficiency

SLMs are used in reconstructing the complex amplitude of a wavefield optically. However, the far-field reconstructed wavefield is affected by non-ideal modulation properties and the discrete nature inherent in SLMs which results in decreased diffraction efficiency. These effects are drawbacks as they interfere with the visual quality and diminish the light efficiency within the region of interest. Further, minor deviations in the manufacturing process of LC-SLMs microdisplays could potentially lead to unexpected issues. For instance, even a subtle curvature in the microdisplay might induce aberrations in the shaping of light. These issues can be explored optically and programmatically.

Optically, low diffraction efficiency poses two significant problems. Firstly, it leads to a reduction in light intensity. Secondly, and even more problematic, it can cause interference, as the non-diffracted residual light may overlap with the modulated part of the light. We explored the application of a 4f system to address this issue.

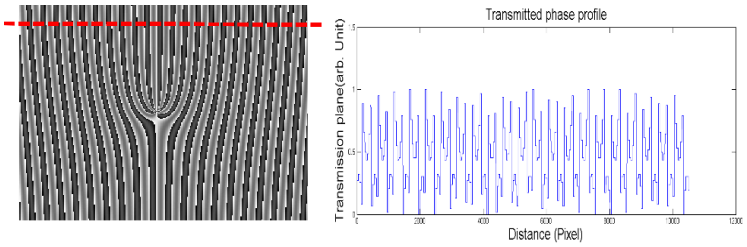

Figure 3-11: A fork hologram profile, with low phase depth modulation $\delta = 0.6$ is shown on the left, with showcases the profile of the grating along a horizontal red line.

In programming terms, the amplitude of modulation depth δ of encoded phase can significantly impact diffraction efficiency. The optimal value finds to be between $0.1 < \delta < 0.4$ for our application. Specifically, the desired phase distribution may be influenced by the intended intensity distribution, presenting challenges in precisely achieving the preferred phase information. Therefore, the modulation depth must be meticulously chosen for optimal performance through simulation. Figure 3-12 demonstrates the impact of a $\delta = 0.6$ phase modulation depth. The results indicate a reduced efficiency in profile depth when compared to the optimal outcomes. (see Figure 3-10 (e)). This highlights the critical role of parameter selection in simulations, emphasizing the importance of optimal values to minimize undesired diffraction effects and enhance overall efficiency in light shaping in the first diffraction order.

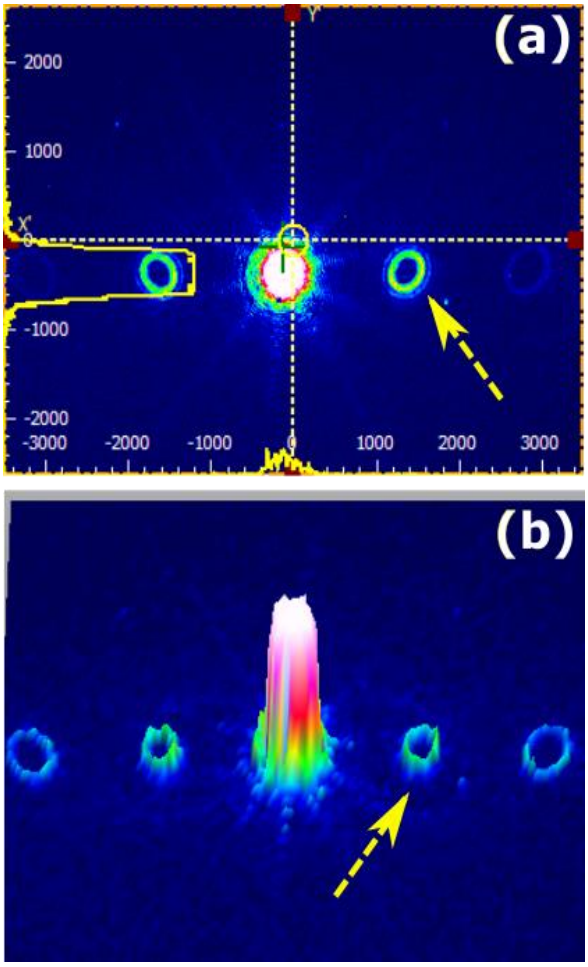

Figure 3-12: SLM's performance with a fork grating with $l = 5$ with phase depth modulation of ($\delta = 0.6$) (a) 2D view depicts the consequences when phase modulation is not chosen reasonably. This deficiency results in diminished energy efficiency in the first diffracted orders and a subsequent reduction in the 3D profile depth (b).

3.5.2 Exploring the influence of beam misalignment on shaping light

Here, our aim is to investigate the interplay between the combined impact of misaligned input beam on the effectiveness and precision of light shaping. Gaining insights into how these factors interact is crucial for optimizing optical systems and applications reliant on the precise manipulation of light patterns. Figure 3-13 illustrates the far-field diffraction pattern depicting the effects of off-axis illumination.

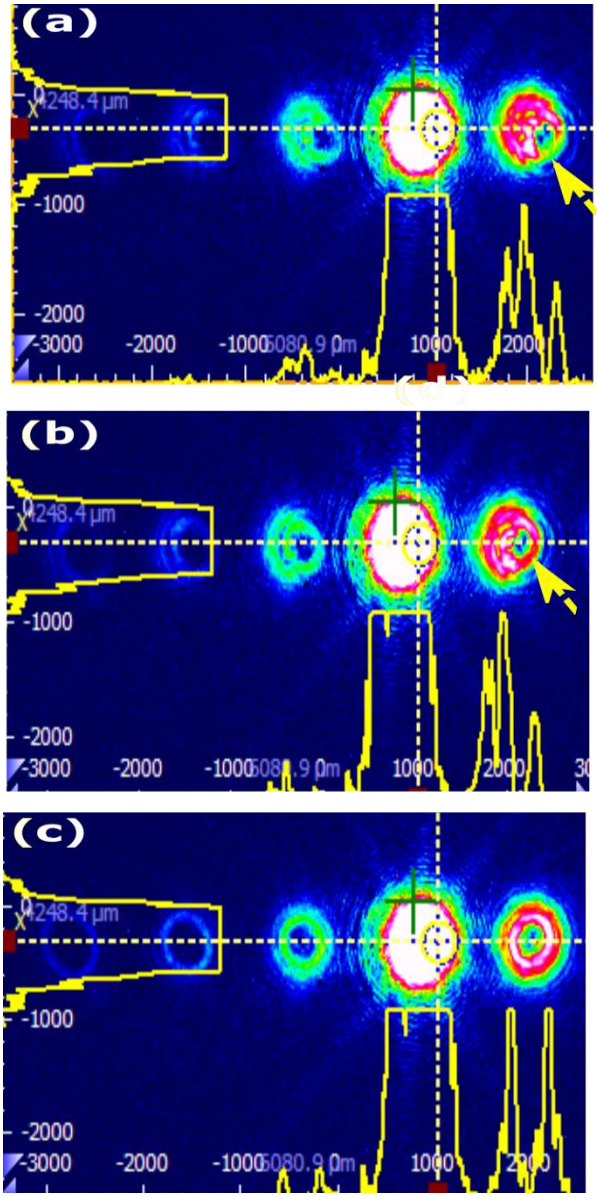

Figure 3-13: Examining the Impact of incident beam which is misaligned on a fork hologram with $l = 5$ (a) the illumination beam is shifted 3mm from the center, (b) shifted by 2mm, and (c) central illumination produces shaped light with perfect doughnut shape.

3.5.3 Effect of spatial filtering on shaping light

Another factor that can affect and distort shaped light, is the impact of input beam quality, which can define the quality of the shaped light. Understanding the dependencies of the diffracted beam shaped structure on incident beam quality is crucial for establishing accuracy in different optical application. Using beam profiler we grabbed photos of generated vortex beam with $l = 5$ from a the He-Ne laser source which is not spatially filterd (Figure 3-14(a)). Employing a spatial filtering system, we used a 10x microscope objective with a 25μm pinhole. The resulting beam is shown in Figure 3-14 (b).

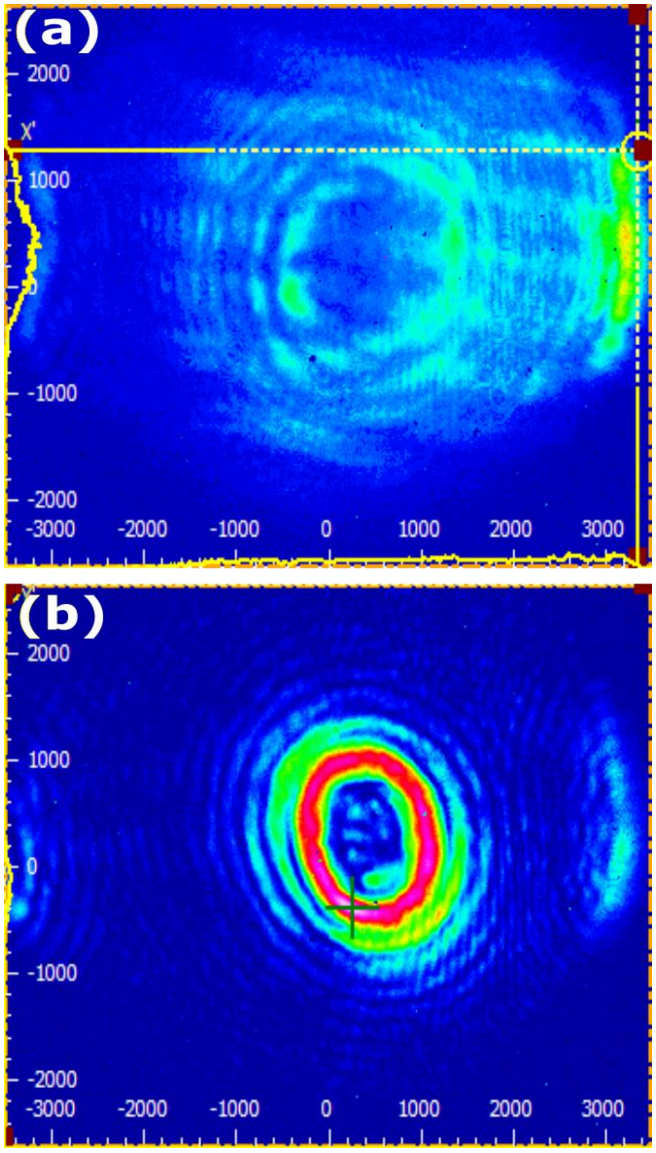

Figure 3-14: effect of spatial filtering on shaping light. (a) without filtering (b) using spatial filtering.

Finally, we would like to provide a set of recommendations for effectively utilizing SLMs and troubleshooting potential issues to ensure optimal performance.

Diagnostic Imaging of Fourier Plane: Verify the system's proper functionality by imaging the Fourier plane of the SLM. This diagnostic approach provides valuable insights into the system's performance.

Functional Check with diffraction Grating: Confirm the operational status of the SLM by applying a linear grating, inducing a deliberate shift in the spot along both the x and y axes. This procedure serves as a practical check for the dynamic responsiveness of the SLM.

Flatness Implementation Check: Evaluate the implementation of panel flatness. When imaging the focal intensity distribution, the presence of a well-defined Airy disc is indicative of proper flatness. Distorted focal intensity suggests potential issues with flatness compensation on the SLM, and addressing this may involve additional phase modulation for distortion compensation.

Polarization Assessment: Verify incident polarization on the SLM by introducing a half-waveplate before it. Direct light into the first diffraction order using a phase grating using SLM and monitor the intensity in the diffracted order while varying the waveplate rotation angle.

Phase Pattern Inspection: To inspect the presentation and behavior of phase patterns in the optical system, substitute the SLM with a secondary monitor. This direct observation allows for a comprehensive assessment of how phase patterns are being displayed.

Implementing these recommendations ensures a thorough and systematic check of key aspects of SLM performance, facilitating optimal usage in various optical application.

4 Detection of OAM of light using sinusoidally-shaped phase gratings(SSPG)

In chapter 2, we explored the limitations of different existing methods characterized by their complexity and intricate experimental setups. Further detecting higher-order OAM or radial mode index remained an enduringly open challenge. Our research centers around simplification, robustness and adaptability. The method discussed in this chapter is based on diffraction of LG beam (with zero radial mode index) from an originally designed sinusoidally shaped phase grating (SSPG). We demonstrate that the resultant far-field diffraction pattern depends on both the magnitude and sign of the azimuthal index, l. Notably, we show that this behavior is specifically linked to the azimuthal index, l. We explore three scenarios for LG mode detection: first, when the azimuthal mode index, l, assumes integer values; second, when it takes fractional (non-integer) values; and third, employing multiplexing for simultaneous detection of multiple vortex beams with different l value. The results underscore the expanded versatility of SSPG in detecting the OAM of optical vortices. The part of these results is published in [59].

4.1 Theory and basic equations

This section provides the theoretical framework essential for interpreting subsequent experimental findings. The model explores the diffraction patterns produced by an incident optical vortex with a specific wavelength λ and an azimuthal index l. This OV is positioned on a sinusoidally-shaped phase grating located at z = 0, where "z" represents the propagation axis. In this study, we use Fresnel diffraction integral to calculate the optical field at each plane of propagation. The optical field was initially propagated to the grating plane, where the incident field distribution was multiplied by the relevant transmission function. This resulting field distribution was then propagated. To describe the transverse coordinates on the aperture plane, we used Cartesian coordinate denoted as (x, y).

In Cartesian coordinates, the complex amplitude of an LG beam with the radial index p=0 over the x_0–y_0 plane can be written as[60]:

$$U\left(x_0,y_0\right)=A.(x_0+i.\mathrm{sgn}\left(\ell\right)y_0)^{|\ell|}\exp\left(-\frac{x_0^2+y_0^2}{w_0^2}\right) \quad (4\text{-}1)$$

where A measures the field strength, and we hereafter set A = 1. w_0 is the beam radius at z=0, and l indicate the topological charge.

The transmission function of a sinusoidally-shaped phase grating (SSPG) can be expressed as follows:

$$\tau(x_0,y_0)=\frac{1}{2\pi}Arg\left[\exp\left(i\frac{2\pi x_0}{\Lambda_x}-ia\sin(\frac{2\pi y_0}{\Lambda_y})\right)+\pi\right] \quad (4\text{-}2)$$

Where Λ_x, Λ_y are the pitch of the grating in x and y direction respectively, Arg returns the argument of the exponential between -π and π, and a is the amplitude of sinusoidal modulation and parameter for fine tuning. The designed SSPG is shown in Figure 4-1.

The vortex beam pass through the SSPG with a transmission function $\tau(x_0, y_0)$. The light beam complex amplitude field immediately after passing through the SSPG is:

$$U_t(x_0,y_0)=U(x_0,y_0)\tau(x_0,y_0) \quad (4\text{-}3)$$

Accounting for the complex phase modulation introduced by SSPG, the field distribution at the observation plane of x_1-y_1 at each plane of propagation, can be calculated using the Fresnel diffraction integral:

$$U(x_1,y_1;z)=h\int_{-\infty}^{+\infty}\int_{-\infty}^{+\infty}U_t(x_0,y_0)\exp\left[i\alpha\left(x_0^2+y_0^2-2\left(x_0x_1+y_0y_1\right)\right)\right]dx_0dy_0 \quad (4\text{-}4)$$

Where $h=\frac{1}{i\lambda z}exp[ikz+i\alpha(x_1^2+y_1^2)]$ and $\alpha=\frac{\pi}{z\lambda}$.

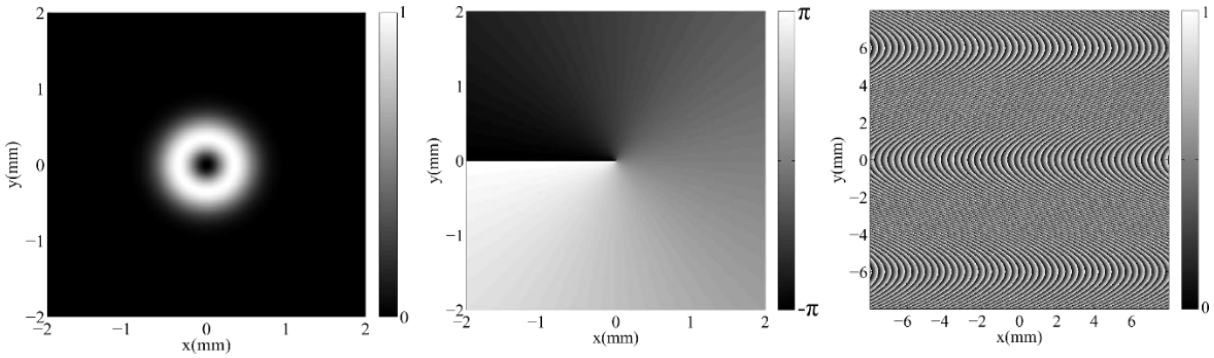

Figure 4-1: From the left to the right: the simulated results for intensity; and phase profiles of a vortex beam ($l = 1$, and beam waist of 0.5mm); and the transmission profile for blazed SSPG with Λ_x= 0.16mm, Λ_y= 12mm.

Figure 4-2 shows the geometry of simulated far-field intensity distributions after the beam's passing through the SSPG center. The vortex beams with topological charges $l = -10$ and $l = +10$ with beam waist of 0.5mm and $\lambda = 632nm$, passing through SSPG.

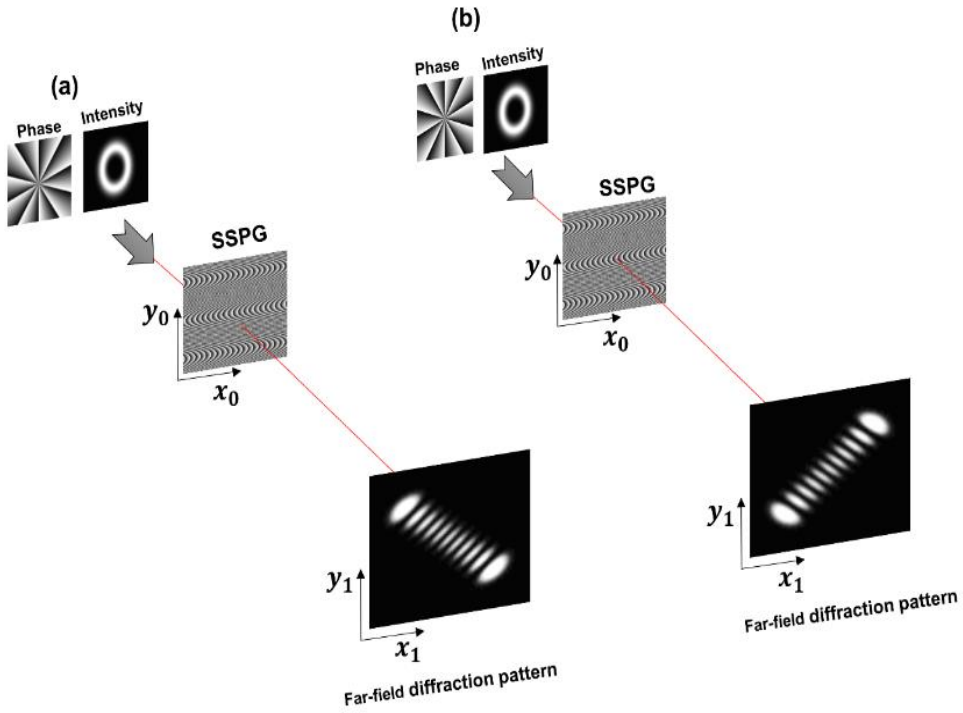

Figure 4-2: Simulation results for the far-field intensity distribution after vortex with the beam waist 0.5 mm, passing through SSPG for (a) l= -10 and (b) l=10. The other parameters were set as Λ_x= 0.16mm, Λ_y= 12mm, and a = 12, z = 2m which provide us with the most discernible fringes.

4.2 Far-field intensity profile

4.2.1 Far-field diffraction intensity distribution for integer azimuthal indices

In Figure 4-3, the numerically calculated results of the far-field diffraction intensity profiles are presented for integer azimuthal mode indices, l = -6,-12,-15 in the upper row, and l = +20, +30, +50 in the lower row.

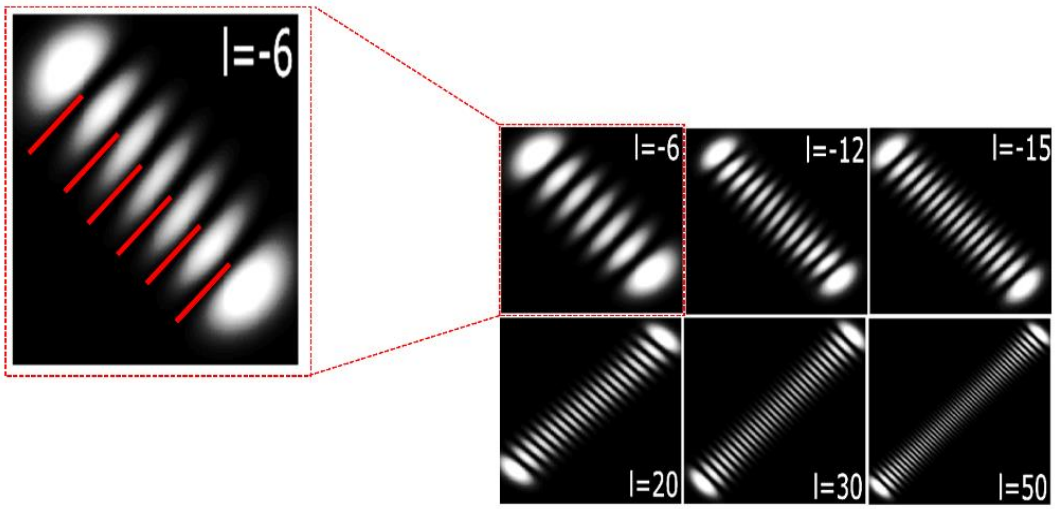

Figure 4-3: Numerical simulations depict the far-field diffraction intensity profiles showcasing various integer azimuthal mode indices: -6, -12, -15 in the upper row, and +20, +30, +50 in the lower row (from left to right). These patterns illustrate the behavior of far-field diffraction intensity under different azimuthal mode indices, indicating a rotational change when the sign of the azimuthal index, l, is reversed.

From the results of numerical simulations one can verify that the diffraction for the far-field intensity pattern is equal to the modulus of the azimuthal mode index. As can be seen from Figure 4-3, after diffraction from SSPG, a vortex beam with topological charge $\pm l$ breaks into $|l|+1$ bright fringes (or $|l|$ dark spots). Additionally, the fringe orientation gives the information about the sign of the incident vortex beam. Therefore, according to the theoretical calculation, detecting both positive and negative signs using SSPG appears feasible. The effect of changing the sign of the azimuthal index, $l \rightarrow -l$ is illustrated in Figure 4-3, it becomes apparent that for negative topological charges, the intensity distribution exhibits an anti-diagonal orientation, whereas for positive topological charges, the intensity distribution takes on a diagonal configuration. Thus, the number of fringes in the far-field diffraction pattern from SSPG and its orientation can be used as a detector of the azimuthal mode index, l, of an incident OV. As it can be seen from Figure 4-2, the intensity profile of a vortex beam with l azimuthal

index is identical to the $-l$ case (a ring shape), this makes it impossible to deduce the azimuthal mode index directly from the intensity profile of the vortex beam. The SSPG plays a crucial role in disrupting this symmetry, thereby enabling the differentiation between the two distinct signs of the OAM value. The ability to discern between positive and negative l values carries profound significance, particularly within the domain of communication. Furthermore, it plays a important role in the exploration and analysis of vortex beam interaction with chiral structures, opening promising avenues for advancements and insights in these fields.

4.2.2 Far-field diffraction pattern of fractional azimuthal indices

We have also investigated the fractional charges in response to the considerable interest surrounding the presence of fractional azimuthal indices within optical beams. This fascination primarily centers on probing entanglement and furthering research in quantum information [61]. For non-integer azimuthal indices (fractional l values), a phase singularity appears, creating a line of low intensity. Researchers have employed both SPP and CGH to produce optical beams with half-integer fractional azimuthal indices. Basistiy et al. [62] utilized a CGH employing a half-integer screw dislocation for generating a fractional LG beam. In 2004, Berry mathematically explored the development of waves carrying phase singularities of $2\pi l$, where l could be either an integer or a fractional value [63]. When the fractional phase step ($2\pi l$) deviates from an integer value, Berry's theoretical prediction outlines creation of new vortex, particularly as this step approaches and surpasses a half-integer value. His insights into the transformative nature of the fractional phase step greatly enhance our comprehension of singular optics phenomena.

The far-field diffraction intensity patterns resulting from a vortex beam with a fractional azimuthal mode index diffracting from SSPG are shown in Figure 4-4. These patterns illustrate the transition from $l = 2$ to 3, incrementing in fractional steps of 0.1. Notably, for azimuthal indices between 2 and 2.2, the far-field pattern closely resembles that of $l = 2$, exhibiting $|l| = 2$ dark fringes. However, for values of $l \geq 2.4$, a distortion in the far-field diffraction intensity pattern becomes evident, particularly highlighted in the red-circled region for $l = 2.3$ in Figure 4-4 below.

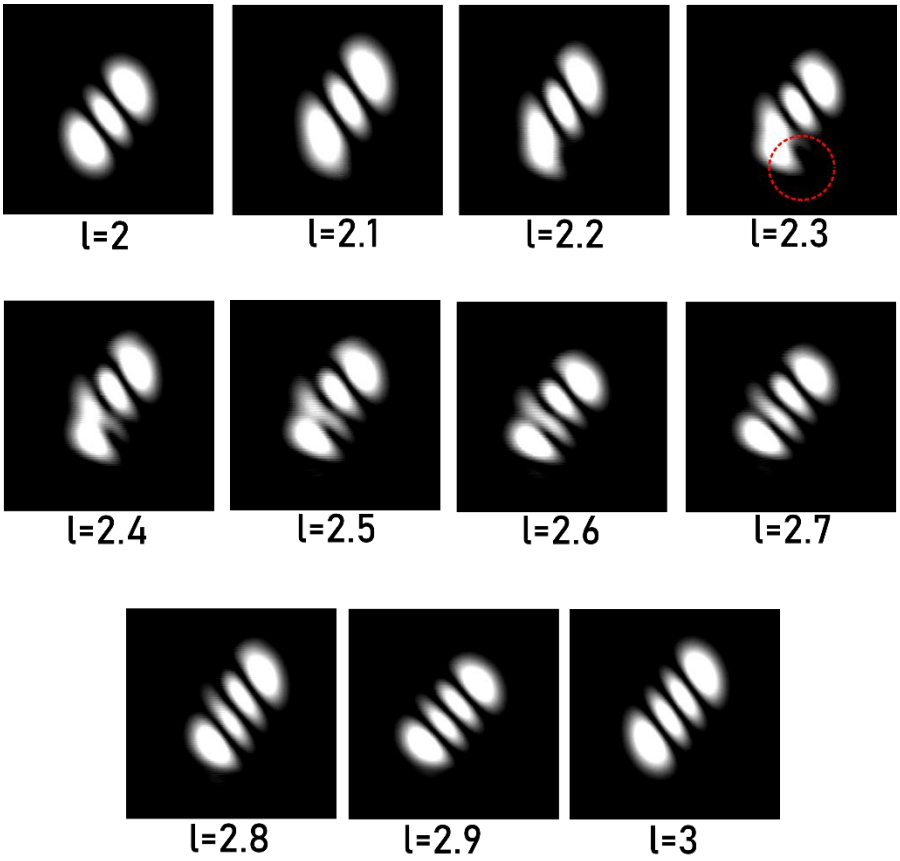

Figure 4-4: Numerical simulations depict the far-field diffraction intensity pattern for fractional azimuthal mode indices. The sequence shows the far-field diffraction intensity patterns ranging from l = 2 to 3, incrementing in fractional steps of 0.1. Notably, these patterns reveal the emergence of a new fringe as the azimuthal mode index reaches and surpasses a half-integer value.

The distortion observed for $l \geq 2.4$ marks the emergence of a new fringe. As l reaches 3, this new fringe fully forms, evident by the presence of $|l| = 3$ dark fringes in the far-field diffraction intensity pattern. These intensity profiles depict the evolution from two to three fringes as the azimuthal mode index progresses from $l = 2\ to\ 3$. Specifically, the pattern maintains its $l = 2$ form with two fringes between $2 < l < 2.3$, while for $l = 3$, the presence of three dark fringes becomes prominent for $l \geq 2.5$ until reaching completion at $l = 3$. This sequence aligns precisely with Berry's prediction [63] that the creation of new vortex occurs at the point where the fractional azimuthal mode index passes a half-integer value. The simulation results demonstrate that SSPG possesses the capability to detect fractional topological charges, rendering it more applicable for specific applications where the detection of fractional charges is a requisite.

4.2.3 Simultaneous detection of multiple vortex beams

Here, our objective is to explore the possibility of detecting multiple vortex beams with distinct topological charges employing SSPG. We briefly discuss the method for generating multiple OAM beams employing two perpendicular fork gratings. The process involves creating a phase mask for multiple vortex beams, illustrated in Figure 4-5 (b). By utilizing fork gratings, each with a central l-fold fork, positioned in the horizontal and vertical direction, we combine these two gratings to produce their combination, a two-dimensional (2D) fork diffraction grating. In our example, 2D grating resulted from a horizontal fork with strength 1-fold fork dislocation and a vertical fork hologram with 3-fold fork dislocation. This method facilitates the transformation of a Gaussian light beam into nine distinct diffraction orders. Each of these diffraction orders constitutes a vortex beam carrying a unique topological charge. Figure 4-5 displays the array of diffraction orders generated by the designed 2D grating. Notably, Figure 4-5 (c) shows the variation in topological charge and the mode indices (n_x, n_y) for each diffraction order. The resulting combination creates $(n_x = -1, n_y = +1)$ diffraction order which is a superposition of diffracted orders $(n_x = -1, n_y = 0)$ and $(n_x = 0, n_y = +1)$ and carries topological charge of $l = (+3) + (-1) = +2$, as shown in Figure 4-5 (c). The topological charge for additional diffraction orders can be computed in a similar manner. For this specific example (Figure 4-5 (c)), the topological charge corresponding to each diffraction order in the can be determined using the expression $l(n_x, n_y) = n_x + 3n_y$.

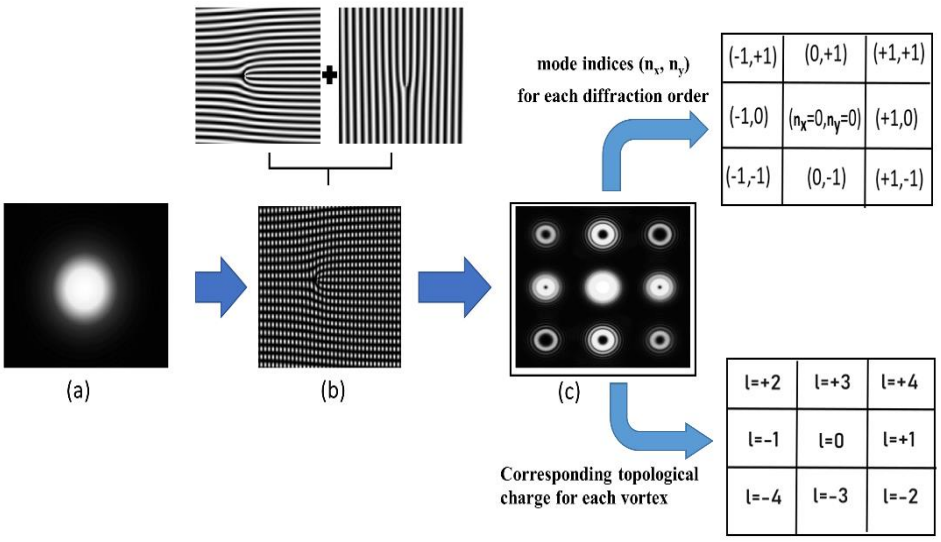

Figure 4-5: The simulation results demonstrate the underlying principle of generating multiple vortex beams. (a) Input Gaussian beam. (b) computer generated hologram of 2D fork grating (c) far-field intensity pattern.

The zeroth order $(n_x = 0, n_y = 0)$ beam is charged with $l = 0$ and used as a reference beam for alignment aid. We used the central spot in zero-order as a point of reference to which the optical system is aligned and to which all other parameters of the designed grating are referenced.

Since we are limited by the small size of the SLM with our SSPG, we opted for only detection of only four vortex beams with distinct topological charges, including the zero order. The conceptual representation of detection of the four topological charges is shown in Figure 4-6. These distinctive points are placed along two black dashed line (1st and 2nd lines) on the SSPG in Figure 4-6.

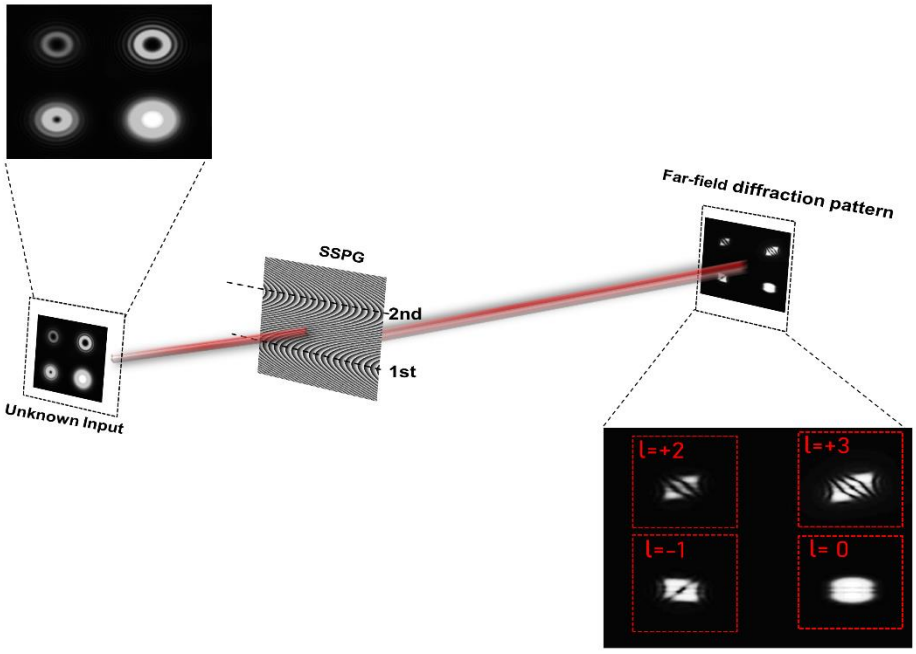

Figure 4-6: The conceptual representation of the numerical simulation for detection of multiple vortex beams using unique SSPG. The calculation parameters for the designed SSPG, Λx = 0.12mm, Λy = 8 mm, a=12. Other parameters are w_0=0.5mm, λ=632 nm, z=2m.

In particular, the detection method involves the selective use of spatially chosen diffraction orders: $(0,0), (-1,0), (-1,+1)$, and $(0,+1)$. These specific diffraction orders correspond to the identification of distinct topological charges: 0, -1, +2, and +3, respectively. This approach is specifically designed to detect multiple topological charges in their corresponding diffraction orders.

The two diffraction orders (0,0) and (-1, 0) with topological charges of $l = 0$ and $l = -1$, intersect the 1st black dashed line (shown on the SSPG hologram). The other two diffraction orders, $(-1,+1)$ and $(0,+1)$, intersect the 2nd black dashed line.

4.3 Experimental setup and detected results

The preceding numerical simulations have effectively showed how the far-field diffraction patterns resulting from an OV diffraction by unique SSPG can offer valuable insights into the OAM, particularly as the azimuthal mode index, denoted as l undergoes variations. This section will now transition from simulation to experimental implementation, putting these findings into practice.

The experimental setup to demonstrate the detection of OAM is shown in Figure 4-7. A frequency stabilized He-Ne laser at λ=632 nm(≈15mW) is used as the light source to provide the fundamental Gaussian beam. The laser beam is passed through a neutral density filter (NDF) to decrease the intensity of the beam so that it does not saturate the CCD camera. The spatial filter system (SF) before the SLM cleans the beam transverse intensity and creates a uniform Gaussian beam. The vortex beam was created in the far-field of the SLM. As previously presented, the holograms were of the form of forked diffraction gratings in order to impose a $2\pi l$ phase shift on the incident Gaussian beam, where l is the azimuthal mode index of the vortex beam. Subsequently, a 4f system is used to rescale the beam size, and an aperture in the Fourier plane of the SLM_1 was used to select the first diffraction order and blocking all other remaining parts. A half-waveplate (*HWP*) was used in order to rotate the polarization of the incident light beam to the optimum angle for the SLM_1 so as to maximize the power diffracted into the first-order.

The plane of SLM_1 was relay imaged through a beam splitter (BS) to a near-field CCD camera directly recording the beam intensity (CCD_1), and a second SLM (SLM_2) was used to perform detection of OAM state of light using SSPG. The diffracted field was detected by CCD_2 (The camera served to record and save the images onto the hard drive of a computer). The parameters for SSPG were set as Λ_x= 0.2 mm, Λ_y = 5 mm, and a = 12, which provide us with the most discernible fringes.

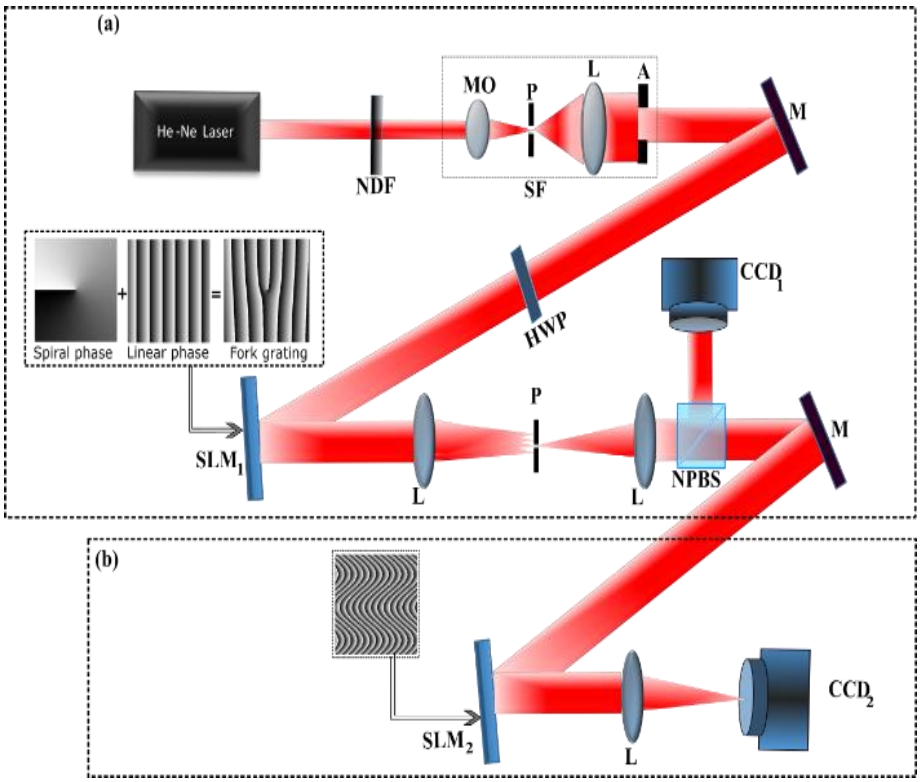

Figure 4-7: Schematic of experimental set-up (gray-levels correspond to phase values). NDF: neutral density filter, HWP: half-wave plate, MO: Microscope objective, P: Pinhole, CL: Collimated lens, Sf: Spatial filtering, A: Aperture, L: Lens, NPBS:non-polarizing Beam splitter, SLM: Spatial light modulator, CCD: Charged coupled device. (a) generation part, (b) detection part

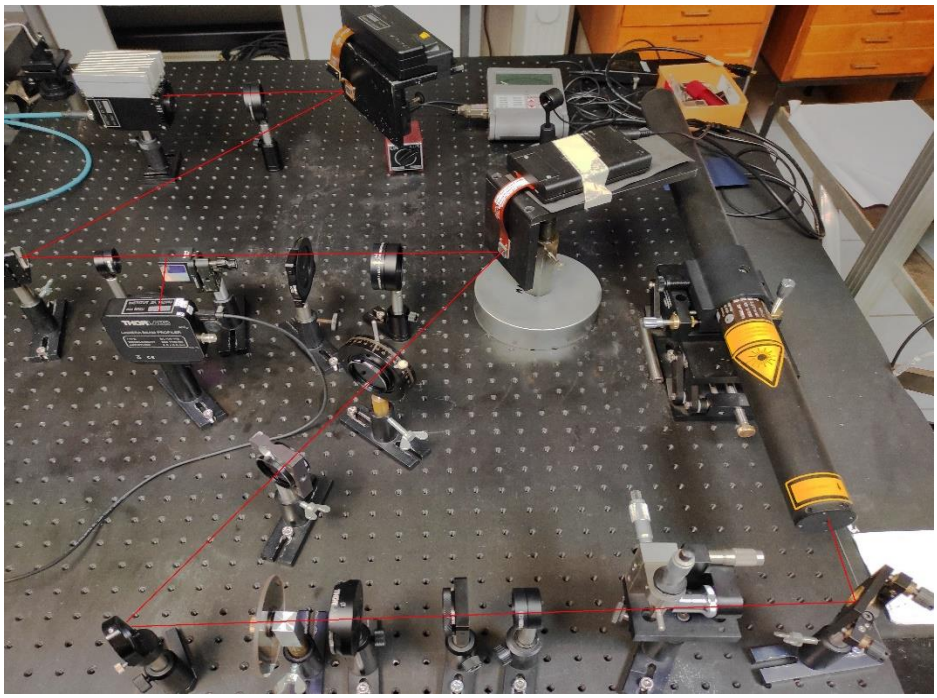

Figure 4-8: The experimental arrangement for generation and detection of optical vortex beam. L = lens, SLM = spatial light modulator, M = mirror, CCD = charge couple device camera, filter = ND filter, HWP: half wave plate, BS

4.4 Experimental results

4.4.1 Measured far-field intensity distribution for diffraction of vortex from SSPG

The experimental results obtained for the far-field diffraction intensity patterns are seen in Figure 4-10 for positive TC and Figure 4-11 for negative TC. The experimental results presented for positive values of l = +8, +10, +20, +25, +30, +40, +60, +80, +100 and +150 and subsequently for the same negative values. As can be seen the measured results show very good agreement with previous simulated results. Note that even l = 150 pattern renders detectable fringes (see Figure 4-9). Explicitly, one can count the dark stripes (|l|) or bright fringes (|l|+1) up to 150 from the diffraction pattern, and the pattern orientation is flipped when the sign of the azimuthal mode index is changed.

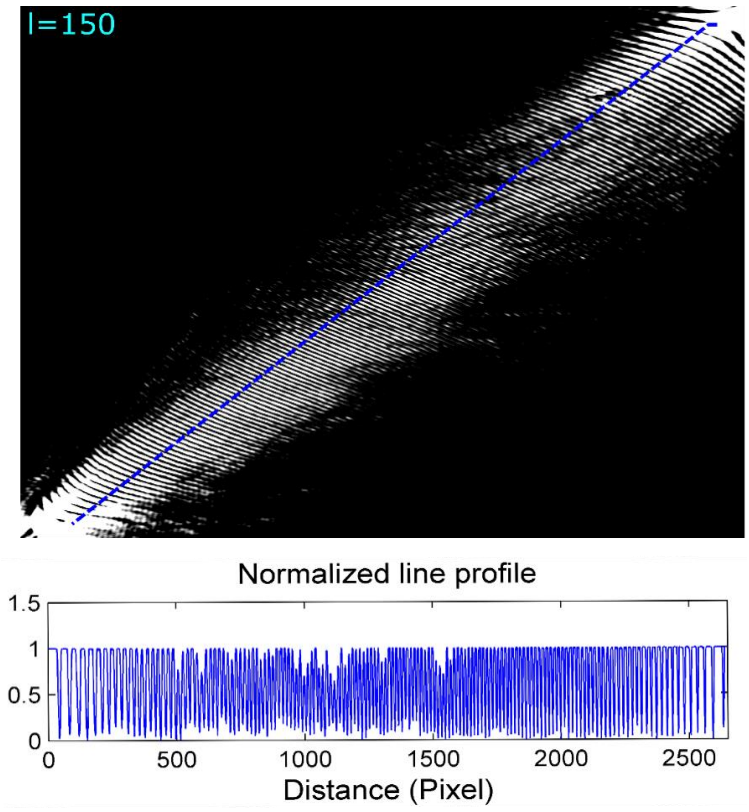

Figure 4-9: A close examination of the intensity profile for the experimental results corresponding to the highest detected OAM, $l = 150$, along with the line profile taken along a diagonal line.

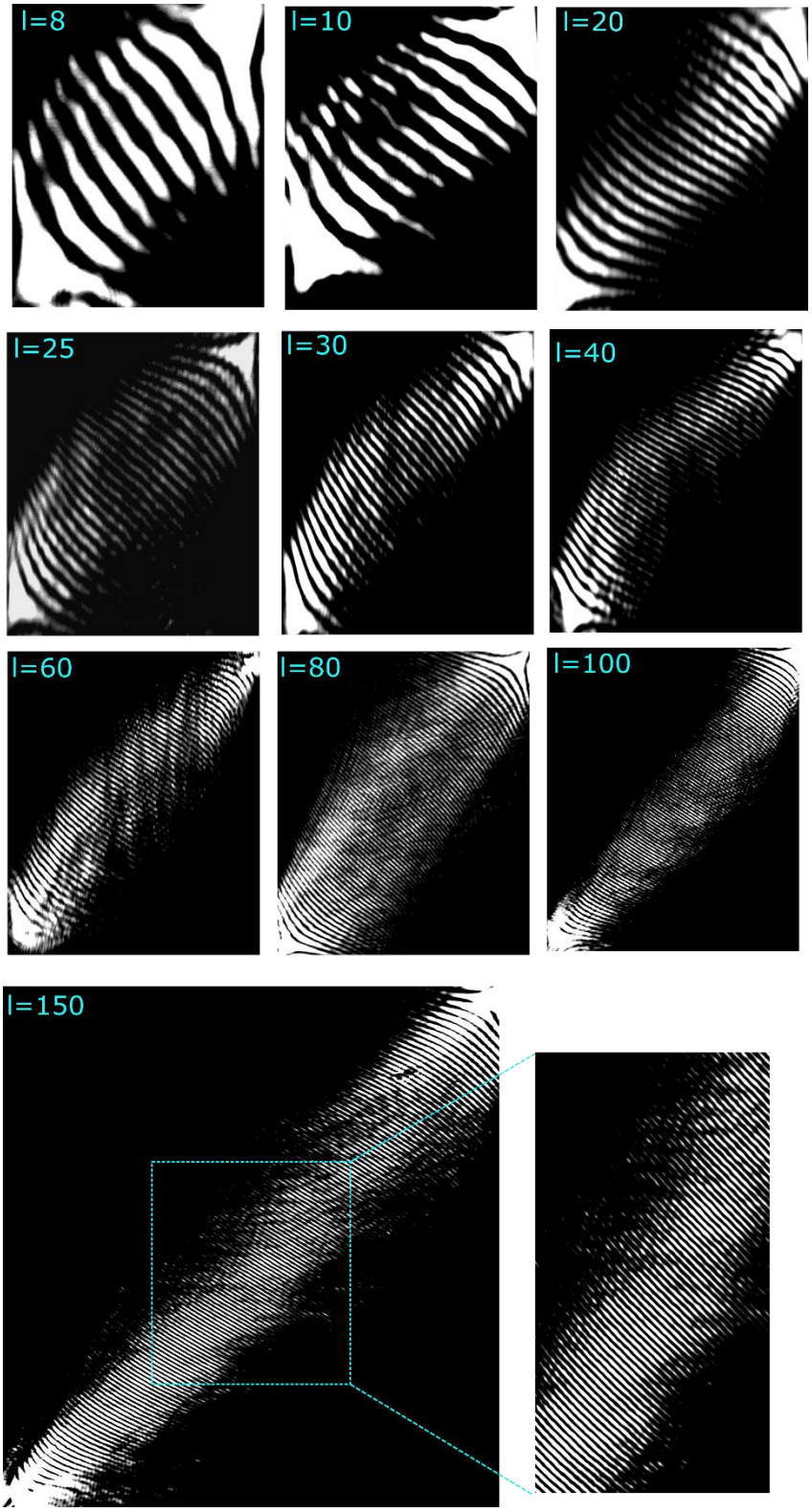

Figure 4-10: Experimental results for diffraction of optical vortex from designed SSPG for different positive OAM values.

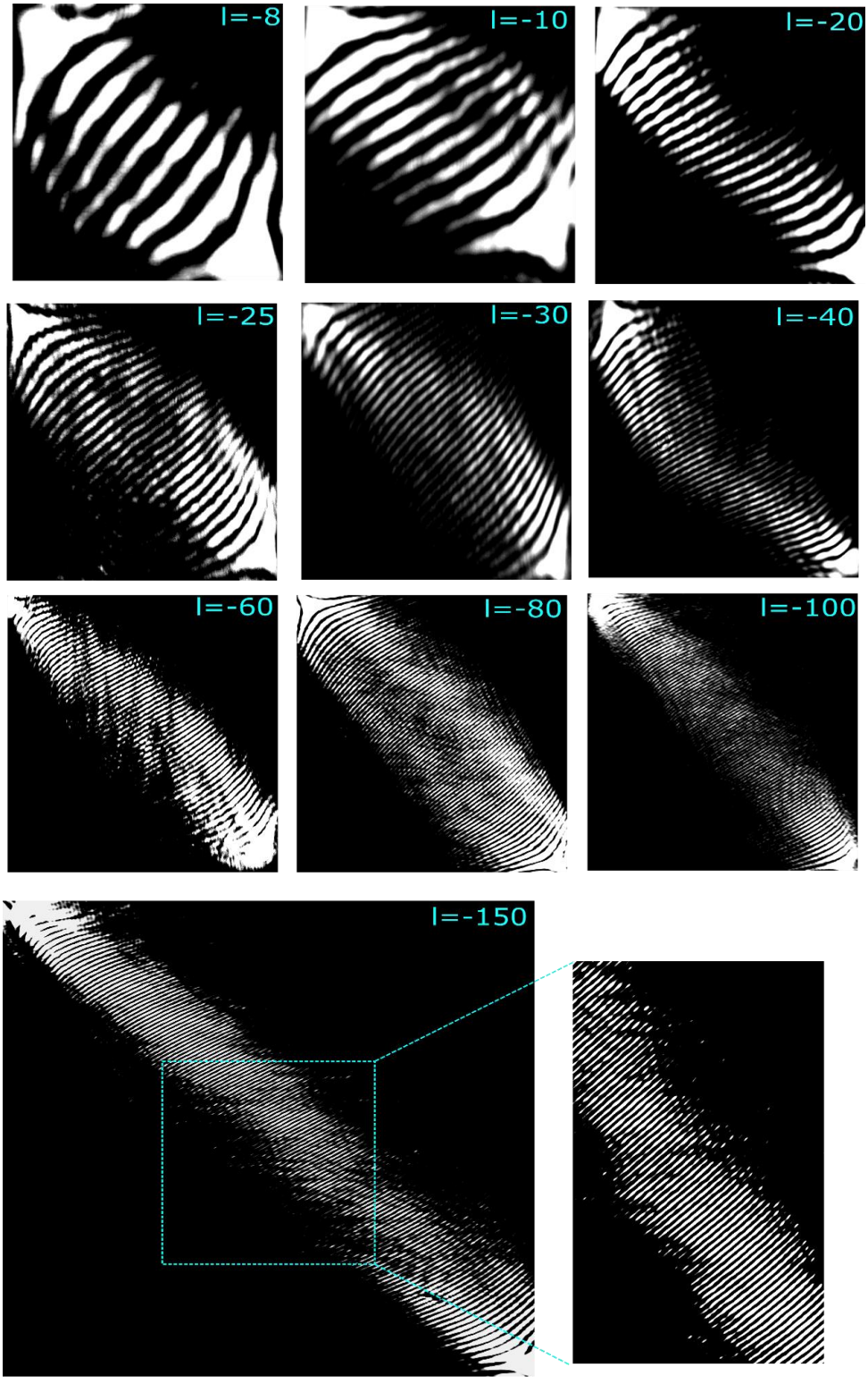

Figure 4-11: Experimental results for diffraction of optical vortex from designed SSPG for different negative OAM values.

4.4.2 Detection of multiple vortex beams using SSPG

The far-field intensity distribution for multiple vortex beams after passing SSPG is shown in Figure 4-12. Multiple vortex beams were detected for diffraction orders of $(n_x = 0, n_y = +1)$, $(n_x = +1, n_y = 0)$, $(n_x = -1, n_y = +1)$, $(n_x = +1, n_y = +1)$, for various topological chrages.

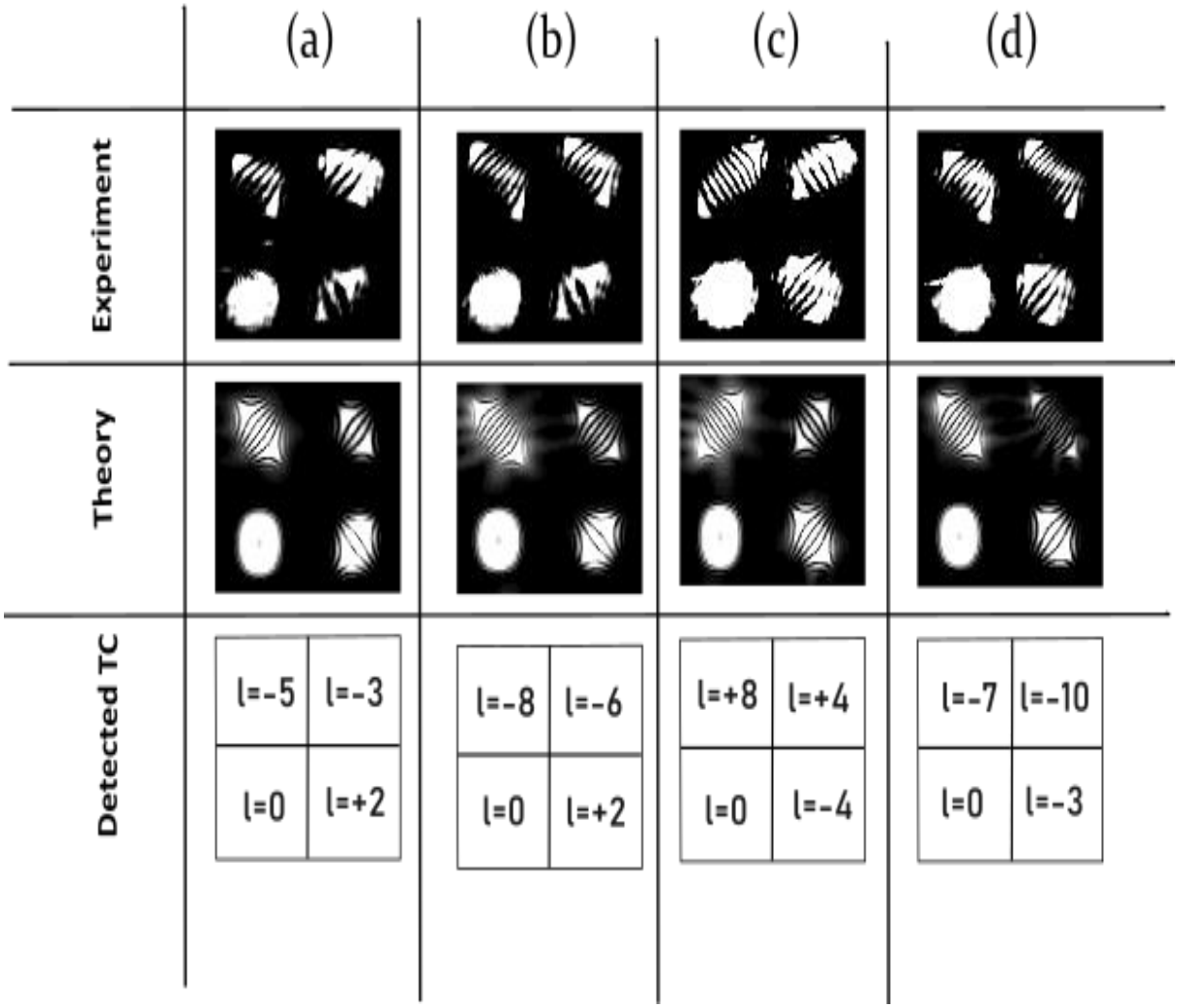

Figure 4-12: Experimental and simulation results for the detection of the multiple topological charges. The desired selected diffraction orders, represented by a dashed blue square, are shown in (a)-(d).

4.5 Adaptive nature of SSPG: fine-tuning for efficient TC detection

Before we end this chapter, we would like to talk about adaptive nature of SSPG using parameter a. We aim to investigate the influence of SSPG parameters on TC detection. We demonstrated the robust nature of the designed grating, specifically assessing its adaptability for effective TC detection. The designed diffraction grating is uniquely defined by three parameters: Λ_x, Λ_y, and a. These parameters play a crucial role in determining the characteristics and behavior of the grating. Altering Λ_x modify the spatial frequency of the linear phase in the x-direction. Consequently, this adjustment allows for control over the angle of the first diffraction order. The parameter Λ_y controls the period of the sinusoidal function in the y-direction. We performed the simulation using SSPG with fixed value of Λ_x and Λ_y while changing the a parameter. The corresponding results are listed in Figure 4-13. When the paremeter a is set within the range of 10 to 12, a relatively good conversion for detection results is obtained. This shows the importance of the a parameter of the proposed SSPG to the measurement effect and the adaptability of the SSPG. For different conditions, the necessary fine-tuning of SSPG can be made within this range to obtain clear and accurate transformation results. Therefore, the SSPG shows good adaptability to achieve the expected measurement results.

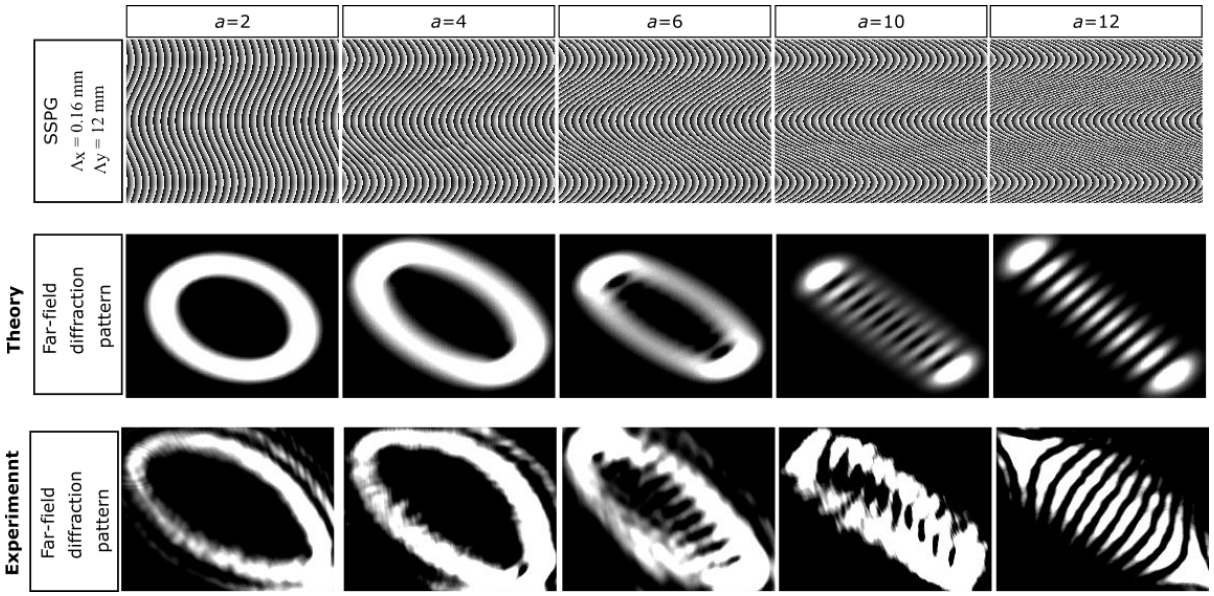

Figure 4-13: Outline of the SSPG with Λx = 0.16mm, Λy = 12mm and different $'a'$ parameters and their corresponding theoretical and experimental results in for $l = -10$. Other parameters are w_0=0.5mm, λ=632 nm, z=1.5m.

5 Investigating detection efficiency in the presence of laser beam misalignment tolerance

The robustness of a detection method to misalignment plays a crucial role in performance and precision of various applications. This consideration underscores the importance of designing detection methods that exhibit resilience to misalignment, ensuring reliable and robust detection of vortex beam. This chapter focuses on the tolerance of grating and examines the effects of beam misalignment on TC detection.

Nevertheless, the prerequisite for aligning the transmitting and receiving elements presents a significant challenge to the practical implementation of vortex beams. In an effort to comprehend the detection performance resulting from input beam misalignment, we begin by examining uniform beam steering to address two distinct misalignment scenarios: Off-axis horizontal displacement and off-axis vertical displacement within the SSPG plane. Subsequently, we proceed by studying the response of the detection system upon change of oblique angles and axis deviations. Both the theory and experiments demonstrate the impressive ability of SSPG to detect TC even when there's beam misalignment. This highlights SSPG's remarkable capability to accurately identify TC values despite potential alignment challenges.

5.1 SLM-Based Laser Beam Steering

To induce a transverse displacement in the laser beam incident on the plane of SSPG, we employed beam steering using a SLM. Laser beam steering techniques have witnessed remarkable advancements. Both mechanical [64] and non-mechanical [65] approaches have been developed for diverse requirements.

Mechanical methods typically utilize mirrors or prisms, whereas non-mechanical approaches involve technologies such as acousto-optic modulators and spatial light modulators. These techniques provide precise control and swift beam positioning, aligning with the requisites of contemporary applications. The methodology used in this study centers on the utilization of an SLM, and its underlying principle will be briefly explained.

SLMs present a compelling alternative to, and in some applications, a viable replacement for conventional mechanical beam steerers. SLMs offer several advantages, including the absence of moving components, reduced weight, compactness, and low power consumption. The theoretical capabilities of SLMs could be exceptionally high if it were feasible to generate flawless diffraction gratings. However, in practice, the phase distributions produced by today's available SLMs exhibit imperfections. This limitation is primarily attributed to factors such as pixelization and phase quantization inherent to SLMs. The small-scale pixel structures in relation to the thickness of the LC layer result in unwanted interference among neighboring pixels.

The technique of beam steering can be effectively implemented using CGH loaded on a SLM. By employing these holograms, characterized by linear phase profiles, it becomes possible to induce a one-dimensional transverse displacement of the beam spot at the focal plane of a lens. This approach offers precise control over the direction in which the optical beam is directed, thereby enabling targeted and dynamic steering. By applying a linearly varying phase delay the light will be deflected (Figure 5-1). The inherent periodic aspect of the phase finds frequent application, often employing phase gratings shaped with an amplitude of 2π.

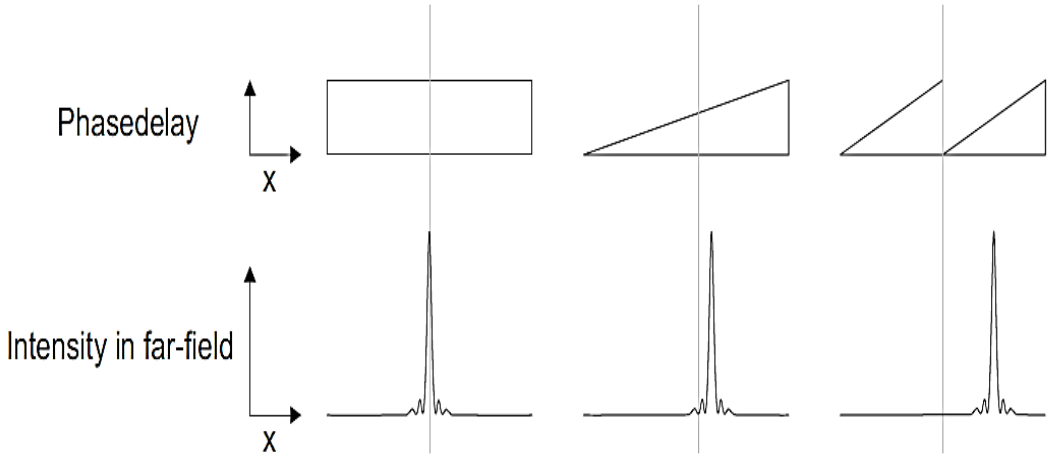

Figure 5-1 Illustrations displaying the deflection of a beam due to linear phase shifts. The phase distribution can be cyclically adjusted in increments of 2π to represent a blazed grating.

The spatial frequency of the blazed grating dictates the angle of deflection, while the linear phase shift creates an asymmetrical diffraction pattern in the far-field. The grating equation expresses the connection between the diffraction angle (β_m) for the qth diffraction order and the grating period (Λ) measured in pixel units.

$$\sin \beta_q = \frac{q\lambda}{\Lambda\delta} \tag{5-1}$$

Where λ is the wavelength and δ is the pixel pitch. The first diffraction order is commonly utilized for beam steering and the maximum deflection angle is then

$$\beta_{1,\max} = \pm \sin^{-1} \frac{\lambda}{2\delta} \tag{5-2}$$

Commercial SLMs typically feature pixel pitches from 6 to 30 μm, enabling maximum deflection angles spanning from 0.1° to 12.3° for wavelengths between 450nm to 1500nm. Employing small phase shifts across a broad beam area allows for precise and accurate beam steering.

5.2 **Results and discussion**

We theoretically and experimentally investigated the effect of the lateral shift of the incident vortex beam on the plane of SSPG in steps of 0.25 mm. The incident vortex with l =10 and the beam waist of 0.5 mm is displaced in two directions. The respective diffraction patterns are presented in Figure 5-2. The first 8 pictures (Figure 5-2 (a1) – (a8)) show theoretical results of vortex diffraction from SSPG, when the vortex center is displaced in vertical direction at 0, 0.25, 0.50, 0.75, 1.00, 1.25, 1.50 and 1.75 mm from the center, and next eight pictures (Figure 5-2 (b1) – (b8)) show the corresponding experimental results. It can be inferred that for vertical displacement the intensity pattern will be degraded when the incident vortex is approximately at inflection points of the sinusoidal function (Figure 5-2, (a4) and (a5)). As long as the center of the beam is close to either maximum or minimum (Figure 5-2, (a2), (a3), (a6) and (a7)) the TC of the vortex beam is still recognizable. From the results, it becomes evident that the far-field intensity exhibits ideal fringe visibility when positioned at the maximum, minimum, or in close proximity to these points. As anticipated, the theoretical and experimental results reveal that horizontal displacements do not induce any changes in the intensity pattern of diffracted field. This consistency underscores the robustness of the detection system in response to horizontal beam displacement, Figure 5-2 (c1) to (c4), and Figure 5-2 (d1) – (d4) shows the theoretical and experimental results, respectively.

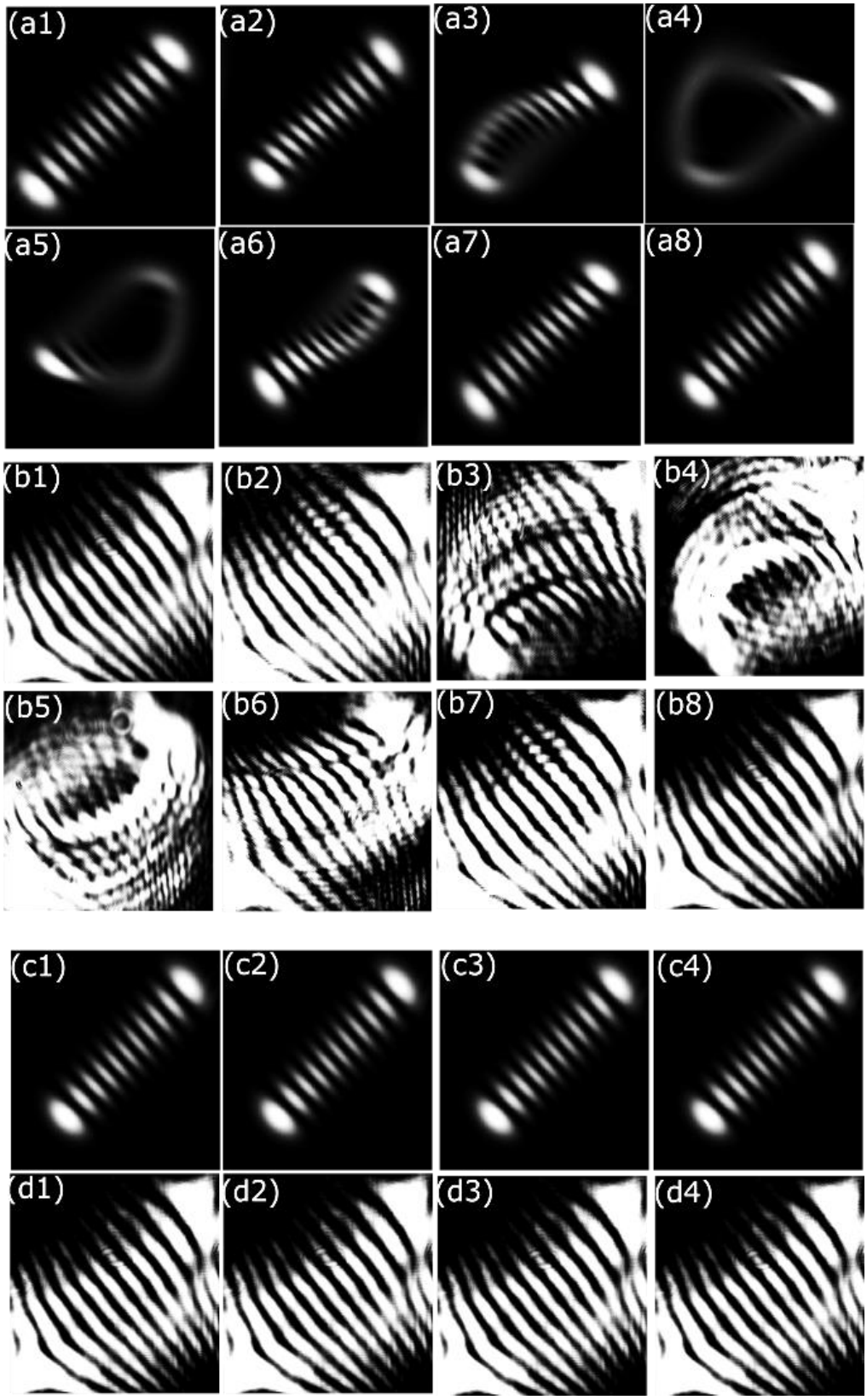

Figure 5-2: Simulation and the corresponding experimental for vortex beam with $l = 10$ results for lateral shift of the beam in vertical direction, (a1) – (a8): at 0, 0.25, 0.50, 0.75, 1.00, 1.25, 1.50 and 1.75 mm from the center, and (b1) – (b8) the corresponding experimental results and (c1) – (c4): in horizontal 0, 0.25, 0.50, 0.75 mm and (d1) – (d4) the corresponding experimental results.

Both theoretical and experimental findings indicate that fringe resolution is not strictly dependent on the position of the incident vortex beam. To be more specific, in Cartesian coordinates, certain points along the y-axis of SSPG (vertical direction), particularly those corresponding to local maxima or minima, yielded excellent fringe resolution. However, it is worth noting that there was a degradation in resolution at inflection points of the SSPG, yet the TC remained recognizable. Along the x-axis (horizontal direction), the diffraction pattern remained consistent. We successfully investigated the influence of vortex beam displacement on the TC detection, highlighting the versatility and reliability of the method. The lateral (horizontal) shift invariance of detection demonstrated here is highly advantageous, as it reduces the need for precise adjustments to the incident beam's position on the plane of SSPG. This intrinsic stability in the presence of lateral shifts significantly enhances the practicality and efficiency of optical systems, imparting valuable benefits for applications where misalignment can be a common challenge.

5.3 Effect of oblique illumination

For the investigation of the influence of the input angle, we varied the angles of SLM_2 across the SSPG plane. The experimental results (see Figure 5-3) demonstrate robust consistency even with varying rotations of SLM_2 at angles of 0°, 10°, and 15°. This stability highlights the method's ability to sustain performance reliability across diverse incident angles.

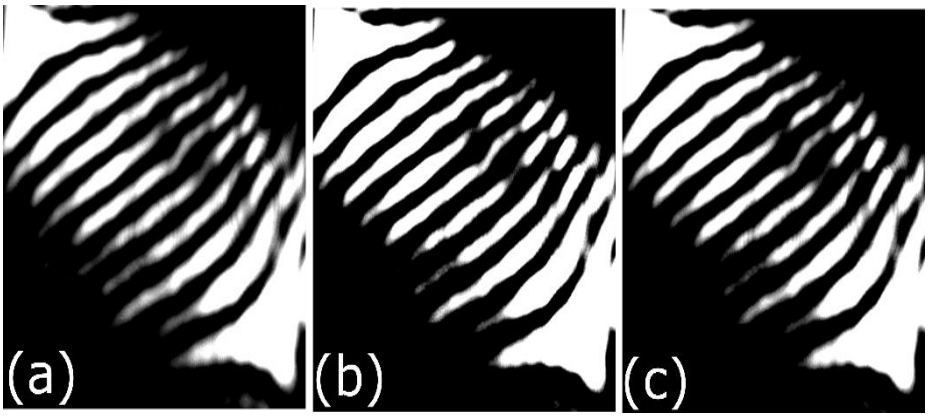

Figure 5-3 Experimental results for rotation of the second SLM by angles for (a) 0, (b) 10 and (c) 15 degrees for the l = -10 beam

6 Towards complete modal detection of LG beams

Harnessing the full advantage of the LG modes in different application requires detection over both the azimuthal and radial components. Studies indicate that precise manipulation of both radial and azimuthal aspects of LG mode has significantly contributed to the enhancement of classical communication protocols reliant on mode-division multiplexing schemes. [66]. It has also been instrumental in manipulating light propagation through complex media, finding applications in diverse fields such as imaging through multi-mode fibers [67] and the development of programmable optical circuits [68]. Furthermore, the ability to detect both mode indices of LG mode is essential for harnessing the benefits of high-dimensional encoding, which enhances communications by increasing their capacity. This access also facilitates noise-resistant entanglement distribution [69].

Chapter 2 laid the groundwork for exploring the capability of detecting both mode indices in any measurement technique. Furthermore, the optimal method and scheme to determine both the azimuthal and radial mode indices (l and p) remain unclear. While interferometric techniques have demonstrated multi-outcome detection for both the azimuthal and radial aspects of LG modes [70-72], their scalability is inherently complex.

In chapter 4, our examination focused on the detection of LG mode with a radial mode index set to zero $p = 0$, But LG_p^l modes are comprised of both an azimuthal mode index l and radial mode index denoted as p. The focus of this chapter revolves around detecting LG_p^l, where $p \neq 0$. Here, we extend our investigation to demonstrate the generation and detection of LG modes for the case when $p \neq 0$.

This chapter investigate the theoretical and experimental exploration of far-field diffraction intensity patterns for LG beams of different mode indices, l and p. As will be demonstrated, the incorporation of the radial index "p" significantly influences the characteristics of the far-field diffraction pattern. However, clear guidelines will be established to directly deduce both mode indices from the intricate far-field diffraction patterns. This systematic approach ensures a comprehensive understanding of the complex interplay between these indices, allowing for precise complete modal (including azimuthal and radial) detection of LG beams.

6.1 Generation of LG mode: theoretical framework and experimental results

LG modes arise from phase-modulating of an incoming Gaussian beam using an SLM loaded with a fork shaped hologram, where in polar coordinate the phase grating takes the form of

$$\ell\varphi = m\pi + \frac{2\pi r}{\Lambda}\cos\varphi \tag{6-1}$$

where $m = 0, \pm1, \pm2, ...$ and Λ *is* the pitch of the fork grating. The fork grating's diffraction angle can be altered by fine-tuning parameter Λ, optimizing the phase hologram within the transmission function formula represented as [73]:

$$T(r,\varphi) = e^{i\delta H(r,\varphi)} \tag{6-2}$$

where δ represent the amplitude of the phase modulation. The formula for the CGH can be written [73]:

$$H(r,\varphi) = \frac{1}{2\pi}\mathrm{mod}(\ell\varphi - \frac{2\pi}{\Lambda} r\cos\varphi, 2\pi) \tag{6-3}$$

Where $mod(a,b) = a - bint(a/b)$ is the reminder of a/b. As shown before, when $p = 0$, the generated hologram lacks radial nodes, and the bifurcation number is dependent upon the specific value of the l in Equation (6-3). However, when $p > 0$, its phase hologram is similar to that of $p = 0$; but one or more periodic radial nodes appear radially (see Figure 6-4).

LG modes with radial index $p \neq 0$ can be generated by the phase modulation of Gaussian beam with the following phase function:

$$\varphi_{phase}(r,\varphi) = -l\varphi + \pi\varphi\left(-L_p^{\ell}\left(2r^2/w_0^2\right)\right) \tag{6-4}$$

Where $L_p^{|l|}$ represents the Laguerre polynomial with parameters l and p. Figure 6-1, shows the simulation results of high-order LG beam generation. Figure 6-1(a) shows the fork grating required to generate the LG_3^3 beam and Figure 6-1(b) shows the fork grating required to generate LG_2^5.

The phase modulation function used in Figure 6-1(a) and (b), $is\ \varphi_{phase}(r,\varphi) = -l\varphi + \pi\varphi\left(-L_p^l(2r^2/w_0^2)\right)$ in which the beam-waist radius is w_0 =2.5 mm. As it can be seen, when $p > 0$, one or more circular dislocations appear in the fork grating of the LG beam.

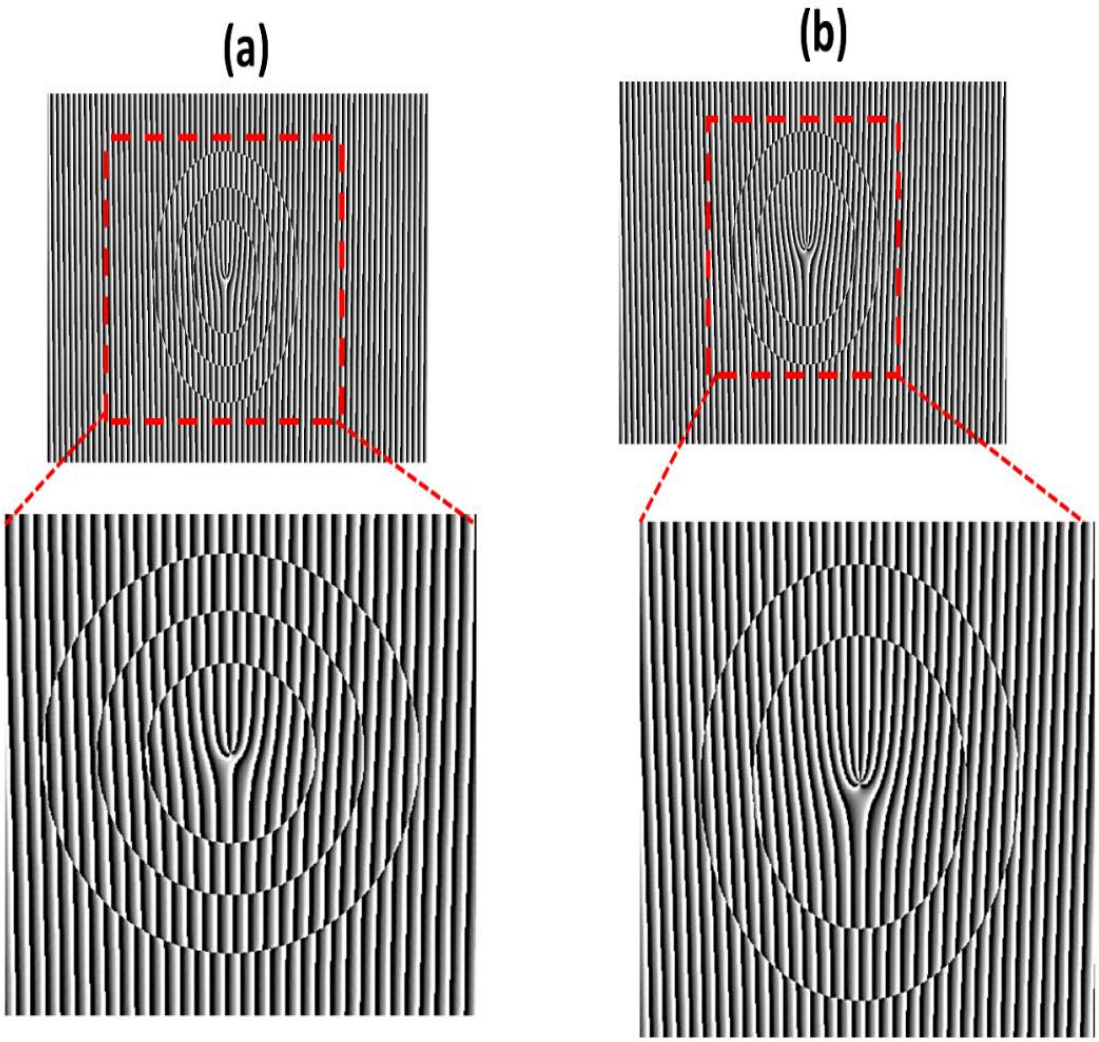

Figure 6-1: Numerically simulated with added closer view (a) Fork grating of $LG_3^3\ beam$, (b) Fork grating of beam LG_2^5

Examining the impact of the waist radius fork grating structure, we simulated the fork gratings of the LG_1^1 beam for different waist values. Figure 6-2(a) and (b) show fork hologram corresponding to LG_1^1 beams having a waist of w_0 =1.0 mm and 2.5 mm, respectively.

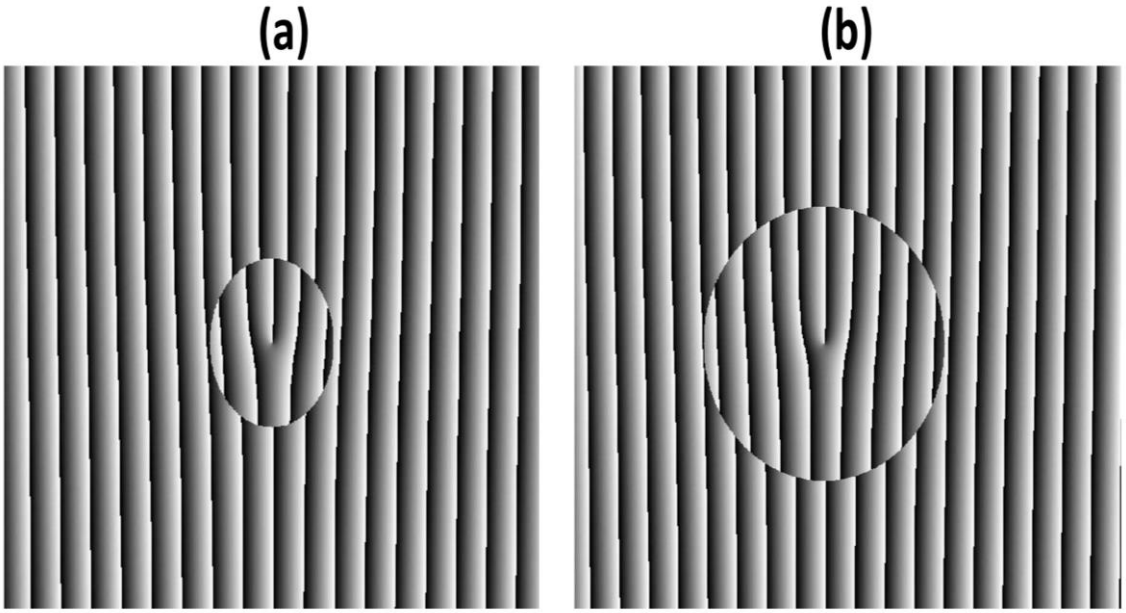

Figure 6-2: numerically simulated fork-shaped grating of LG_1^1 beam with (a) w_0 =1.0 mm and (b) 2.5 mm

The profiles of the fork grating in cases where $p \neq 0$ show interplay of the total phase governed by $\exp(il\varphi)$and Laguerre polynomial $L_p^{|\ell|}(2r^2/w_0^2)$ through the magnitude of w_0. As shown in Figure 6-2, the fork-grating profile of the LG_1^1 beam displays a circular dislocation. With a larger beam-waist radius, the size of this circular dislocation expands.

Figure 6-3, are the simulated and measured experimental results for intensity distribution of the LG_1^3, LG_2^3, LG_3^3 . The simulation parameters are set as follows: $\lambda = 632\ nm, w_0 = 1.0\ mm$.

Theoretical and experimental findings, depicted in Figure 6-3, illustrate that for $p > 0$, the light-intensity distribution of the LG beam displays a multi-ring intensity profile, where the count of bright rings corresponds to $p + 1$. The experimental outcomes align consistently with the theoretical simulation results.

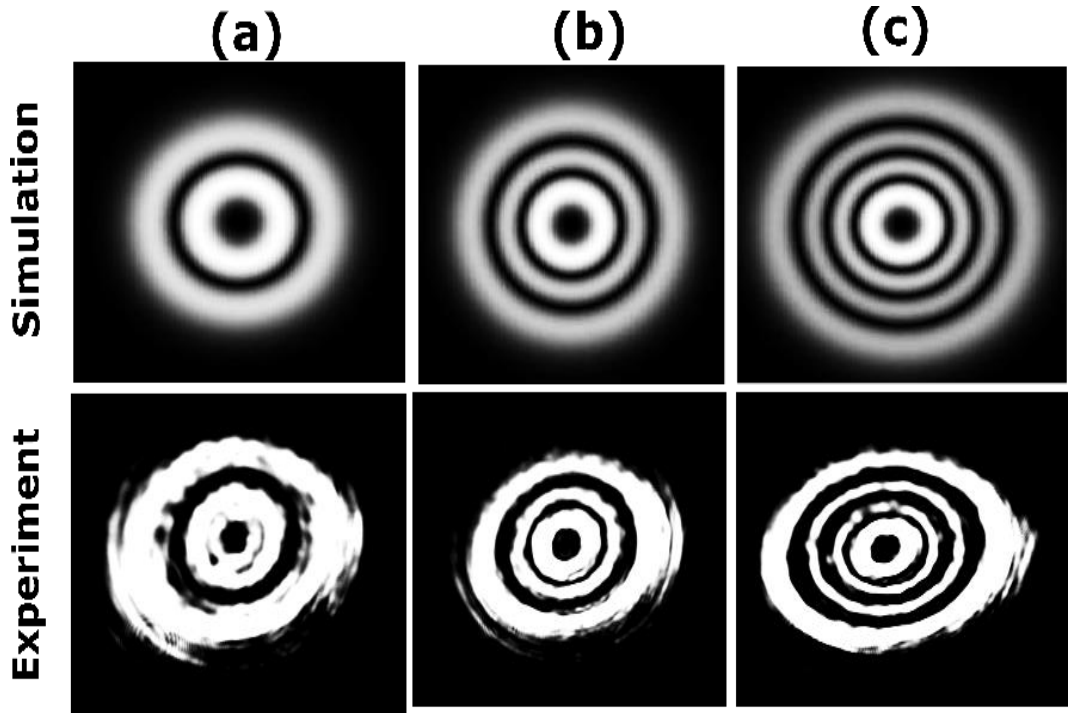

Figure 6-3 Numerical simulation and experimental results for LG beam (a) LG_1^3, (b) LG_2^3,(c) LG_3^3.

6.2 **Basic equations for diffraction of LG mode from SSPG**

In this section, we provide the governing equation for theoretical calculations of diffraction of an incident LG mode ($p \neq 0, l \neq 0$) with a wavelength of λ and an azimuthal index l and radial index p. The LG mode is centered on a sinusoidally-shaped phase grating located at z = 0, where "z" represents the propagation axis. As before, we employ the Fresnel integral for theoretical calculation of optical field at each plane of propagation. The optical field was initially propagated to the SSPG plane, where the incident field distribution was multiplied by the relevant transmission function of SSPG. This resulting field distribution was then propagated to the far-field ($z = 2m$). To describe the transverse coordinates on the aperture plane, we used Cartesian coordinates denoted as (x, y).

Expressed in Cartesian coordinates, the complex amplitude of an LG mode with a radial index $p \neq 0$ across the x_0-y_0 plane can be represented as [60]:

$$U\left(x_0, y_0\right) = \left(x_0 + i.\mathrm{sgn}\left(\ell\right) y_0\right)^{|\ell|} \exp\left(-\frac{x_0^2 + y_0^2}{w_0^2}\right) L_p^{|\ell|}\left(\frac{2\left(x_0^2 + y_0^2\right)}{w_0^2}\right) \tag{6-5}$$

where w_0 is the beam radius at z=0, l and p indicate the azimuthal mode index and radial mode index respectively.

The transmission function of the SSPG can be expressed as follows:

$$\tau(x_0, y_0) = \frac{1}{2\pi} Arg\left[\exp\left(i \frac{2\pi x_0}{\Lambda_x} - ia \sin(\frac{2\pi y_0}{\Lambda_y}) \right) + \pi \right] \quad (6\text{-}6)$$

Where Λ_x, Λ_y are the pitch of the grating in x and y direction respectively, Arg returns the argument of the exponential between -π and π, and a is the amplitude of sinusoidal modulation and parameter for fine tuning.

The vortex beam pass through the SSPG with a transmission function $\tau(x_0, y_0)$. The light beam complex amplitude field immediately after passing through the SSPG is:

$$U_t(x_0, y_0) = U(x_0, y_0)\tau(x_0, y_0) \quad (6\text{-}7)$$

Accounting for the phase function introduced by SSPG, the field distribution at the observation plane of x_1-y_1 at each plane of propagation, can be calculated using the Fresnel diffraction integral,

$$U(x_1, y_1; z) = h \int_{-\infty}^{+\infty} \int_{-\infty}^{+\infty} U_t(x_0, y_0) \exp\left[i\alpha\left(x_0^2 + y_0^2 - 2\left(x_0 x_1 + y_0 y_1 \right) \right) \right] dx_0 dy_0 \quad (6\text{-}8)$$

Where $h = \frac{1}{i\lambda z} exp[ikz + i\alpha(x_1^2 + y_1^2)]$ and $\alpha = \frac{\pi}{z\lambda}$.

As depicted in Figure 6-4, and from the theoretical results it can be seen that diffraction of $LG_{p\neq 0}^{l}$ from SSPG comprised of multi-row or multi-columns intensity distribution. This phenomenon can be directly understood as each ring of the LG mode is diffracted into a new row or column.

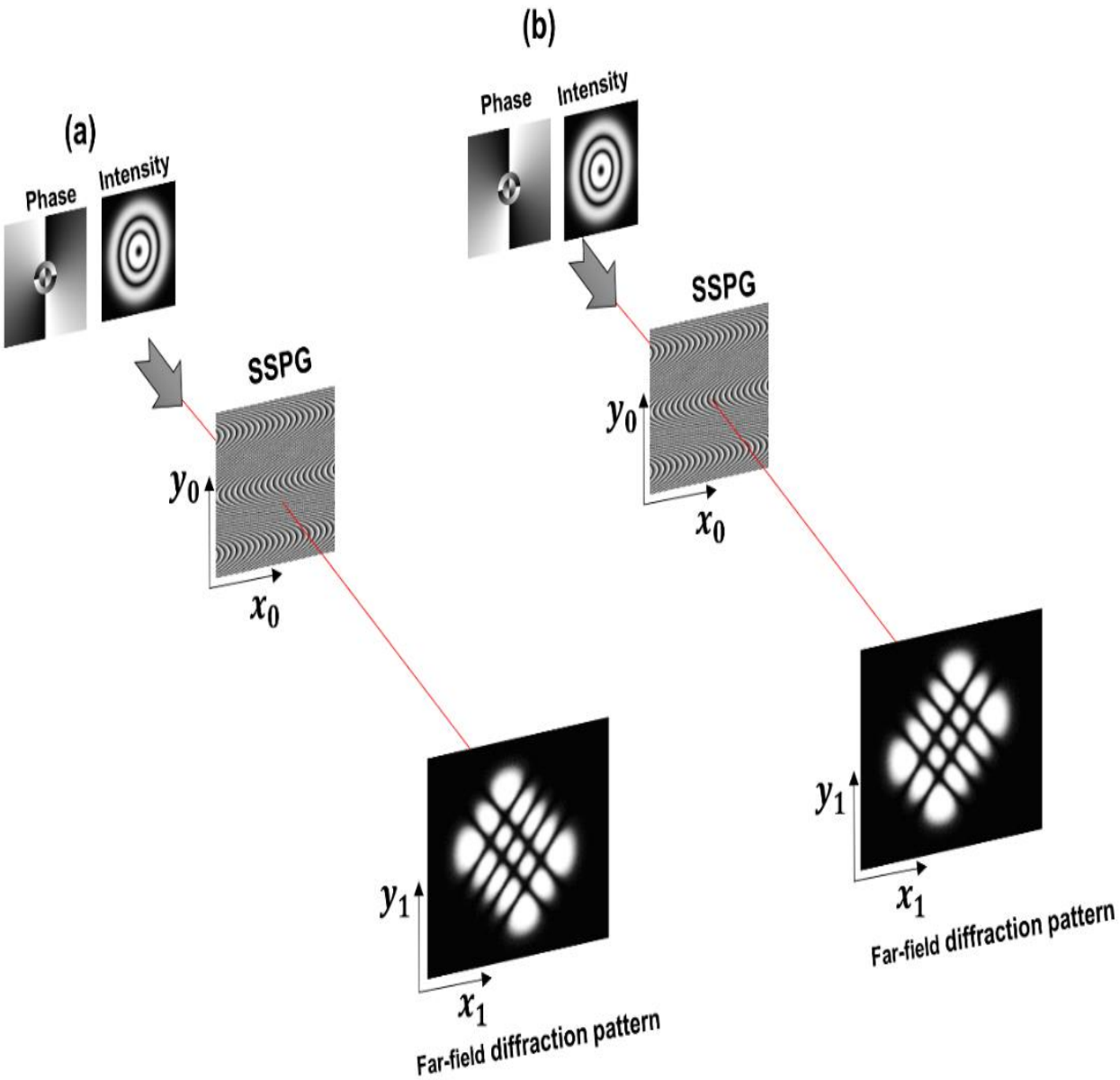

Figure 6-4 Simulation results for the far-field intensity distribution after passing through SSPG for (a) $l = -2, p = 2$ and (b) $l = +2, p = 2$. The parameters for SSPG were set as Λ_x= 0.16mm, Λ_y= 12mm, and a = 12, z = 2m which provide us with the most discernible fringes.

6.2.1 Complete modal detection of LG mode: simulation results

Within this section, we aim to analyze the utilization of SSPG for the detection of multi-ring vortex LG beams. The theoretical results calculated from Fresnel integral (Figure 6-4) show that the far-field diffraction pattern has sub bright spots of the diffraction field in arrays of $n \times m$, as illustrated in Figure 6-5.

By analysis of intensity profile it can be deduced that for multi-ring vortex beams, the radial index p can be determined using the following relation:

$$p = Min(m,n) - 1 \tag{6-9}$$

where $Min(m,n)$ denotes taking smaller value. The values for m and n represent the count of bright spots within an array, indicated respectively by the red and blue arrows.

The subtraction of number of sub bright spots in the diffracted field is associated with $|l|$:

$$|\ell| = m - n \tag{6-10}$$

The determination of the sign of the topological charge l involves observing the arrangement direction of diffracted spots corresponding to the $Max(m,n)$ value. A diagonal arrangement indicates a positive l, while an anti-diagonal arrangement signifies a negative l. This process is visually represented in Figure 6-5.

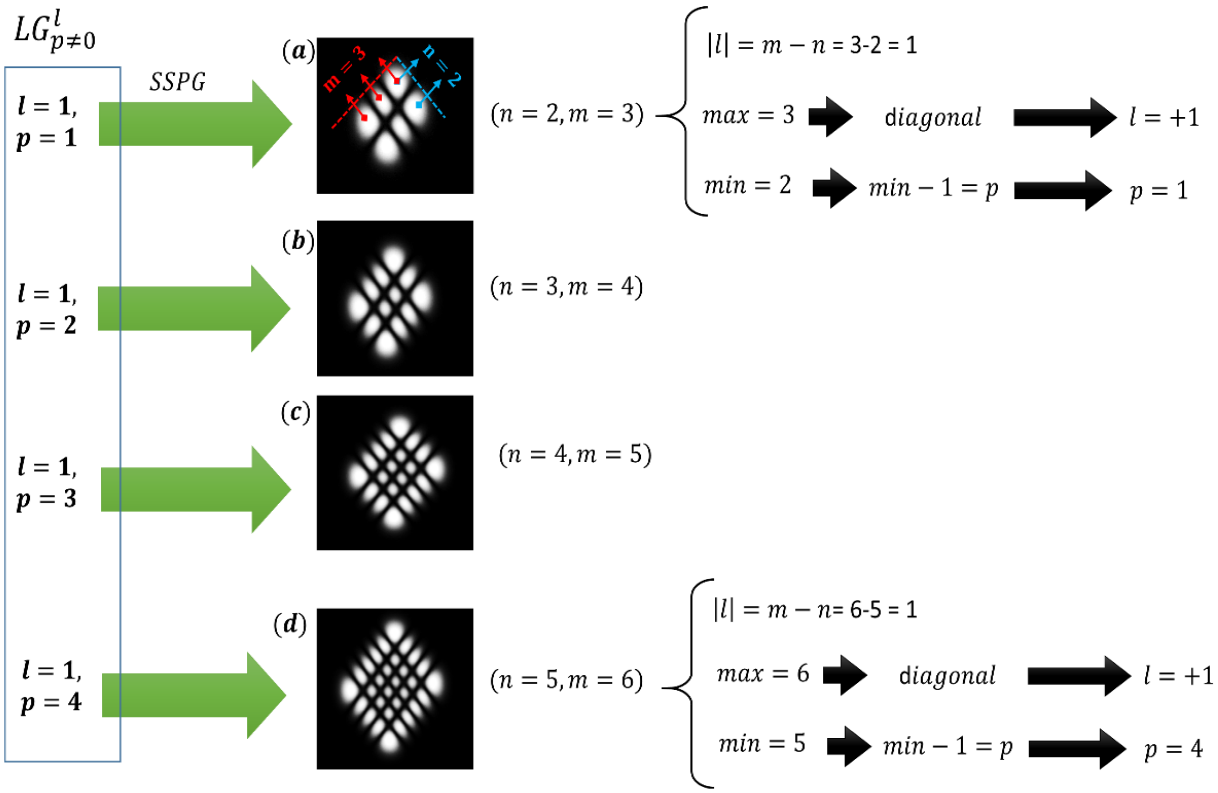

Figure 6-5 The procedure for detecting the $LG^{1}_{p=1,2,3,4}$ mode from the far-field diffraction pattern from SSPG (Green arrows indicate the resultant pattern after diffraction from the SSPG).

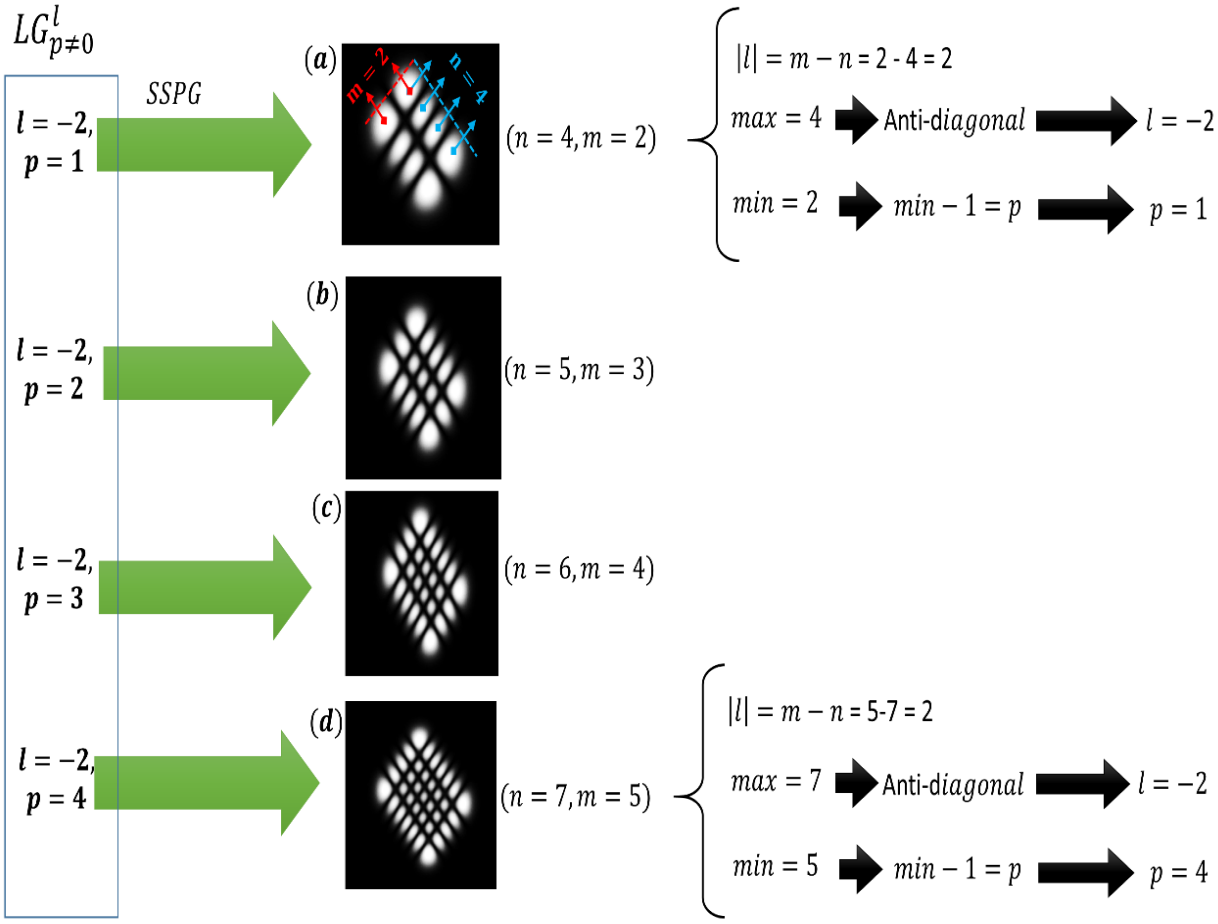

Figure 6-6: The procedure for detecting the $LG^{-2}_{p=1,2,3,4}$ mode from the far-field diffraction pattern from SSPG (Green arrows indicate the resultant pattern after diffraction from the SSPG).

6.2.2 Experimental detection of higher order LG mode using SSPG

The experimental configuration remains consistent with the previous setup, albeit with a modification: the first SLM is now loaded with fork-shaped holograms using different azimuthal and radial mode indices. The Figure 6-7, presents the theoretical and detected results for different LG modes. It is evident that there is a good agreement between both theoretical and measured results.

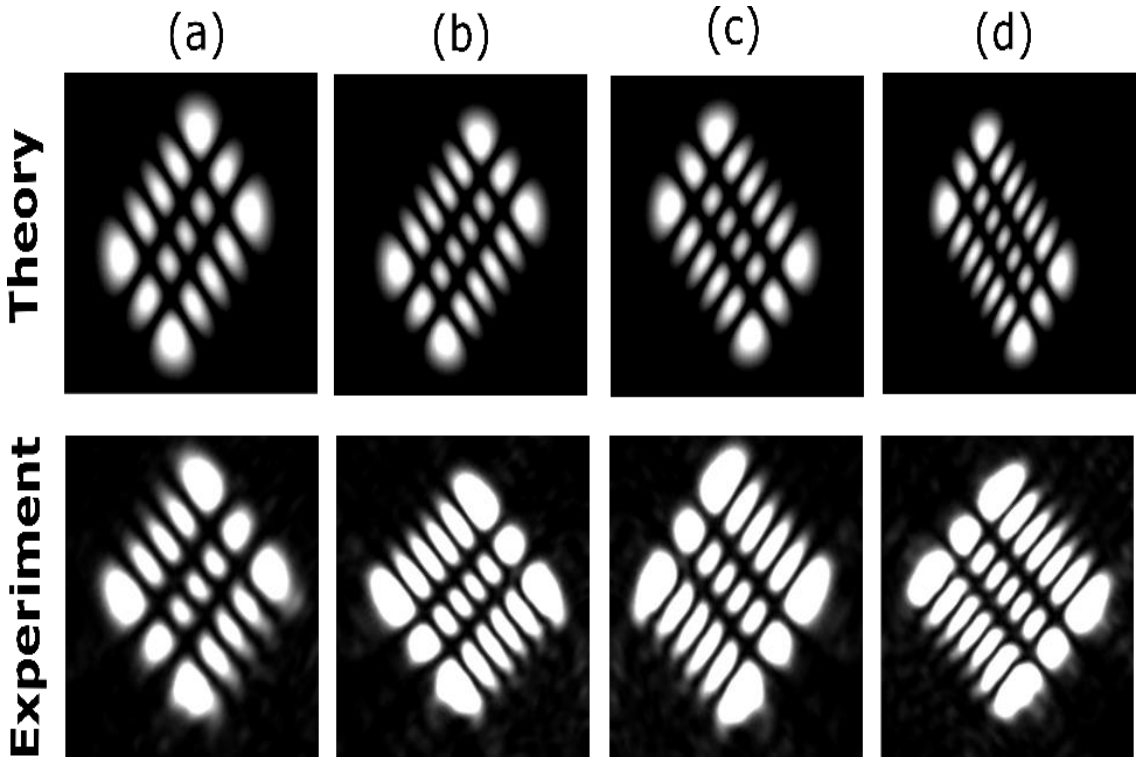

Figure 6-7: Theoretical and experimental results of far-field diffractions when multi-ring LG beams are diffracted by SSPG. (a) LG_2^2, (b) LG_3^4, (c) $LG_3^{-4}$and (d) LG_4^{-5}

In summary, a systematic approach for the comprehensive modal detection of LG modes from the far-field diffracted light field of SSPG can be outlined. Firstly, enumerate the count of bright spots within the m and n arrays. Then, calculate the radial index (p) using Equation (6.9). Subsequently, compute the absolute value of the topological charge $|l|$ by subtracting m from n. Lastly, based on the maximum value derived from m and n, observe the orientation of the spots; a diagonal orientation signifies a positive l, while an anti-diagonal orientation indicates a negative l.

7 Conclusion and future work

The primary objective of this research was to efficiently and robustly detect the OAM carrying in optical vortex beams. The thesis proposes a new grating for this purpose that we named sinusoidally shaped phase grating (SSPG). The SSPG can be fine-tuned only using three parameters. Our methodology's effectiveness was examined through Fresnel diffraction integrals and later confirmed through experimental results. This research was accompanied by the development of a Matlab code for the rapid implementation of various designed phase modulations for both generation and detection parts. Both theoretical calculation and experimental validations lead to the conclusion that this method stands out for its robustness and efficiency in detecting higher-order LG modes where the mode index for $l, p \neq 0$. The behavior of the far-field diffraction intensity pattern was shown to be dependent upon the mode index of LG mode.

Chapter two, comprised a literature review of various techniques employed in detecting OAM. However, we wanted to highlight the advantage of our method in contrast to other techniques in terms of robustness and ability to detect higher order LG modes. In contrast to interferometric methods, our approach simplifies the process by eliminating the need for a second beam. Furthermore, our method shows exceptional robustness and impressive tolerance to beam misalignment, a critical advantage. This capability holds particular value in applications where small deviation of the beam within an optical system can affect OAM detection. Both theoretical and experimental findings indicate that the OAM detection efficiency, is notably high when the vortex resides at the center of the maximum or minimum of SSPG, whereas degradation of fringes occurs at inflection points of the grating, but still OAM state of light is recognizable. The change of orientation of far-field diffraction pattern associated to l value showed to be useful for detecting negative and positive topological charges. We show the robustness of our method by showing the detection results for high order topological charge up to $l = \pm 150$. Actually, we are confident that with our method the values of the azimuthal mode indices, l, can go up to even higher values by using SLMs with higher resolution and higher fill factor. This proves that our design, although simple and modest, is robust and could achieve the main goals for this work. The grating's adaptability in fine-tuning parameters finds crucial application in scenarios where optical systems have aberrations.

Furthermore, our research demonstrates the ability of the proposed grating to detect fractional charges. The simulation results demonstrate that SSPG possesses the capability to detect fractional topological

charges, rendering it more applicable for specific applications where the detection of fractional charges is a requisite. Our grating's ability to detect fractional topological charges and multiple OAM modes underscores its immense value across various applications in optical and quantum communication.

Another intriguing aspect of the SSPG was its unique design enabling the simultaneous detection of multiple TC. We successfully detected four distinct TCs simultaneously. This unique capability showcases the versatility and efficiency of the SSPG in handling complex optical scenarios, offering a valuable tool for applications that involve the manipulation and analysis of multiple TC.

In the final chapter, we underscored the importance of LG modes, highlighting their distinctive features when both radial and azimuthal modes are present. Our proposed grating demonstrates remarkable efficacy in detecting LG modes, particularly when $p \neq 0$. The results indicate the exceptional performance of the grating in detecting such modes, emphasizing its versatility and potential impact on applications demanding precise control over spatial modes.

Our research lays the groundwork for exciting possibilities in future investigations and innovations. One avenue for exploration involves integrating our proposed grating with cutting-edge technologies. By incorporating machine learning algorithms or adaptive optics, we envision enhancing the grating's capabilities and expanding its applications. Furthermore, our research suggests potential applications in the realm of quantum optics and information processing. Investigating how our proposed grating could contribute to secure communication and advancements in quantum computing opens new frontiers in these fields.

In this research, we explored the response of our SLM under various phase modulations, employing pure-phase modulation for both generation and detection. To gain deeper insights into the implications of our findings and chart a course for future investigations, it would be worthy to consider a shift towards exploring the generation and detection of OAM using complex amplitude modulation.

Future studies could enrich this exploration by incorporating advanced optical modulation techniques, and in particular, by leveraging the capabilities of a digital micro-mirror device (DMD). The integration of complex amplitude modulation techniques, coupled with innovative device technologies, may offer enhanced control and manipulation of OAM, opening up new possibilities for applications in fields such as quantum communication, optical communication.

There are many more interesting questions that could be researched in future research. Here, I give my personal list of possible future topics in OAM detection system.

1- Detection of collinear superposition of OAM beams

2- Detection of higher order non-collinear superposition of OAM beams using diffraction

3- Detection of OAM of light at the single photon level

4- Evaluation of the influence of digital micro-mirror device on OAM detection efficiency

5- Development of an algorithm for automated OAM detection

8 Bibliography

1. Maxwell, J.C., *A dynamical theory of the electromagnetic field*. 1996: Wipf and Stock Publishers.
2. Poynting, J.H., *The wave motion of a revolving shaft, and a suggestion as to the angular momentum in a beam of circularly polarised light.* Proceedings of the Royal Society of London. Series A, Containing Papers of a Mathematical and Physical Character, 1909. **82**(557): p. 560-567.
3. Beth, R.A., *Mechanical detection and measurement of the angular momentum of light.* Physical Review, 1936. **50**(2): p. 115.
4. Darwin, C.G., *Notes on the theory of radiation.* Proceedings of the Royal Society of London. Series A, Containing Papers of a Mathematical and Physical Character, 1932. **136**(829): p. 36-52.
5. Allen, L., et al., *Orbital angular momentum of light and the transformation of Laguerre-Gaussian laser modes.* Physical review A, 1992. **45**(11): p. 8185.
6. Nye, J.F. and M.V. Berry, *Dislocations in wave trains.* Proceedings of the Royal Society of London. A. Mathematical and Physical Sciences, 1974. **336**(1605): p. 165-190.
7. Berry, M.V., J.F. Nye, and F.J. Wright, *The elliptic umbilic diffraction catastrophe.* Philosophical Transactions of the Royal Society of London. Series A, Mathematical and Physical Sciences, 1979. **291**(1382): p. 453-484.
8. Allen, L., M. Padgett, and M. Babiker, *IV The orbital angular momentum of light*, in *Progress in optics*. 1999, Elsevier. p. 291-372.
9. Poynting, J.H., *On the transfer of energy in the electromagnetic field.* Proceedings of the Royal Society of London, 1883. **36**(228-231): p. 186-187.
10. He, H., et al., *Direct observation of transfer of angular momentum to absorptive particles from a laser beam with a phase singularity.* Physical review letters, 1995. **75**(5): p. 826.
11. Ashkin, A., et al., *Observation of a single-beam gradient force optical trap for dielectric particles.* Optics letters, 1986. **11**(5): p. 288-290.
12. Simpson, N., L. Allen, and M. Padgett, *Optical tweezers and optical spanners with Laguerre–Gaussian modes.* Journal of modern optics, 1996. **43**(12): p. 2485-2491.
13. Dholakia, K., et al., *Second-harmonic generation and the orbital angular momentum of light.* Physical Review A, 1996. **54**(5): p. R3742.
14. Mair, A., et al., *Entanglement of the orbital angular momentum states of photons.* Nature, 2001. **412**(6844): p. 313-316.
15. Padgett, M.J. and J. Courtial, *Poincaré-sphere equivalent for light beams containing orbital angular momentum.* Optics letters, 1999. **24**(7): p. 430-432.
16. Gibson, G., et al., *Free-space information transfer using light beams carrying orbital angular momentum.* Optics express, 2004. **12**(22): p. 5448-5456.
17. Yao, A.M. and M.J. Padgett, *Orbital angular momentum: origins, behavior and applications.* Advances in optics and photonics, 2011. **3**(2): p. 161-204.
18. Tamburini, F., et al., *Encoding many channels on the same frequency through radio vorticity: first experimental test.* New journal of physics, 2012. **14**(3): p. 033001.
19. Wang, J., et al., *Terabit free-space data transmission employing orbital angular momentum multiplexing.* Nature photonics, 2012. **6**(7): p. 488-496.
20. Bourennane, M., A. Karlsson, and G. Björk, *Quantum key distribution using multilevel encoding.* Physical Review A, 2001. **64**(1): p. 012306.

21. Gröblacher, S., et al., *Experimental quantum cryptography with qutrits.* New Journal of Physics, 2006. **8**(5): p. 75.
22. Liu, B., Y. Cui, and R. Li, *A broadband dual-polarized dual-OAM-mode antenna array for OAM communication.* IEEE Antennas and Wireless Propagation Letters, 2016. **16**: p. 744-747.
23. Wang, B., et al., *Improved lateral resolution with an annular vortex depletion beam in STED microscopy.* Optics letters, 2017. **42**(23): p. 4885-4888.
24. Gahagan, K. and G.J. Swartzlander, *Optical vortex trapping of particles.* Optics Letters, 1996. **21**(11): p. 827-829.
25. Swartzlander, G.A., et al., *Astronomical demonstration of an optical vortex coronagraph.* Optics express, 2008. **16**(14): p. 10200-10207.
26. Forbes, K.A. and G.A. Jones, *Optical vortex dichroism in chiral particles.* Physical Review A, 2021. **103**(5): p. 053515.
27. Katoh, M. *Optical vortex emitted from free electrons in nature*. in *Light in Nature VII*. 2019. SPIE.
28. Beijersbergen, M., et al., *Helical-wavefront laser beams produced with a spiral phaseplate.* Optics communications, 1994. **112**(5-6): p. 321-327.
29. Rubano, A., et al., *Q-plate technology: a progress review.* JOSA B, 2019. **36**(5): p. D70-D87.
30. Piccirillo, B., et al., *Photon spin-to-orbital angular momentum conversion via an electrically tunable q-plate.* Applied Physics Letters, 2010. **97**(24): p. 241104.
31. Gutiérrez-Vega, J.C., *Pancharatnam–Berry phase of optical systems.* Optics letters, 2011. **36**(7): p. 1143-1145.
32. Gabor, D., *Holography, 1948-1971.* Science, 1972. **177**(4046): p. 299-313.
33. Gabor, D., W.E. Kock, and G.W. Stroke, *Holography: The fundamentals, properties, and applications of holograms are reviewed.* Science, 1971. **173**(3991): p. 11-23.
34. Brady, D.J. *Leith-Upatnieks holography in computational sensors*. in *Optical Information Systems IV*. 2006. SPIE.
35. Waters, J.P., *Holographic image synthesis utilizing theoretical methods.* Applied physics letters, 1966. **9**(11): p. 405-407.
36. Raisanen, A., et al. *Computer-generated holograms for mm-and submm-wave beam shaping*. in *Twenty Seventh International Conference on Infrared and Millimeter Waves*. 2002. IEEE.
37. Guo, C.-S., et al., *Optimal annular computer-generated holograms for the generation of optical vortices.* JOSA A, 2005. **22**(2): p. 385-390.
38. Guo, Z., S. Qu, and S. Liu, *Generating optical vortex with computer-generated hologram fabricated inside glass by femtosecond laser pulses.* Optics communications, 2007. **273**(1): p. 286-289.
39. Carpentier, A.V., et al., *Making optical vortices with computer-generated holograms.* American Journal of Physics, 2008. **76**(10): p. 916-921.
40. Bekshaev, A., O. Orlinska, and M. Vasnetsov, *Optical vortex generation with a "fork" hologram under conditions of high-angle diffraction.* Optics communications, 2010. **283**(10): p. 2006-2016.
41. Palmer, C. and E.G. Loewen, *Diffraction grating handbook.* 2005.
42. Hristov, H.D. and M.H. Herben, *Millimeter-wave Fresnel-zone plate lens and antenna.* IEEE Transactions on Microwave Theory and Techniques, 1995. **43**(12): p. 2779-2785.
43. Janicijevic, L. and S. Topuzoski, *Fresnel and Fraunhofer diffraction of a Gaussian laser beam by fork-shaped gratings.* JOSA A, 2008. **25**(11): p. 2659-2669.

44. Schonbrun, E., et al., *3D interferometric optical tweezers using a single spatial light modulator.* Optics express, 2005. **13**(10): p. 3777-3786.
45. Preece, D., et al., *Independent polarisation control of multiple optical traps.* Optics express, 2008. **16**(20): p. 15897-15902.
46. Andrews, D.L. and M. Babiker, *The angular momentum of light*. 2012: Cambridge University Press.
47. Nieminen, T.A., N.R. Heckenberg, and H. Rubinsztein-Dunlop, *Optical measurement of microscopic torques.* Journal of Modern Optics, 2001. **48**(3): p. 405-413.
48. Padgett, M., et al., *An experiment to observe the intensity and phase structure of Laguerre–Gaussian laser modes.* American Journal of Physics, 1996. **64**(1): p. 77-82.
49. Hickmann, J., et al., *Unveiling a truncated optical lattice associated with a triangular aperture using light's orbital angular momentum.* Physical review letters, 2010. **105**(5): p. 053904.
50. O'holleran, K., M.J. Padgett, and M.R. Dennis, *Topology of optical vortex lines formed by the interference of three, four, and five plane waves.* Optics Express, 2006. **14**(7): p. 3039-3044.
51. Soskin, M., et al., *Topological charge and angular momentum of light beams carrying optical vortices.* Physical Review A, 1997. **56**(5): p. 4064.
52. Liu, Y. and J. Pu, *Measuring the orbital angular momentum of elliptical vortex beams by using a slit hexagon aperture.* Optics Communications, 2011. **284**(10-11): p. 2424-2429.
53. Berkhout, G.C. and M.W. Beijersbergen, *Method for probing the orbital angular momentum of optical vortices in electromagnetic waves from astronomical objects.* Physical review letters, 2008. **101**(10): p. 100801.
54. Heckenberg, N., et al., *Generation of optical phase singularities by computer-generated holograms.* Optics letters, 1992. **17**(3): p. 221-223.
55. Bazhenov, V.Y., M. Soskin, and M. Vasnetsov, *Screw dislocations in light wavefronts.* Journal of Modern Optics, 1992. **39**(5): p. 985-990.
56. Khonina, S., et al., *Gauss–Laguerre modes with different indices in prescribed diffraction orders of a diffractive phase element.* Optics communications, 2000. **175**(4-6): p. 301-308.
57. Slussarenko, S., et al., *The polarizing Sagnac interferometer: a tool for light orbital angular momentum sorting and spin-orbit photon processing.* Optics Express, 2010. **18**(26): p. 27205-27216.
58. Mourka, A., et al., *Modal characterization using principal component analysis: application to Bessel, higher-order Gaussian beams and their superposition.* Scientific reports, 2013. **3**(1): p. 1422.
59. Dezfouli, A.M., et al., *Detection of the orbital angular momentum state of light using sinusoidally shaped phase grating.* Applied Physics Letters, 2022. **120**(19).
60. Gbur, G.J., *Singular optics*. 2016: CRC press.
61. Oemrawsingh, S., et al., *Experimental demonstration of fractional orbital angular momentum entanglement of two photons.* Physical review letters, 2005. **95**(24): p. 240501.
62. Basistiy, I., et al., *Synthesis and analysis of optical vortices with fractional topological charges.* Journal of Optics A: Pure and Applied Optics, 2004. **6**(5): p. S166.
63. Berry, M., *Optical vortices evolving from helicoidal integer and fractional phase steps.* Journal of Optics A: Pure and Applied Optics, 2004. **6**(2): p. 259.
64. Teng, M., et al., *Mechanical beam steering array antenna with tunable height.* IEEE Antennas and Wireless Propagation Letters, 2022. **21**(11): p. 2293-2297.

65. Benton, D.M. *Non-mechanical beam steering: ways and means*. in *Technologies for Optical Countermeasures XV*. 2018. SPIE.
66. Trichili, A., et al., *Optical communication beyond orbital angular momentum.* Scientific reports, 2016. **6**(1): p. 27674.
67. Čižmár, T. and K. Dholakia, *Exploiting multimode waveguides for pure fibre-based imaging.* Nature communications, 2012. **3**(1): p. 1027.
68. Mirhosseini, M., et al., *High-dimensional quantum cryptography with twisted light.* New Journal of Physics, 2015. **17**(3): p. 033033.
69. Ecker, S., et al., *Overcoming noise in entanglement distribution.* Physical Review X, 2019. **9**(4): p. 041042.
70. Fu, D., et al., *Realization of a scalable Laguerre–Gaussian mode sorter based on a robust radial mode sorter.* Optics express, 2018. **26**(25): p. 33057-33065.
71. Gu, X., et al., *Gouy phase radial mode sorter for light: concepts and experiments.* Physical review letters, 2018. **120**(10): p. 103601.
72. Zhou, Y., et al., *Sorting photons by radial quantum number.* Physical review letters, 2017. **119**(26): p. 263602.
73. Arlt, J., et al., *The production of multiringed Laguerre–Gaussian modes by computer-generated holograms.* Journal of modern optics, 1998. **45**(6): p. 1231-1237.

9 Author biography

Ali Mardan Dezfouli completed his bachelor's degree in Solid-State Physics from Zanjan University, followed by a master's degree in Optical Engineering at Malek-Ashtar University of Technology, Faculty of Science, Department of Physics. Following the completion of his MSc thesis, he began collaborating with the Institute for Advanced Studies in Basic Sciences (IASBS) in 2017. Afterward, he assumed the role of a research assistant in Hrvoje Skenderović's group at the institute of physics in Zagreb. He has co-authored five published scientific articles (with one more submitted) in reputable journals, and has contributed to one highlighted article. Additionally, he presented his dissertation topic at a conference in Barcelona, Spain as part of oral presentation.

List of publication:

1. **Dezfouli, A. M.**, Abramović, D., Rakić, M., & Skenderović, H. (2022). Detection of the orbital angular momentum state of light using sinusoidally shaped phase grating. *Applied Physics Letters*, *120*(19).
2. **Dezfouli, A. M**., & Skenderović, H. (2024). Higher-order topological charge detection using off-axis parabolic mirror. Applied Physics Letters, 124(10).
3. Amiri, P., **Dezfouli, A. M**., & Rasouli, S. (2020). Efficient characterization of optical vortices via diffraction from parabolic-line linear gratings. *JOSA B*, *37*(9), 2668-2677.
4. Hebri, D., Rasouli, S., & **Dezfouli, A. M**. (2019). Theory of diffraction of vortex beams from structured apertures and generation of elegant elliptical vortex Hermite–Gaussian beams. *JOSA A*, *36*(5), 839-852.

Selected conference presentations:

Dezfouli, A. M., Abramović, D., Rakić, M., & Skenderović, H, Detection of the orbital angular momentum state of light using sinusoidally shaped phase grating, December of 2022, Laser Congress and Exhibition, Barcelona International Convention Center, **Barcelona, Spain (oral presentation)**

Dezfouli, A. M.,Demoli, N., Abramović, D., Rakić, M., & Skenderović, H, Dynamic surface deformation measurement using digital holography interferometry, 2023 Siegman International School on Lasers, **Dublin, Ireland (poster presentation)**